X-ray Microdiffracion Techniques to Study the Microstructure of Materials

Khosrow Hassani

Doctor of Philosophy

July 2006

Department of Physics, McGill University
Montréal, Quebec

A thesis submitted to McGill University in partial fulfilment of the requirements of the degree of Doctor of Philosophy

Your file Votre référence
ISBN: 978-0-494-27787-4
Our file Notre référence
ISBN: 978-0-494-27787-4

To *my parents and sisters* who were patient

Abstract

X-ray microdiffraction is a powerful technique to study the microstructure of materials. In this thesis we built two x-ray microdiffraction setups and demonstrated their capabilities by two case studies. In our *microfocusing* setup, synchrotron x-rays were focused to a micron-size spot using a Fresnel zone plate. To scan the sample, we built a 3-axis translation stage with 30 nm step size over 25 mm travel range. Our *x-ray diffraction imaging (topography)* setup consisted of a monochromator, a channel-cut analyzer to define the diffraction angle, and a CCD camera with 0.645 μm pixels size to record the images. In our first project, we studied the microstructure of 90° ferroelectric domains and domain walls in barium titanate ($BaTiO_3$). We discovered a ~ 1 μm surface-like layer below the surface where domain walls angle, strain, and domains orientation deviate from the bulk values. These can be explained in terms of total energy minimization and domain-domain interaction. In our second project, we used x-ray topography to measure lattice deformations in the free and bent states of a silicon micro-cantilever used in scanning probe microscopy. We found that the cantilever was twisted by 8 mdeg with respect to the base and there were small strains in the cantilever and joint area. In the bent state, we measured 0.3 m average radius of anticlastic curvature and a maximum of 2×10^{-5} strain at the edges of the cantilever. We discuss possible causes of the twist and the non-zero strains. Our setups and the tools we developed can be used to study the microstructure of other similar systems, as well.

Abrégé

La microdiffraction des rayons X est une technique efficace dans l'étude de la microstructure des matériaux. Dans cette thèse nous avons élaboré deux méthodes de microdiffraction de rayons X et avons démontré leurs capacités en étudiant deux cas particuliers. Pour notre technique de microfocalisation, des rayons X provenant d'un synchrotron ont été focalisés en un point dont la taille était de l'ordre du micron en utilisant une plaque de zone Fresnel. Pour balayage rayons X de l'échantillon, nous avons construit une plate-forme dotée d'une translation sur 3 axes avec des pas de 30 nm sur une distance de translation de 25 mm. Notre installation d'imagerie de diffraction de rayons X (topographie) etait consistituée d'un monochromateur, d'un analyseur à canaux séparé pour définir l'angle de diffraction, et d'une camera CCD avec pixels de 0.645 μm pour enregistrer les images. Dans notre premier projet, nous avons étudié la microstructure du domaine ferroélectrique de 90° et des parois du domaine dans le titanate de baryum (BaTiO3). Nous avons découvert l'existance d'une couche d'environ 1 μm sous la surface où l'angle de la paroi du domaine, la tension, ainsi que l'orientation du domaine dévient des valeurs générales mesurées dans le volume du massif. Celles-ci peuvent être expliquées en termes de minimisation de l'énergie totale et des interactions entre domaines. Dans notre deuxième projet, nous avons utilisé un topographe à rayons X pour mesurer les déformations de structures cristallines associées aux états libres et courbés d'un microlevier de silicon utilisé en microscopie à force atomique. Nous avons découvert que le microlevier était torsadé de 8 mdeg par rapport à la base et qu'il y avait de petites tensions dans la région du microlevier et du joint. Dans l'état courbé, nous avons mesuré en moyenne un

rayon de courbure anticlastique de 0.3 m et une tension maximale de 2×10^{-5} sur les bords du microlevier. Nous discutons des raisons possibles de cette torsion et de cette tension. Nos installations et les outils que nous avons développés peuvent aussi bien être appliqués à l'étuder de la microstructure d'autres systèmes similaires.

Acknowledgements

"Who is not thankful to the creatures, is not thankful to the creator"

(Prophet Mohammad)

In the course of this work, there were pleasant and hard times; happy moments to devastating crises. In such situations, there were people who accompanied me and provided help, sympathy, and support. Not mentioning their names and acknowledging them would be totally dishonest and unfair.

First, I would like to thank my supervisor, Professor Mark Sutton, for his scientific guidance and financial support. He introduced me to the art of experimental physics by his unique insight of the science and research, and generously shared his extensive knowledge with me. He taught me more than one word. My best compliment on his standards is that it is literally impossible to satisfy him! Other colleagues from our group also deserve much gratitude: Martin Holt did parts of the experiments with Mark when I was denied access to the APS. Khalid Lazziri and Andrei Fluerasu, for rescuing me at the times of Yorick headaches and many constructive discussions about physics and other matters of life in the lab, office, or outside. My special thanks go to my friend and colleague, Saeid Asgharizadeh, for all the moments we shared together talking about politics, science, life, and our concerns and frustrations at lunch or break times. I should also mention newer members of our group, Yongfang Zhang and Zhenxing Feng, and wish them success. I am also indebted to these other colleagues: Professor Zaven Altounian was always a source of help and support in academic related issues. Robert Gagnon, Steve Kecani, Eddie Delcampo, Saverio Biunno, Michel Beauchamp, Frank Van Glis, and Leo Nikkinen, the technical staff of the department. I benefited form their expertise in doing my experiments and

technical issues. Computer and network experts, Juan Gallego and Paul Mercure provided excellent IT support and helped me with configuring and running Linux on my own computer. Without their help this work would be much harder. The kind and skillful secretary of graduate studies, Paula Dominguez, and other administration staff in the main office for providing around-the-clock information, help, and support. Mohsen Sabouri Ghomi, my first friend and buddy in the department who gave me very useful hints and suggestions at the beginning of my work. Chantal Boudreau, Nela Durisic, and Marianne Roussy, for being so nice to me and trying to reduce the pressure when we watched a movie, had a simple friendly chat, or shared a cup of coffee. I should also thank Chantal once more for the excellent French translation and Robert for final revision. Cristiano Dias, my great officemate, who was always nice and supportive. Mike, the friendly cleaner of the department, for his good job and many interesting discussions about the world.

Before going any further, I should mention my family: my parents, sisters, and cute niece, Mahshid, the people who payed the highest price. From my departure up to the present time, they patiently tried to encourage me to pursue my work and not be worry about anything else. They pretended that everything was OK, while I knew it was not. I thank them all and hope they forgive me.

Then, there were other friends mostly from the Iranian community in Montreal with whom I shared my sunny and rainy days, as well as, my bright and dark nights during my long stay at McGill. They, in one way or another, shaped my feelings as we ate, talked, worked, or walked together and shared our moments and secrets. The order people appear on my list is mostly chronological and by no means should reflect their influence or ranking in my mind. For all they did, I would like to express

my deep appreciations to the following people: Mr. Javeshkhani and Ali Rajaei who sheltered me in the first days when I was all alone. Mohammad who has been with me from the beginning up to now. Hengameh, an understanding friend, always caring even from far away. Ali, my dear friend, for all the cheer and all the moments we had together at home, in the swimming pool, football court, in travel, or in the cafes and also for his amicable and admirable character. Pari and Yahya for conveying hope and good feelings whether in a bike trip to Jean Talon or a pick up from the hospital. Bardia and Ali Shanian and their wives Leila and Mahta, the calm and peaceful friends. Again Saeid and his family, examples of rare people, both in the department and outside. My heavenly friend, Roya, for being there in the hot and humid nights of Sherbrooke and McGill College when I desperately needed a bench to rest and a breeze to cool down a bit, and there was none. Mahmood, my understanding and kind friend. This couple generously provided care and hospitality when they themselves needed them. And last, but not the least, my artist friend, Negin, who esthetically architectured a mystic space for the imagination of tea, journey of soul trough the joy and pain of light and darkness, aromatic inspiration of flowers, and the tearful pray of candles at Saint Joseph oratory. Each one of these people contributed a single word or a whole chapter, not to this thesis, but, to another book, the book of my life! I will certainly remember them whenever happens that I am looking back at those pages. For all they wrote and for their love, may God bring his blessing to them.

Contents

List of Tables

List of Figures

Chapter 1

Introduction

Materials are made of atoms which are bound together by inter-atomic forces. The goal of material science is to study the properties of materials using different theoretical and experimental methods. Among them, x-ray diffraction is one of the oldest and most powerful methods to get quantitative information about the atomic structure of materials. The overall subject of this thesis is to demonstrate how an extension of the conventional x-ray measurements can be used to obtain more detailed information about the structure of materials by a set of experiments and interpretation of the results.

Although fundamental properties of materials are defined by their inherent atomistic structure, often, many of their physical behaviors are determined by their structure on micron size scale. For example, ferromagnetic and ferroelectric materials demonstrate macroscopic magnetic or electric polarizations only when their micron-size domains are aligned in a preferable direction. Therefore, the study of microstructure of these systems can provide valuable information to understand their behavior. The system being studied can be heterogeneous with micron-size fine structures, or homogeneous with micrometer dimensions. In this thesis we have used x-ray mi-

croscopy to study one example of each case: the ferroelectric domains in barium titanate ($BaTiO_3$), a well known ferroelectric crystal, and the imperfections in a single crystal silicon cantilever used in scanning probe microscopy.

We use the term *microprobing* to refer to any technique used to study the structure of materials on micrometer scale. Several microprobing techniques exist each with its own advantages and limitations. In this chapter we will very briefly introduce the methods most popular and most relevant to the systems studied in our work.

Optical microscopy [72] is, perhaps, the oldest and most known technique. The instrument can be relatively simple and affordable. As the name implies, this technique can be used to study only transparent materials or, otherwise, image the outer surface of the sample. The spatial resolution of optical microscopy is in the range of light wavelength (a fraction of micrometer). Merz [91, 92] used a polarized optical microscope to study the domains structure in $BaTiO_3$. Merz [93], Little [87], and Miller et al. [95, 96] used the same method to study the motion of domain walls in $BaTiO_3$. Other versions of optical microscopes have been developed for special applications. *Confocal optical microscopy* is used to get three dimensional information mostly from biological systems [58].

Scanning Electron Microscopy (SEM) [111] and *Transmission Electron Microscopy* (TEM) [110] are techniques based on diffraction of electron beams from the sample. The typical energy of the electron beam in SEM is in the order of 10-100 keV and for TEM 100-1000 keV. These numbers translate to a few nanometer and sub-nanometer spatial resolutions for SEM and TEM, respectively. The instrument is more complicated and expensive, but, still can be installed and used in an ordinary laboratory. Because of the strong interaction of electrons with matter, the range of penetration

of electrons is very limited. SEM is used to image the surface of samples. TEM needs very thin samples ($\leq$100 nm) which usually require a lot of time and effort to prepare. Yakunin et al. [138] used high resolution TEM to investigate the fine structure of 90° domain walls in 500-2000 Å $BaTiO_3$ thin films. Floquet et al. [46] used SEM combined with x-ray diffraction to investigate the microstructure of thin films of $PbZr_{0.2}Ti_{0.8}O_3$ (PZT) on different substrates prepared with different methods. TEM is also a desirable way to measure strains in micron-size structures [33].

The other very important and relatively new category of microscopy techniques is based on the interaction of an atomically sharp tip located at the end of a micron-size cantilever with the surface of the sample. These techniques are generally referred to as *Scanning Probe Microscopy* (SPM). Because of the short range of the interaction, only a few atoms near the end of the tip interact with the atoms on the sample surface providing atomic resolution. Three most important examples of these techniques are *Scanning Tunneling Microscopy* (STM) [22], *Atomic Force Microscopy* (AFM) [119], and *Near-field Scanning Optical Microscopy* (NSOM) [29]. STM was invented in 1982. In this technique the tip is placed very close (about 1 nm) from the surface of a conducting specimen and a voltage of a few millivolts to 1 volt is applied between the tip and the sample. This causes a tunneling current between the uppermost atoms on the surface and the tip. Monitoring the movements of the cantilever (constant current mode) or the changes in the tunneling current (constant height mode) as a function of the tip position provides an image of the electronic structure of the sample surface. This current is very sensitive to the tip-surface distance. In STM the tip also exerts a force to the sample surface which was the idea behind invention of the first AFM in 1986. In AFM the force between the tip and the sample surface causes

small deflections of the cantilever which is recorded by a piezoelectric current or an optical beam reflected from the back of the cantilever. The sample does not need to be conductive. Measuring the cantilever deflection as a function of the tip position across the sample surface provides an image of the surface with atomic resolution. With AFM not only can one image the surface, but by bringing the tip in contact with the surface and applying a sufficiently big voltage, it is possible to displace atoms on the surface. Gruverman et al. [53] showed how scanning force microscopy can be used to both image and manipulate the ferroelectric domains in PZT thin films. Tarrach et al. [130] combined polarized light microscopy and piezoresponse force microscopy to find the three dimensional distribution of ferroelectric domains in $BaTiO_3$ and to locate the regions of interest on the sample. NSOM is a method where laser light is passed trough a small aperture near the sample surface. The size of the aperture is much smaller than the light wavelength. To achieve spatial resolution better than diffraction limits, the tip-surface distance must also be much smaller than the light wavelength, a region known as "near-field". The aperture is usually a sharp optical fiber coated by a metal everywhere except at its tip. Usually a feedback method is needed to keep the tip distance constant. NSOM can be used in transmission mode for transparent samples or reflection mode for opaque specimens. For example, Yang et al. [139] used NSOM to measure the motion of a single domain wall in ferroelectric lithium tantalate ($LiTaO_3$) with nanometer resolution. STM and AFM although have atomic spatial resolution, are methods to study the surface and provide little information about the bulk structure of the sample. In all these techniques, the imaging is rather slow because it requires a point-by-point scan of the sample. These microscopy methods are widely used in many research and industrial labs.

Among many experimental tools to study the properties of materials on micron size scale, x-ray diffraction [134, 1] has a special place. X-ray diffraction is more than a century old and has evolved extensively [94]. X-ray wavelengths are in the order of the size of atoms and their inter-atomic distances (a few Å) making them suitable for diffraction from atomic layers. Depending on the material and the wavelength, x-rays can normally penetrate several micrometers into sample. They can, therefore, be used as a non-destructive probe to acquire detailed data on the atomic scale from the bulk of the system under study. Four main parameters of a Bragg peak obtained in a typical x-ray diffraction experiment directly measure four essential properties of the sample:

- Peak integrated intensity is proportional to the amount of material contributing to the diffraction. Intensity also depends on the type and arrangement of atoms in the lattice through *structure factor* and can be, in principle, used to get information about this fundamental characteristic of the system (see chap. 2). Absorption and scattering by atoms also affect the intensity and provide extra information on the distribution and composition of matter in the sample. Therefore, changes in the peak intensity can be used to specify type, configuration, distribution, and number of atoms in the sample.

- Sample angle, θ, determines the orientation of the diffracting atomic planes and, therefore, reveals how atomic layers in the lattice are oriented with respect to each other and the sample surfaces. variations of this quantity show lattice rotation and disorientation.

- The diffraction angle, 2θ, directly measures the spacing between the atomic layers. A knowledge of 2θ helps to measure quantities such as lattice deforma-

tion and strain. With high resolution x-ray diffractometers strains as small as 1×10^{-5} or even less can be measured depending on the angular resolution of the measurements.

- Another Bragg peak parameter is the width which is inversely proportional to the size of the coherent diffraction volume or the crystal size, whichever smaller, in the direction of the diffraction vector. This provides information on the completeness and uniformity of the lattice.

In a more abstract way, x-ray diffraction data can directly measure the electron density function or, more exactly, the correlation between the electron density at two different points [20]. X-ray diffraction can be used to study almost any crystalline or non-crystalline material. The obtained data is not restricted to the surface of the sample and, depending on how deep x-rays can penetrate into sample, x-ray diffraction is considered a bulk probe. X-ray diffraction is fast, specially with the existing high flux synchrotron sources and fast detectors. These detectors (depending on their speed) can be used to do *in situ* study of the dynamics of processes which have an effect on the charge distribution in the system. Even though x-ray diffraction can, in principle, have atom-size resolution, this is reduced in the conventional x-ray diffraction techniques by the fact that the gathered data is an average over the entire diffraction volume.

The idea of *x-ray microdiffraction* (microscopy) [129] is to go beyond this limit and collect x-ray diffraction data from a micron-size region of the sample by utilizing one of the two *Microfocusing*, or *X-ray Diffraction Imaging* (XDI or *x-ray topography*) methods described in chap. 2. With x-ray microdiffraction we can get all the valuable information normal x-ray diffraction offers, with micrometer spatial resolution. One

can study the details of the static and dynamical properties of systems on micron-size scales. Not only the systems themselves, but many devices used to study these systems on micrometer or nanometer scales have micrometer dimensions. With the growing number of microfabrication facilities, micromachining is the technology extensively used to manufacture micro-devices. The manufacturing process itself can, in principle, introduce new deficiencies to the products in addition to those that inherently existed in the original material [104, 60, 65, 135]. These can influence the performance of the device in one way or another [65]. X-ray microdiffraction seems to be the most natural way of identifying imperfections in such devices [24, 25, 135]. In the microfocusing method, the diffraction volume is reduced by focusing the x-rays to a micron-size area using a focusing element such as a Fresnel Zone Plate (FZP) [68, 109]. In the XDI method, on the other hand, parallel x-rays get diffracted from a big volume, and then a micron-resolution detecting device such as a high-resolution photographic film or an x-ray CCD is used to spatially resolve the rays diffracted from different points on the sample [13]. Although, x-ray topography has been already used for several years using x-ray tube sources and special photography films, the realization of x-ray microdiffraction depends strongly on the existence of x-ray synchrotron sources as primary sources of extremely parallel and high flux coherent x-rays, and also on advanced x-ray optical devices [98]. X-ray microfocusing is only feasible with coherent x-rays from synchrotrons and special optical devices, such as x-ray Fresnel zone plates to focus the x-rays. Because of these technical complications, x-ray microdiffraction facilities and specially microbeam scanning microscopy, are not utilized as easily and widely as the other methods mentioned above. In chap. 2 we will briefly describe the principles of x-ray diffraction and then introduce x-ray microdiffraction methods with

special emphasis on the techniques used in our studies.

In this thesis we have designed, built and characterized experimental setups to conduct x-ray microdiffraction measurements with high spatial and angular resolutions. Some parts of the instrumentation and design have been done in the Physics Department at McGill University. The setups have been implemented at the Advanced Photon Source, Argonne National Laboratory where most of the experiments have been done. Modeling, software development, data analysis, interpretation of results, and comparison with theory have been mostly done at McGill. To characterize, calibrate, and demonstrate the capabilities of our setups, we performed two microdiffraction experiments. The samples used in our experiments, apart from the practical applications, were chosen mainly because they were excellent systems to be studied by our new setups. Our goal was to understand and characterize our setups and develop the required tools to overcome the new issues one has to deal with when doing x-ray microdiffraction experiments. The first system we studied had micron-size structures and the second system had micrometer dimensions.

As the first example, we studied the microstructure of 90° ferroelectric domains in barium titanate ($BaTiO_3$) crystals [59]. Ferroelectrics are materials that posses a spontaneous electric dipole moment which can be reversed by applying a sufficiently large electric field. Ferroelectrics have been the subject of extensive research [52], mainly because of their applications in making optical devices, actuators, microsensors, and more recently as candidates for *Non-Volatile Random Access Memories* (NVRAMs) [124, 32, 64, 137, 99]. These are memories that, once the information is stored, do not need a voltage to preserve it. To minimize the total free energy, materials in the ferroelectric phase form regions with different polarization directions, called

ferroelectric domains. The boundary between two neighboring domains is called a *domain wall*. Many static and dynamic properties of ferroelectric materials fundamental to their applications, such as polarization switching, fatigue, and coercive electric field are governed by the microstructure of ferroelectric domains and domain boundaries [123]. Therefore, to understand and characterize the properties of ferroelectric crystals, a detailed study of the structure of these materials on micron-size scale is essential. We have chosen barium titanate for our studies. It is a well studied and classic ferroelectric crystal from Perovskite family (with ABO_3 generic formula). At room temperature $BaTiO_3$ is in ferroelectric phase and has tetragonal lattice with a rather simple atomic and domain structure consisting of anti-parallel (180°) and perpendicular (90°) domains. The crystallographic $\langle 001 \rangle$ directions in the neighboring 90° domains are perpendicular to each other separated by domain walls at 45° with respect to the polarizations of the domains. Because of the small tetragonality ratio, $\frac{c}{a} \simeq 1.01$, the two adjacent 90° domains are distinguishable in an x-ray diffraction experiment. The micrometer size of these domains make them an ideal system for a microdiffraction study. Strain field exists around both 180° and 90° domain walls because of non-ideal matching of the lattices on two sides of the walls [92]. Strain is, however, more profound around 90° walls due to tetragonal lattice. Strain field, the associated elastic energy, and the interaction between the domains are important factors to be considered when studying ferroelectrics [30, 102, 17]. They affect many microscopic properties of the ferroelectric domains such as size and equilibrium configuration, domain stability and also domain boundaries orientation, profile, and thickness in the bulk and near the crystal surfaces [4, 2]. These, in turn, determine the electrical, electromechanical, and optical properties of these materials [19]. More

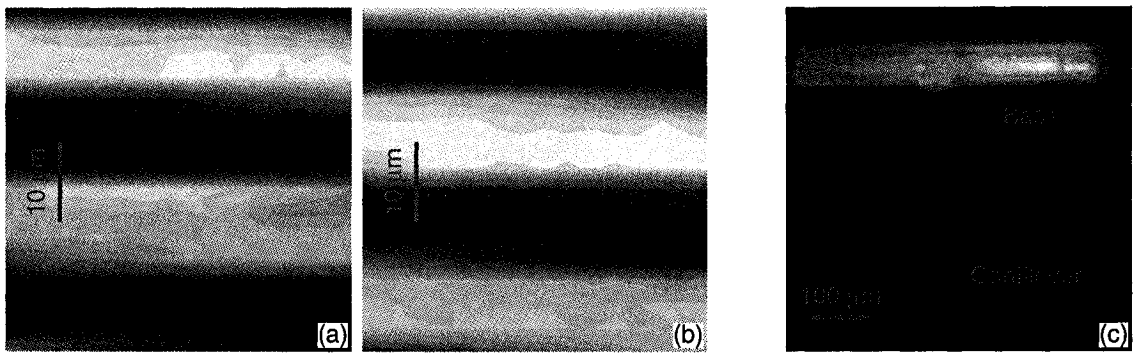

Figure 1.1: (a),(b) X-ray intensity plots of (200) and (002) domains in $BaTiO_3$: Bright and dark bands represent alternating domains in the same scan region. (c) XDI image of a silicon cantilever: Base appears brighter than the cantilever because it is much thicker.

importantly and from the novel applications point of view, many dynamical properties of these crystals directly depend on the domain wall energy through phenomena such as polling, domain wall motion, switching, and nucleation and growth of domains [97, 3, 127]. We did a detailed study of the structure of 90° domains and domain walls in a $BaTiO_3$ single crystal with $\sim$10 μm wide stripe-shape domain structure. From the results of our studies we could get an exact two dimensional map of the alternating stripe-shape 90° domains (Fig. 1.1(a) and (b)). We discovered new features in the structure of domains and domain walls in $BaTiO_3$ including the existence of a $\sim$ 1 μm thick layer near the crystal surface where the domain properties substantially differ from the bulk. In chap. 3 we will first review the physics of ferroelectrics and then present the details of our x-ray microdiffraction study of the 90° domains in $BaTiO_3$

.

In our second project, we used triple crystal (monochromator, sample, analyzer) parallel beam XDI technique to obtain micrometer-resolution lattice orientation and out-of-plane strain maps of a single crystal silicon cantilever[57]. We studied both

the "free" and slightly bent states of the cantilever. The main motivation behind this study was that our samples were nearly perfect micrometer-size single crystals. We wanted to know what type of information and to what level of precision our microdiffraction setups were able to obtain from such samples. From application point of view, they were manufactured by micromachining technique which is, essentially, a technology to fabricate micron size devices from bigger bulk materials. The fabrication process usually introduces residual strain and dislocations into the final product [60]. Identifying and characterizing imperfections in the micromachined products is crucial for the manufacturers to improve their products [108]. It is also important for the users of these devices to know about the possible imperfections in the devices they use, because, they affect the performance of the device [65]. For example, residual strain in cantilevers used in scanning microscopy experiments can affect the resonance frequency of the cantilever [88, 23]. In addition to the inherent imperfections, bending strain develops in these devices when they undergo mechanical or thermal deformations. Some of these devices are essentially used as micro-sensors to measure the surface strain [113, 114]. A great amount of work has been focused on silicon, because of its various applications in industry and research [135, 60, 65].

Different techniques are available to measure imperfections with micrometer resolution [33]. The most important ones can be found in the references given in chap. 4. High resolution XDI is a powerful and, perhaps, the most common technique used by many researchers to study imperfections in nearly perfect crystals. The principles of this technique has been clearly elaborated by, for example, Newkirk [103], Tanner [13], and Authier [6] in their books. A brief summary of the technique used in this thesis will be given in chap. 2. One of the difficulties in this technique is, however, to

properly identify, resolve, and distinguish between lattice rotation and lattice strain in small crystals comparable in size with the spatial resolution of the obtained images (usually a few micrometers). Another aspect is the sensitivity of the method. There have been work to measure strain and lattice curvature in big crystals under large bending stress. Bell [9] studied large deflections, and rotations in cantilever beams. Yang et al. [140] measured strain and anticlastic curvature in a centimeter-size silicon crystal under large deflection bending. The need to measure distortions in slightly deformed micron-size crystals with high resolution and without ambiguity still exists.

We used high (angular and spatial) resolution plane-wave XDI method to accurately measure two dimensional maps of lattice orientation, twist, and out-of-plane strain in a micrometer-size single crystal silicon cantilevers used in scanning force microscopy. Our experimental setup and methods we used to model and analyze the data were designed to remove the inherent ambiguities in these types of experiments as much as possible. One example of the integrated intensity map of the cantilever and the base is presented in Fig. 1.1(c). the whole cantilever and supporting base was a one-piece single crystal micromachined from a bulk silicon crystal. We studied the unstrained state of the cantilever, as well as, the slightly bent state. We discovered that the cantilever, as a whole piece, was twisted with respect to the base right at the junction area by $\sim$8 mdeg. Accurate measurement of the twist angle is essential in measuring the lateral forces in AFM [69]. Sader [115] stated that this is hard to measure in micron-size cantilevers. Two dimensional maps of the sample angle of the bent cantilever showed anticlastic curvature across the cantilever width in agreement with the elasticity theory for a bent beam [83, 50]. The average radius of curvature at the middle of the cantilever length was about $\sim$0.3 m. We observed non-zero strain

both in the "free" and bent states of the cantilever. Our results showed compressive strain in the order of 2×10^{-5} at the cantilever edges. In chap. 4 a short review of the imperfections introduced by micromachining, and the major work done to measure them in small crystals will be given. We will then describe the details of our experiments, analysis methods, and results.

In chap. 5 a summary of our results and achievements will be presented along with suggestions for future work.

Chapter 2

X-ray microdiffraction

The main objective in this chapter is to introduce the x-ray microdiffraction techniques used in this thesis. However, to achieve this goal, it is first necessary to review some basic concepts of x-ray diffraction. This will also provide the required base to understand the experimental results and discussions in the following chapters.

Electromagnetic radiations with photon energy in the range of a few keV (wavelength = 0.1-10 Å) are usually referred to as x-rays. Since the energy of x-ray photons are orders of magnitude bigger than the binding energy of electrons in atoms (a few eV), these electrons are considered more or less "free". In a classical picture, in response to the electric field of the x-rays, these electrons oscillate and emit secondary electromagnetic waves with the same energy which are called *scattered waves*. The elastic scattering of x-rays from electrons (*Thompson scattering*,) is the base of the interaction of x-rays with matter. X-rays can also get absorbed by atoms through phenomena such as photoelectric effect which are not considered here. For a single electron, the ratio between the amplitudes of the scattered and incident waves is proportional to $\frac{r_0}{R}$, where r_0=2.82×10^{-5} Å is a constant called the *Thompson scattering length* or *classical electron radius* (see eq. 2.1), and R is the distance of the observa-

tion point from the scattering center. In principle, the incident x-rays get less intense after each scattering. Moreover, the scattered waves can get scattered again by other electrons and the effect of these multiple scatterings should be considered. However, in most of the x-ray diffraction experiments, these complications can be ignored. This approximation, called *kinematical x-ray diffraction*, is valid for samples with enough imperfections in their lattice. In the case of nearly-perfect crystals, where these effects become important, the more general theory of *dynamical x-ray diffraction* must be considered.

2.1 Kinematical theory of x-ray diffraction

In this section we assume that the interaction of x-rays with matter is weak (*Born approximation*) and the crystal is not a single perfect lattice, but rather consists of several small blocks with slightly different (0.01° -0.1°) orientations. This is often called a *mosaic* structure. With these assumptions we can neglect the effect of scattering on the intensity of the incident beam and don't need to consider multiple scattering phenomena.

2.1.1 X-ray scattering by a single electron

Suppose a monochromatic plane x-ray wave travelling in z direction reaches a single free electron with charge $-e$ located at the origin. We can define the xz plane to include the observation point $\mathbf{R}$(Fig. 2.1). Then, the amplitude of the incident electric field, $\mathbf{E_0^i}$ will have two E_{0x}^i and E_{0y}^i components. From electromagnetism theory [67], the amplitude of the radiated electric field at point $\mathbf{R}$, $\mathbf{E_0^r}$, has two components: one

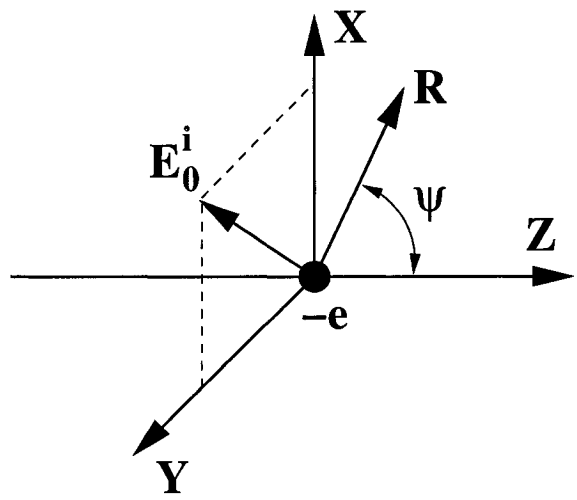

Figure 2.1: X-ray scattering by a single electron

in the xz plane and perpendicular to **R** (produced by E^i_{0x}), and another one parallel to y axis (produced by E^i_{0y}):

$$E^r_{0xz} = -r_0 E^i_{0x} \frac{e^{ikR}}{R} \cos\psi \tag{2.1}$$

$$E^r_{0y} = -r_0 E^i_{0y} \frac{e^{ikR}}{R} \tag{2.2}$$

In these equations, ψ is the angle between the observation vector and the propagation direction of the incident wave, and r_0 is a constant length called the Thompson scattering length or classical electron radius :

$$r_0 \equiv \frac{e^2}{4\pi\epsilon_0 mc^2} = 2.82 \times 10^{-5}\,\text{Å}, \tag{2.3}$$

where m is the mass of the electron and c is the speed of light. In practice, what an x-ray detector at **R** measures is the number of x-ray photons scattered into a small solid angle $\Delta\Omega$ around **R**. The *differential cross-section* is defined as the number

of photons scattered per unit time into a unit solid angle around **R** divided by the number of incident photons per unit time per unit area (incident flux). Since the flux is proportional to the square of the electromagnetic field, we can write the scattering differential cross-section as:

$$\frac{d\sigma}{d\Omega} \equiv \frac{1}{\Delta\Omega}\frac{|\mathbf{E}^r|^2 R^2 \Delta\Omega}{|\mathbf{E}^i|^2} \tag{2.4}$$

$$= \frac{{E^r_{0xz}}^2 + {E^r_{0y}}^2}{{E^i_0}^2}. \tag{2.5}$$

Substituting from eq. 2.1 and remembering that for an unpolarized incident electric field, $\mathbf{E}^i$, each of x and y components carries half of the total intensity, we get:

$$\frac{d\sigma}{d\Omega} = r_0^2 P. \tag{2.6}$$

P is called the *polarization factor*:

$$P = \begin{cases} 1 & \text{if } \mathbf{E}^i_0 \text{ is polarized in y direction.} \\ \cos^2\psi & \text{if } \mathbf{E}^i_0 \text{ is polarized in x direction.} \\ \frac{1}{2}(1+cos^2\psi) & \text{unpolarized light.} \end{cases} \tag{2.7}$$

2.1.2 X-ray diffraction from a crystal

Consider the elastic scattering of monochromatic x-rays from a system of electrons each one with charge $-e$ located at position **r** with respect to the charge at the origin. Suppose $\mathbf{k_i}$ and $\mathbf{k_o}$ are the wave vectors of the incident and scattered waves (Fig. 2.2).

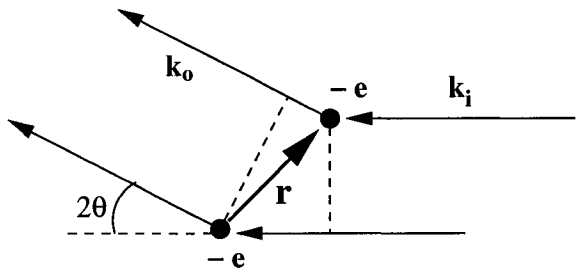

Figure 2.2: X-ray scattering a system of electrons

Because of the elastic scattering, the magnitude of the incident and scattered x-rays are equal, i.e $|\mathbf{k_i}| = |\mathbf{k_o}|$. The total amplitude of the scattered waves (in units of $-r_0$ and dropping the polarization factor) is proportional to the sum of the scattering terms from each electron:

$$A(\mathbf{q}) = \int_V \rho(\mathbf{r})\, e^{i\mathbf{q}\cdot\mathbf{r}}\, d\mathbf{r}, \tag{2.8}$$

where $\mathbf{q} = \mathbf{k_o} - \mathbf{k_i}$ is called the *scattering vector*, $\rho(\mathbf{r})$ is the *electron number density*, and V is the *scattering volume*. The exponential term accounts for the phase difference between waves scattered from the charge at $\mathbf{r}$ and the one at the origin. Scattering intensity is given by the square of the scattering amplitude:

$$I(\mathbf{q}) = |A(\mathbf{q})|^2. \tag{2.9}$$

Eqs. 2.8 and 2.9 state that the x-ray scattering intensity is directly proportional to the square of the Fourier transform of the charge density in the scattering volume. A crystalline material, by definition, consists of a set of atoms (the *basis*) repeatedly positioned on a three dimensional periodic network of sites (the *lattice*). The smallest unit of the lattice points is called the *primitive unit cell*. One can specify the coordinates of each electron in space by $\mathbf{r} = \mathbf{R_n} + \mathbf{r'}$ where $\mathbf{R_n} = n_1\mathbf{a_1} + n_2\mathbf{a_2} + n_3\mathbf{a_3}$ is the lattice

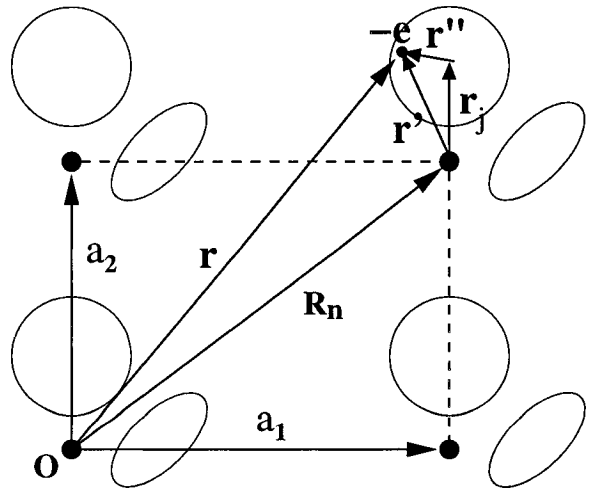

Figure 2.3: Scattering from a crystalline material. The base is assumed to have two different atoms represented by a circle and an ellipse.

coordinates and $\mathbf{r}'$ is the position of the electron in the unit cell (Fig. 2.3). Since in a crystalline structure, by definition, charge density is a periodic function of the lattice vectors, we have $\rho(\mathbf{r}) = \rho(\mathbf{R_n}+\mathbf{r}') = \rho(\mathbf{r}')$. The integral in eq. 2.8 can be converted to sum over lattice points and integration in the unit cell: $\int_V d\mathbf{r} \rightarrow \sum_{lattice} \int_{unit\ cell} d\mathbf{r}'$. Therefore, we get:

$$A(\mathbf{q}) = \sum_n^N e^{i\mathbf{q}\cdot\mathbf{R_n}} \int_{unit\ cell} \rho(\mathbf{r}')\, e^{i\mathbf{q}\cdot\mathbf{r}'}\, d\mathbf{r}', \tag{2.10}$$

where N is the total number of lattice sites. Electron density in the unit cell is the sum of the contributions from all the atoms in the basis: $\rho(\mathbf{r}') = \sum_j \rho_j(\mathbf{r}'')$. Also it is clear that: $\int_{unitcell} d\mathbf{r}' \rightarrow \sum_{base} \int_{unitcell} d\mathbf{r}''$. With this considerations, we get the new form of the scattering amplitude:

$$A(\mathbf{q}) = \sum_n^N e^{i\mathbf{q}\cdot\mathbf{R_n}} \sum_j e^{i\mathbf{q}\cdot\mathbf{r_j}} \int_{unit\ cell} \rho_j(\mathbf{r}'')\, e^{i\mathbf{q}\cdot\mathbf{r}''}\, d\mathbf{r}''. \tag{2.11}$$

Here $\mathbf{r_j}$ and $\mathbf{r''}$ represent the coordinates of atoms in the basis and atomic coordinates, respectively and $\rho_j(\mathbf{r''})$ is the electron number density of atom number j in the basis. The *atomic form factor* for atom j is defined as the integral in eq. 2.11:

$$f_j(\mathbf{q}) \equiv \int_{unit\ cell} \rho_j(\mathbf{r''})\, e^{i\mathbf{q}\cdot\mathbf{r''}}\, d\mathbf{r''}. \tag{2.12}$$

Therefore, eq. 2.11 can be rewritten as:

$$A(\mathbf{q}) = \underbrace{\sum_n e^{i\mathbf{q}\cdot\mathbf{R_n}}}_{Lattice\ sum} \underbrace{\sum_j e^{i\mathbf{q}\cdot\mathbf{r_j}} f_j(\mathbf{q})}_{\substack{Unit\ cell \\ structure\ factor}} \tag{2.13}$$

$$= F(\mathbf{q}) \sum_{n=1}^{N} e^{i\mathbf{q}\cdot\mathbf{R_n}}. \tag{2.14}$$

$F(\mathbf{q})$ is the *structure factor*. Then, the intensity of the scattered x-rays (eq. 2.9) will be equal to:

$$I(\mathbf{q}) = |F(\mathbf{q})|^2\ (N + \sum_{n=1}^{N} \sum_{\substack{m=1 \\ m\neq n}}^{N} e^{i\mathbf{q}\cdot\mathbf{r_{nm}}}), \tag{2.15}$$

where $\mathbf{r_{nm}} = \mathbf{r_n} - \mathbf{r_m}$ is another lattice vector.

2.1.3 Reciprocal lattice, Laue and Bragg conditions

For an ordinary sample, N, the total number of sites in the lattice, is a big number (in order of 10^{12} for a micron-size crystal). The second term in eq. 2.15 depends on the scattering wave vector, $\mathbf{q}$, and is huge compared to the first term only if $\mathbf{q}\cdot\mathbf{r_{nm}}$ is a multiple of 2π (it will be of order of N^2). This can be better explained by introducing a new space. The *reciprocal space* is defined by three base vectors $\mathbf{a^*}$ so

that: $\mathbf{a}_i \cdot \mathbf{a}_j^* = 2\pi\delta_{ij}$, where δ_{ij} is the Kronecker delta function ($\delta_{ij} = 1$ if $i = j$, and zero otherwise). In practice, the reciprocal lattice is defined in terms of the lattice vectors by the following set of equations:

$$\mathbf{a}_1^* = 2\pi\frac{\mathbf{a}_2 \times \mathbf{a}_3}{v_c} \quad , \quad \mathbf{a}_2^* = 2\pi\frac{\mathbf{a}_3 \times \mathbf{a}_1}{v_c} \quad , \quad \mathbf{a}_3^* = 2\pi\frac{\mathbf{a}_1 \times \mathbf{a}_2}{v_c}, \tag{2.16}$$

where $v_c = \mathbf{a}_1 \cdot \mathbf{a}_2 \times \mathbf{a}_3$ is the volume of the unit cell . The condition for strong scattering is only satisfied when the diffraction vector terminates on a point in the reciprocal lattice which is called *Laue condition*:

$$\mathbf{q} = \mathbf{G}, \tag{2.17}$$

where $\mathbf{G} = h\,\mathbf{a}_1^* + k\,\mathbf{a}_2^* + l\,\mathbf{a}_2^*$ (h, k, l integers) is a vector in the reciprocal lattice. In this case the scattered waves constructively interfere and the term *diffraction* is used instead of scattering.

Atomic planes in a crystalline material are usually characterized by three integer numbers, known as *Miller indices*, representing the smallest common multiple of the inverse of their intersection coordinates with the principle axes of the lattice. It is easy to show that the diffraction vector $\mathbf{q}$ is perpendicular to the atomic planes ($h\,k\,l$), and the inter-plane distance d is equal to $\frac{2\pi}{|\mathbf{G}|}$ (Fig. 2.4(a)). Since $|\mathbf{q}| = \frac{4\pi\sin(\theta)}{\lambda}$, where λ is the x-rays wave length and θ is half of the diffraction angle, Laue condition can be restated in terms of real space parameters. In this form it is called *Bragg's law* for diffraction:

$$2d\sin\theta = \lambda. \tag{2.18}$$

As seen in Fig. 2.4(a), the angle x-rays make with the diffracting planes (not the

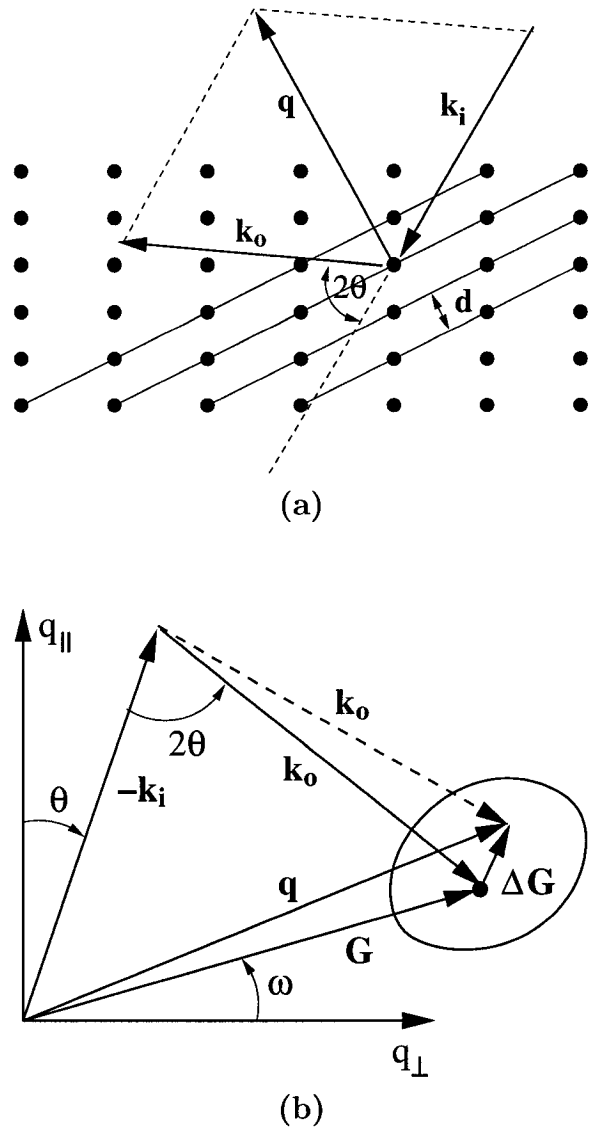

Figure 2.4: (a) Bragg condition for x-ray diffraction from a crystal. (b) Laue condition in reciprocal space. To measure the integrated intensity, one should consider all the diffracted rays from the finite size Bragg peak region in the reciprocal space. $q_\perp$ and $q_{||}$ are components of the diffraction vector perpendicular and parallel to the crystal surface.

crystal surface) is half of the diffraction angle 2θ. For a given wavelength and a particular set of atomic planes, there is only one diffraction angle which satisfies the Bragg condition. There is, however, a degeneracy; the crystal can rotate about the diffraction vector $\mathbf{q}$.

2.1.4 Measured diffraction intensity

Since the diffraction volume in a crystal has a finite size, the Laue condition does not have to be precise. This means that instead of eq. 2.17, in reality we have:

$$\mathbf{q} = \mathbf{G} + \mathbf{\Delta G}, \tag{2.19}$$

where $\mathbf{\Delta G}$ defines a small volume around $\mathbf{G}$ (fig. 2.4(b)). Since $\mathbf{k}_o = \mathbf{k}_i + \mathbf{q}$, for monochromatic and perfectly collimated incident rays, the diffracted rays are monochromatic (elastic scattering) but have a finite divergence. The Bragg peaks are not points, but rather small smeared spots in the reciprocal space. The detector usually accepts a range of diffraction angle 2θ. However, to collect all the diffracted intensities, the crystal must be scanned around the Bragg peak position (called a θ rock) to cover all the possible diffractions inside the Bragg peak volume. The number of photons per unit time per unit solid angle measured this way is called the *integrated intensity*. It can be shown [1, page 148] that the integrated intensity for a crystal is equal to:

$$I = \Phi_0 \, r_0^2 \, P \, |F(\mathbf{q})|^2 \, N \, \frac{\lambda^3}{v_c} \, \frac{1}{\sin 2\theta}, \tag{2.20}$$

where Φ_0 is the incident flux, N is the total number of unit cells, and the other variables have been defined before. The $\frac{1}{\sin 2\theta}$ is called the *Lorentz factor*. Integrated

intensity is proportional to N and, therefore, to the amount of material contributing to the diffraction. Note that sample position is conventionally denoted by θ and diffraction angle by 2θ. These are names given to these angles and θ is not necessarily equal to half of 2θ. To emphasize the distinction, often the difference is defined as sample orientation angle, ω (see fig 2.4(b)):

$$\omega = \frac{2\theta}{2} - \theta. \tag{2.21}$$

The intensity of x-rays diminishes after penetrating through materials. There are several mechanisms responsible for this. When Bragg condition is satisfied, strong diffraction of x-rays into the exit beam reduces the intensity of the incident wave. This phenomenon is called *extinction* and will be discussed in the next section. In kinematical approximation extinction is ignored. The other cause for reducing the intensity of the incident beam is mainly the photoelectric effect. An x-ray photon releases a K-level electron from an atom leaving the atom ionized. Fig. 2.5(a) shows the absorption mechanism: the intensity of the beam after passing through a thickness dz' of the material is reduced by dI which is proportional to dz' itself (more material, more absorbing centers) and the initial intensity of the beam $I(z')$ (bigger incoming flux, bigger chance of absorption):

$$\begin{aligned} dI &\equiv I(z'+dz') - I(z') = -\mu\, I(z')\, dz' \\ &\rightarrow I(z) = I(0)\, e^{-\mu z}. \end{aligned} \tag{2.22}$$

The proportionality constant is called the *absorption coefficient* μ and the *absorption length* is defined as $\frac{1}{\mu}$. This is the thickness, over which, the intensity of the beam

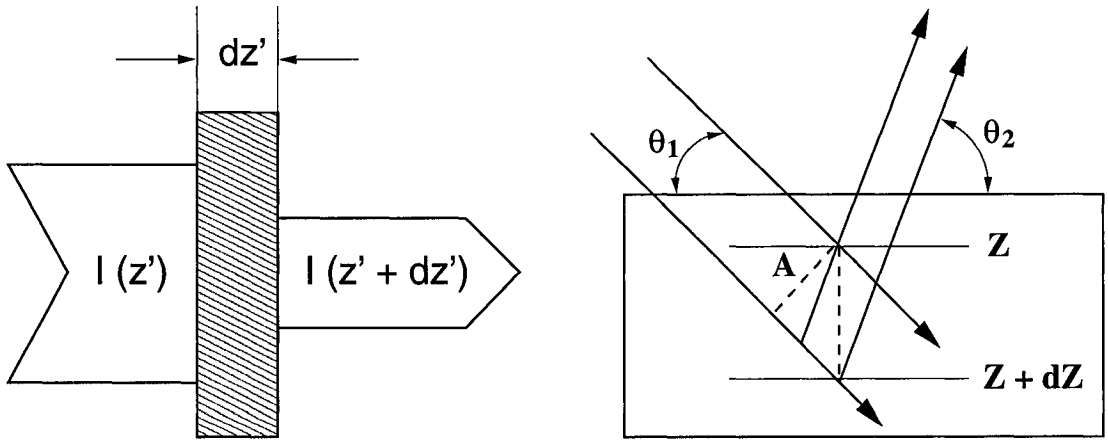

Figure 2.5: (a) Absorption of x-rays. (b) Absorption effect on integrated intensity.

reduces by a factor of $1/e$. In general, absorption length depends on the energy of the incident photons. For example, for silicon and 6.5 keV x-ray photons, this is about 58 μm.

Absorption must be taken into account when calculating the integrated intensity. Suppose a beam with cross-section A is incident on a slab of material. We assume the material is big enough to intercept the entire beam. Let θ_1 and θ_2 be the incident and exit angles of the beam with the material surface and z measure the depth from the surface (Fig. 2.5(b)). The scattering volume between z and $z + dz$ is a parallelogram with volume $dV = \frac{\cos\theta_2 A\, dz}{\sin(\theta_1+\theta_2)}$. To obtain a formula for the integrated intensity with absorption, we suppose a mosaic structure for the crystal. Then, we have to replace N in eq. 2.20 by $N'N_m$ where, N' is the (average) number of unit cells in a mosaic block and N_m is the number of mosaic blocks. Therefore, the number of mosaic blocks in the diffraction volume is equal to $N_m = \frac{dV}{V'}$, where V' is the volume of each mosaic crystalline. The total path the beam travels inside the material is $z(\frac{1}{\sin\theta_1} + \frac{1}{\sin\theta_2})$.

Integrating over z values, we get:

$$I = \Phi_0 r_0^2 P |F(\mathbf{q})|^2 \frac{N'}{V'} \frac{\lambda^3}{v_c} \frac{1}{\sin 2\theta} \frac{A \cos\theta_2}{\sin(\theta_1+\theta_2)} \int_0^\infty e^{-\mu z(\frac{1}{\sin\theta_1}+\frac{1}{\sin\theta_2})} dz$$

$$= \Phi_0 r_0^2 P |F(\mathbf{q})|^2 \frac{A}{\mu v_c^2} \frac{\lambda^3}{\sin 2\theta} \frac{\cos\theta_2}{\sin(\theta_1+\theta_2)} \frac{\sin\theta_1 \sin\theta_2}{\sin\theta_1+\sin\theta_2}. \quad (2.23)$$

2.2 Dynamical theory of x-ray diffraction

For a precise study of x-ray diffraction from nearly perfect crystal, the kinematical theory of x-ray diffraction described in the previous section is not enough and one should use the more general dynamical theory of x-ray diffraction. Since some of the samples we studied in this thesis were very high quality crystals, some important concepts of the dynamical theory of x-ray diffraction will be reviewed here. A more complete description of the theory can be found in the references listed in the bibliography [6, 1, 8].

2.2.1 Diffraction from Perfect crystals

When Bragg condition is satisfied, strong diffraction of x-rays into the exit beam diminishes the intensity of the incident beam. In a perfect crystal this effect is more profound because the periodic lattice extends far enough to scatter an appreciable fraction of the incident beam. This phenomenon is called extinction which, even in non-absorbing crystals, defines a finite depth, known as *extinction length*, over which almost all the incident photons diffract off the crystal. This is a finite size effect and introduces an intrinsic broadening to the Bragg peaks, known as the *Darwin width*.

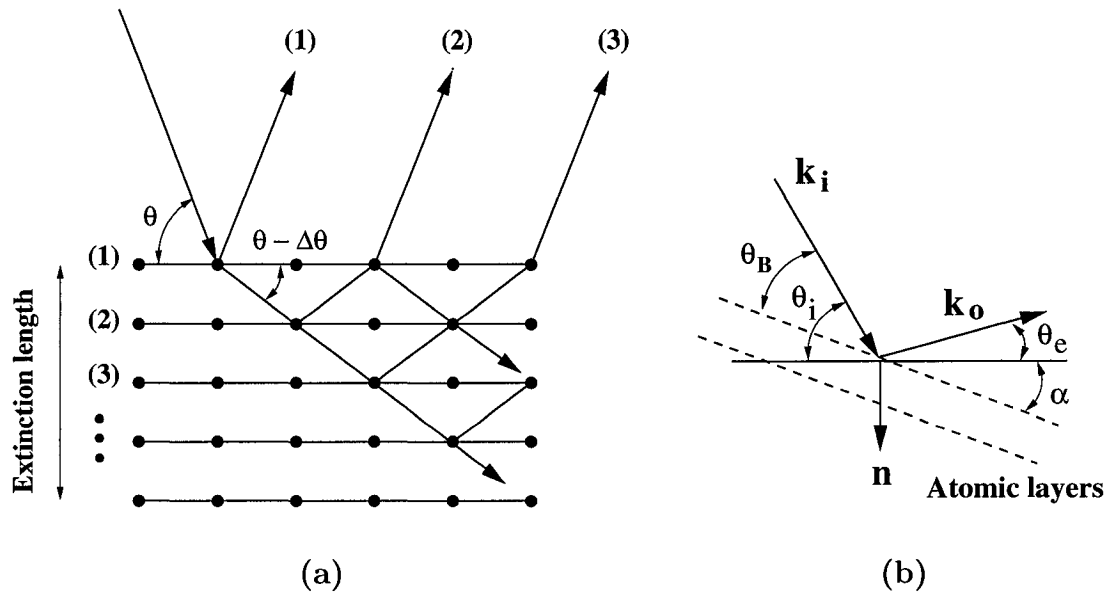

Figure 2.6: (a) Extinction and deviation from Bragg angle (b) Asymmetric diffraction

Like other finite size effects, Darwin width of a Bragg peak in the reciprocal space is proportional to the inverse of the extinction length, provided that the crystal is thick enough to diffract the whole incident wave.

Another important effect is the refraction of x-rays when they enter a crystal. For x-rays, the refraction index of materials, n, is smaller than but very close to 1. Refraction of x-rays at the air-crystal interface changes the direction of x-rays inside the crystal (Fig. 2.6(a)) by a small amount of the order of $\delta = 1 - n \sim 10^{-5}$ rad. This, in turn, causes a small deviation of the Bragg peak angle form what Bragg's law (eq. 2.18) predicts. The order of magnitude of this deviation can be calculated from *Snell's law*[12]:

$$\begin{aligned} \cos\theta &= n\cos(\theta - \Delta\theta) \simeq n\cos\theta + n\sin\theta\,\Delta\theta \\ \rightarrow \Delta\theta &\simeq \frac{1-n}{n}\frac{1}{\tan\theta} \simeq \frac{\delta}{\tan\theta} \sim 10^{-5}\,\text{rad.} \end{aligned} \tag{2.24}$$

Another important effect is that x-rays diffracted from an atomic layer will satisfy Bragg's law when passing trough other atomic layers and, hence, have the chance to get scattered again and return to the incident beam (see fig. 2.6(a)). Multiple scattering reduces the integrated intensity of the exit beam from what the kinematical approximation predicts (eq. 2.20). A quantitative consideration of all these effects is called the dynamical theory of x-ray diffraction. There are two main approaches to calculate the dynamical diffraction effects. Darwin considered a perfect crystal as a set of atomic layers and calculated the combination of multiple scattering from these layers. Ewald, on the other hand, solved Maxwell's equations in a continuum medium with periodic dielectric constant. Both approaches give similar results which are briefly presented here. It can be shown [6, 15] that the deviation of the center of the Bragg peak, $\Delta\theta$, and the Darwin width, w, for the incident beam are given by:

$$\Delta\theta_i^{cen} = \frac{2r_0d^2}{\pi v_c}|F(0)|\tan\theta_B\frac{1-\gamma}{2\gamma}, \tag{2.25}$$

$$w_i = \frac{2r_0d^2}{\pi v_c}|F(\mathbf{q})|\tan\theta_B P\frac{\gamma}{|\gamma|^{1/2}}, \tag{2.26}$$

where $\mathbf{q}$ is the diffraction vector, $|F(0)|$ and $|F(\mathbf{q})|$ are the structure factors at $\mathbf{q}=0$ and $\mathbf{q}=\mathbf{q}$ (broadening is more effective for strong reflections), θ_B is the kinematical Bragg angle (eq. 2.18), P is the polarization factor, and γ is called the *asymmetry factor* defined as:

$$\gamma \equiv \frac{\mathbf{n}\cdot\mathbf{k}_o}{\mathbf{n}\cdot\mathbf{k}_i}. \tag{2.27}$$

In this equation $\mathbf{k}_i$ and $\mathbf{k}_o$ are the incident and exit wave vector directions and $\mathbf{n}$ is the surface normal pointing into the crystal. γ is positive for the Laue case and negative for the Bragg case. $\gamma = \pm 1$ show symmetric Laue and symmetric Bragg

cases, respectively. The corresponding quantities for the exit beam are given by [15]:

$$\Delta\theta_e^{cen} = -\frac{\Delta\theta_i^{cen}}{\gamma}, \tag{2.28}$$

$$w_e = -\frac{w_i}{\gamma}. \tag{2.29}$$

Using Bragg's law (eq. 2.18), we can translate the Darwin width in angle to a similar width in wavelength:

$$\frac{\delta\lambda}{\lambda} = \frac{\delta\theta}{\tan\theta}, \tag{2.30}$$

where $\delta\theta$ is the angle spread of the beam and can be replaced by w_i or w_e to get the wavelength spread of the incident or exit beams. Wavelength spread defines a range of wavelengths that can be collected by the crystal from the incident beam or diffracted to the exit beam.

2.2.2 Darwin reflectivity curve

In considering dynamical diffraction experiments, two different geometries are specially important. In *symmetric Bragg* case, the diffracting planes are parallel to the crystal surface(Fig. 2.7(a)), whereas in *symmetric Laue* case, they are perpendicular to the crystal surface (Fig. 2.7(b)). A curve showing the ratio of the intensity of the exit beam to that of the incident beam vs beam angle or wavelength is called a *Darwin reflectivity curve.* Fig. 2.8 shows Darwin reflectivity curve for Si(111) reflection in symmetric Bragg geometry from a 50 μm thick crystal. The red thin graph shows the case where the real absorption is assumed to be zero. The solid curve shows the reflectivity with absorption. The center of the peak is shifted from the kinematical Bragg value at zero. For low absorption the reflectivity is near unity within the Dar-

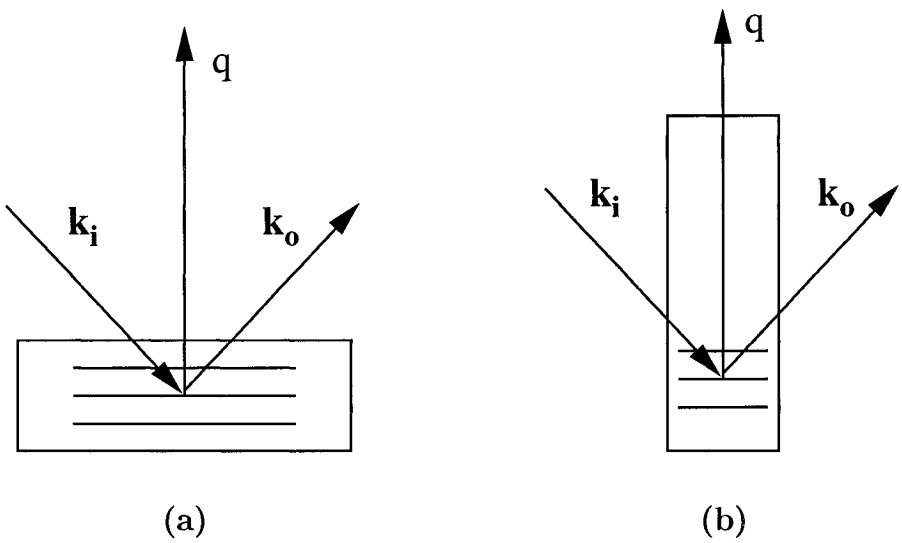

Figure 2.7: (a) Symmetric Bragg case (b) Symmetric Laue case

win width. Rapid oscillations show the finite size effect due to the finite thickness of the crystal. The period of these oscillations in the reciprocal space is equal to $\frac{2\pi}{t}$, where t is the crystal thickness. Using the notations introduced in Fig. 2.6 and eqs. 2.25 and 2.28, we can express the incident and exit angles as follows:

$$\theta_i = \alpha + \theta_B + \Delta\theta_i^{cen} + \Delta\theta_i, \tag{2.31}$$

$$\theta_e = -\alpha + \theta_B + \Delta\theta_e^{cen} + \Delta\theta_e. \tag{2.32}$$

In these equations $\Delta\theta^{cen}$ measures the deviation of the center of the incident and diffracted peak values from kinematical Bragg angle, and $\Delta\theta$ shows the position of an arbitrary point relative to the center of the peak (see Fig. 2.8). A relation similar to eq. 2.28 exists between $\Delta\theta$ values for the exit and incident beams:

$$\Delta\theta_e = -\frac{\Delta\theta_i}{\gamma}. \tag{2.33}$$

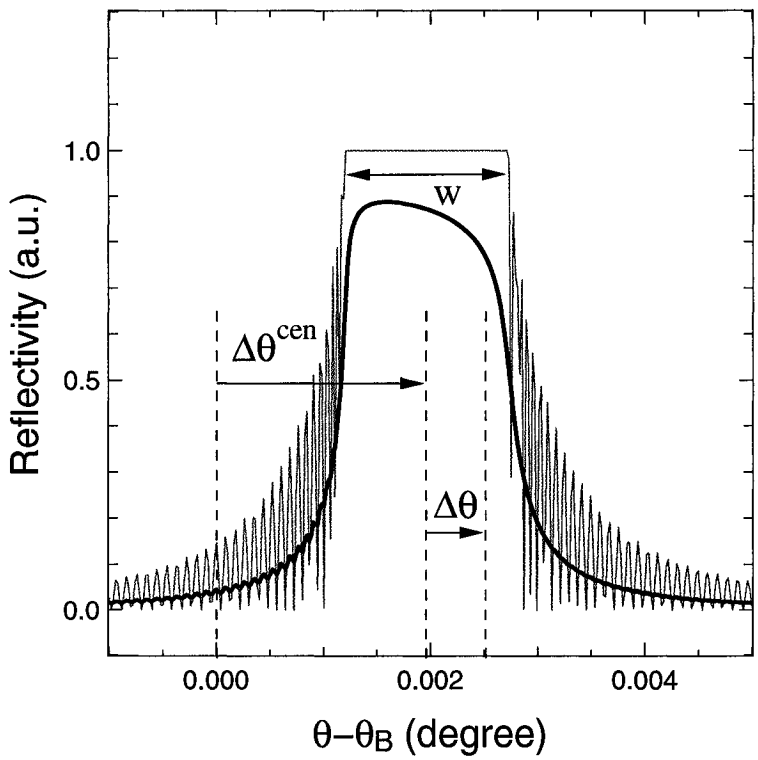

Figure 2.8: Darwin reflectivity curve for Si(111) reflection from a 50μm thick crystal in symmetric Bragg geometry. Red curve corresponds to the case where the effect of real absorption is ignored. Solid black curve shows the reflectivity of absorbing crystal. Rapid oscillations are due to the finite thickness of the crystal.

case	α	γ	$\Delta\theta_e^{cen}$	$\Delta\theta_e$	w_e	θ_e
Bragg	0	-1	$\Delta\theta_i^{cen}$	$\Delta\theta_i$	w_i	θ_i
Laue	$\pi/2$	1	$-\Delta\theta_i^{cen}$	$-\Delta\theta_i$	$-w_i$	$2\theta_B$-θ_i

Table 2.1: Exit beam quantities in terms of the corresponding incident quantities for the symmetric Bragg and Laue cases.

The results for symmetric Bragg and Laue cases are summarized in table 2.1.

2.2.3 Dumond diagrams

In eq. 2.32, $\Delta\theta_i = \pm w_i/2$ define two curves corresponding to the two ends of the Darwin width. One can then get the incident and exit angles:

$$\theta_i = \alpha + \theta_B + \Delta\theta_i^{cen} \pm w_i, \tag{2.34}$$

$$\theta_e = -\alpha + \theta_B + \Delta\theta_e^{cen} \pm w_e. \tag{2.35}$$

For a given range of λ, one can calculate two values for each of θ_i and θ_e and plot $\frac{\lambda}{2d}$ versus these angles. The results are often called *Dumond diagrams*. Although $\Delta\theta^{cen}$ and w are also functions of θ_B and, therefore, λ, they are rather small compared to the θ_B term and for a short interval, the Dumond diagrams look like straight lines called *Dumond reflectivity bands*, because, this is the region where the reflectivity is close to unity. These are helpful to map a given incident ray to the corresponding exit one. Examples of such curves for Si(111) surface in symmetric Bragg and Laue cases are plotted in Fig. 2.9. In this figure [+] and [-] signs correspond to the same signs in eqs. 2.34 and 2.35. Note that for the Symmetric Bragg case, the incident and

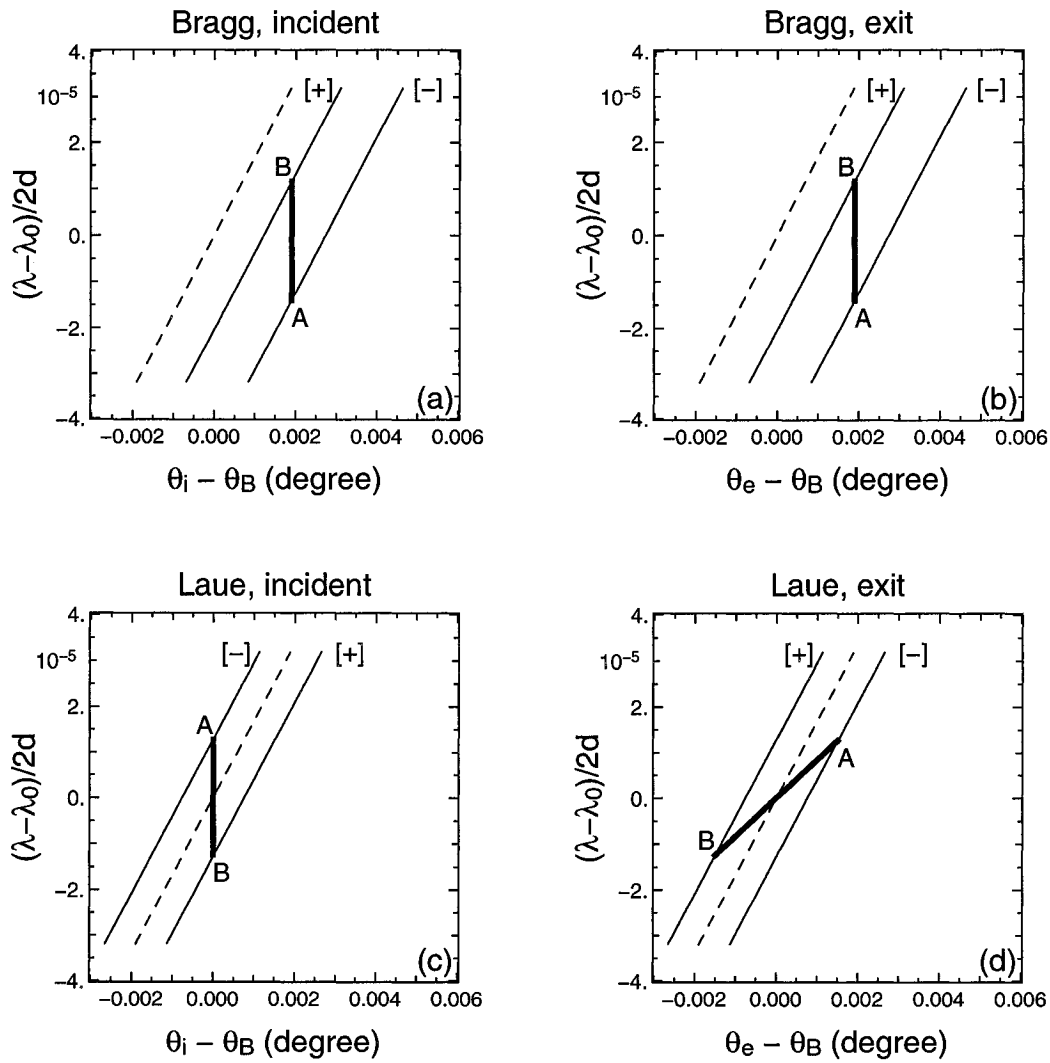

Figure 2.9: Dumond reflectivity bands For Si(111) reflection at λ_0= 1.653 Å. On the vertical axes d is the Bragg planes spacing. [+] and [-] show the two Darwin width edges. Dashed lines show the kinematical Bragg value. (a),(b) symmetric Bragg case: incident and exit angles are equal for all the wavelengths. (c),(d) symmetric Laue case: there is no shift due to refraction, however, rays with the same incident angle, but different wavelengths have different exit angles.

exit angles are always equal whatever the wavelength be. On the other hand, for the symmetric Laue case the upper and lower edges change position (see table 2.1) and even for the same incident angle, waves with different wavelengths leave the crystal with different exit angles.

2.2.4 Dynamical integrated intensity

In general, because of extinction and multiple scattering, the integrated intensity for perfect crystals is lower than the kinematical value (eq. 2.20) [for the cases we studied the extinction length is much smaller than the absorption length, so that the real absorption is not as important]. Even for mosaic crystals the integrated intensity is lower than the kinematical value, because, mosaic blocks have a finite size and dynamical effects like extinction and multiple scattering take place. To calculate the integrated intensity, one has to find the area under the Darwin reflectivity curve. Here we present the result for symmetric Bragg case [1]:

$$I_d = (\frac{8}{3\pi})\,\Phi_0\,\frac{A\lambda^2 r_0|F(\mathbf{q})|}{v_c}\,\frac{1}{\sin 2\theta}\,P. \tag{2.36}$$

2.3 X-ray microdiffraction techniques

In conventional x-ray diffraction, the measured intensity is an average over the entire diffraction volume (eq. 2.8). Therefore, the resolution of the experiment depends on the size of the beam and the acceptance angle of the detector. X-ray microdiffraction or *x-ray microscopy* means collecting x-ray diffraction data with micron or sub-micron spatial resolution on the sample. To achieve this goal, one can use a very narrow beam

to illuminate only a micron-size area of the sample. But, this will considerably reduce the number of photons that can be scattered from that area. A better way would be to focus the x-rays to a small area without losing intensity and then move the focused beam to the desired point on the sample. This is called the *microfocusing* or *x-ray microbeam scanning microscopy* technique. Another method is to use a wide beam with large cross section to illuminate a large area and then use a micron-resolution x-ray recording medium to spatially resolve the diffracted beam. This technique is often called *X-ray Diffraction Imaging* (XDI) or *x-ray topography*. The invention of high flux x-ray synchrotron sources and the developments of high resolution x-ray CCD cameras helped to improve this method but, in principle, it has been known and used for many years using conventional x-ray sources and high-resolution films as the recording media. Microfocusing, however, requires an spatially coherent x-ray source and a focusing device. This method was only realized after synchrotron sources and high quality focusing elements such as x-ray Fresnel zone plates became available. A detailed review of these techniques can be found in the references at the end of this thesis [103, 6, 13, 98]. In this section the two main techniques used in our experiments will be briefly reviewed.

2.3.1 X-ray microbeam scanning microscopy

Although the idea of x-ray microscopy by a focused x-ray beam was first introduced about 58 years ago [80], because of technological difficulties, it was not implemented until the recent developments in the tunable high-flux synchrotron sources and high quality x-ray focusing optical devices. The challenge was even more serious for hard x-rays ($\lambda = 0.1 - 10$ Å). This is because the normal index of refraction of materials

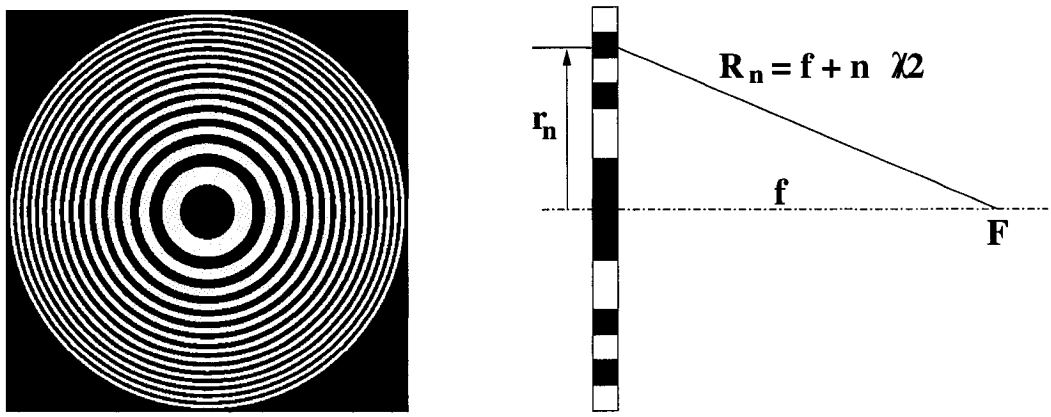

Figure 2.10: Fresnel zone plate. (a) front view, (b) side view to calculate the zone radius.

for x-rays is very close to unity and, therefore, a refraction-based "lens" is not so practical. A "diffraction grating" for x-rays must have periodicity in the order of the x-rays wavelength which is not very practical to make either. Unlike mirrors for light, there is no material to "reflect" x-rays and even the total reflection angle for x-rays is very small according to Snell's law.

Micromachining technology, high-precision design and engineering, and atom-resolution layer deposition methods have created different methods based on refraction, diffraction, and reflection to focus x-rays. These include Bragg-Fresnel lenses, Kirkpatrick-Baez mirrors, capillaries, compound refractive lenses, and Fresnel zone plates. A description of these devices can be found in the references at the end of this thesis [98]. Here we briefly introduce the Fresnel zone plates which are the most popular devices and were used in our experiments to focus hard x-rays. A Fresnel zone plate is a circular diffraction grating consisting of concentric alternating rings of two different materials (Fig. 2.10). The rings are designed so that the optical path from each ring to the focal point F on the symmetric axis of the zone plate differ by

$\lambda/2$ for the neighboring rings, where λ is the wavelength of the x-rays. If the out-of-phase zones are blocked or their phase difference π is somehow compensated for by passing through the zone plate, waves reaching the focal point from all the zones will constructively interfere and the result will be a strong focused beam at this point.

From Fig. 2.10 an equation can be derived for the radius of the nth zone:

$$\begin{aligned} r_n &= (R_n^2 - f^2)^{1/2} = [(f + n(\lambda/2))^2 - f^2] \\ &\simeq (nf\lambda)^{1/2} = \sqrt{n}\, r_1, \end{aligned} \tag{2.37}$$

where f is the focal length of the plate and we have assumed that $f \gg n\lambda$. This is generally true as f is typically a few millimeters and the number of zones on the order of a few hundreds. So the radius of the rings is proportional to the square root of integer numbers and the proportionality constant is equal to $r_1 = \sqrt{f\lambda}$, the radius of the central disk. The width of each zone, Δr_n can be also estimated:

$$\begin{aligned} \Delta(r_n^2) &= r_n^2 - r_{n-1}^2 = f\lambda \\ \rightarrow 2r_n \Delta r_n &\simeq f\lambda \\ \rightarrow \Delta r_n &= \frac{r_n}{2n} = \frac{r_1}{2\sqrt{n}}. \end{aligned} \tag{2.38}$$

If the spatial coherence of the beam is equal or bigger than the size of the zone plate, the lateral size of the focal spot, Δs, will be diffraction-limited and determined by the Rayleigh criterion [12]:

$$\Delta s = \frac{1.22 \Delta r_N}{m}, \tag{2.39}$$

where Δr_N is the width of the outermost zone and m is the diffraction order. Fresnel

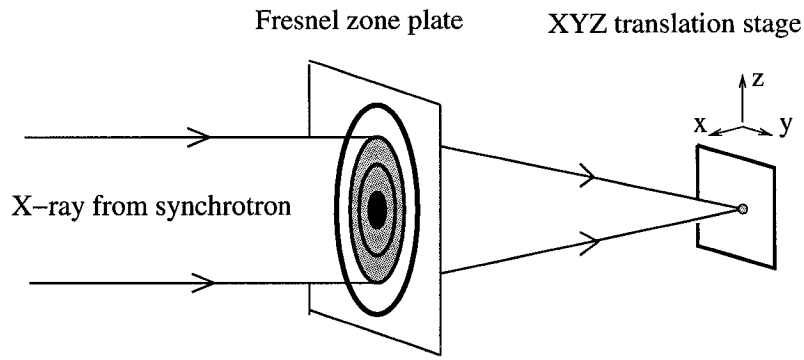

Figure 2.11: X-ray microfocusing setup

zone plates for x-rays are usually made by very high resolution electron lithography. Fig. 2.11 shows a typical microfocusing setup: the sample can be moved with respect to the focused beam using a translation stage to get x-ray diffraction data from the desired region.

2.3.2 X-ray diffraction imaging (topography)

X-ray diffraction imaging is a technique to identify long range distortions and strain fields in crystals. In this method the incident beam is not necessarily small, but the diffracted beam is spatially resolved by a high-resolution detector. In this section we will present a qualitative description of the main principles and techniques of XDI. Our emphasis will be on the plane wave diffraction imaging method used in this thesis. The excellent book by Authier [6] provides more detailed descriptions of these methods, as well as, many references on each specific subject.

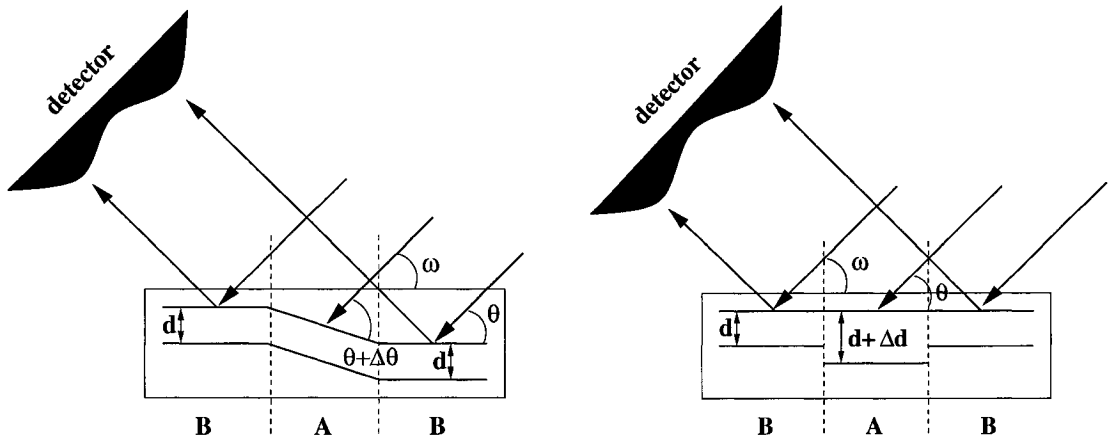

Figure 2.12: (a) Pure lattice disorientation. (b) Pure lattice strain

2.3.3 Source of contrast in XDI

First question when studying XDI is the most fundamental one: how the lattice imperfections are distinguished in the recorded image? Two main mechanisms are responsible for contrast in XDI images:

Suppose a region A in the crystal is disoriented with respect to the rest of its surrounding lattice B. The crystal is set to satisfy the Bragg condition for the normal region B and the diffracted beam is recorded by an extended detector (Fig. 2.12(a)). For monochromatic radiation, if the lattice rotation angle $\Delta\theta$ for region A is within the width of the rocking curve of the crystal, Bragg condition will be only partially satisfied for this region and the diffracted beam will have lower intensity than the rest of the crystal. If disorientation is more than the width of the rocking curve, region A will not satisfy the Bragg condition at all and this area will appear dark in the image. If polychromatic radiation is used and the region A still satisfies the Bragg condition for some wavelength in the spectrum of the incident beam, the diffracted

rays will have a different orientation than the rest of the crystal. This will also cause contrast on the image by redistributing the intensities. This is, accordingly, called *orientation contrast*. The disorientation angle $\Delta\theta$ can be measured by rotating the crystal by $\Delta\omega_o = -\Delta\theta$ to bring region A to diffraction condition and strong intensity from this area is observed. It is important to note that this type of contrast can have a completely different origin. As illustrated in Fig. 2.12(b), suppose that in region A there is no disorientation, but the lattice spacing is different from its surrounding (strained lattice, for example). Again if the Bragg condition is met for region B, region A will not satisfy the diffraction condition and, therefore, will appear weaker or dark on the image. In this case the rotation angle $\Delta\omega_s$ needed to bring region A to maximum diffraction can be calculated from Bragg's law:

$$\Delta\omega_s = -\tan\theta\,\frac{\Delta d}{d}, \tag{2.40}$$

where Δd is the change in the lattice constant d. This can be confused with an equal lattice disorientation. However, since the lattice constants in these two cases are different, so will be the diffraction angle 2θ. The angle between the diffracted and incident beams will be equal to $2\sin^{-1}(\frac{\lambda}{d})$ for a pure disorientation, and $2\sin^{-1}(\frac{\lambda}{d+\Delta d})$ for a pure strain. An analyzer crystal after the sample can serve as a filter to pass a certain direction of the diffracted beams to resolve the ambiguity.

The second contrast mechanism arises around local imperfections in a perfect crystal. For example, the contrast of a point defect or dislocation in a topographic image. The deformed lattice around these defects is no longer a perfect lattice and, depending on the magnitude of imperfectness, extinction reduces and the simple kinematical approximation is appropriate to describe the diffraction. As we've seen

in sec 2.2.4, integrated intensity in the kinematical approximation is greater than the dynamical theory for the same lattice because of the lack of extinction and multiple reflections. This enhances the diffracted intensity form the defected areas and this type of contrast is, therefore, called *extinction contrast.* Obviously if extinction breaks down, but there is no more material to contribute to the kinematical diffraction, there will be no enhanced intensity. In order to observe this type of contrast, the crystal must be thicker than the extinction length of the x-rays.

2.3.4 Techniques of x-ray diffraction imaging

In general XDI can be done either in reflection (Bragg) or transmission (Laue) geometries. However, several techniques have been developed since the invention of XDI. Here a short review of the most important ones will be given and compared.

2.3.4.1 Berg-Barrett technique

This is a single crystal reflection topography technique. Although it was first introduced by Berg [10] in 1931 to observe the trace of scratches on the surface of sodium chloride crystals, because of its simplicity and efficiency, has been improved by many others and still is being used. To understand the geometry used in this technique, let's consider the simplest possible diffraction imaging setup. A source of size h_i in the diffraction plane (the plane defined by $\mathbf{k}_i$ and $\mathbf{k}_o$ in Fig. 2.4) is used to illuminate the sample at distance L and an extended detector at distance l records the diffracted rays (Fig. 2.13). The spatial resolution of the image depends on many factors including the *geometrical resolution.* If all the rays reaching the point P on the sample are within the rocking curve of the crystal, then geometrical size of the image on the

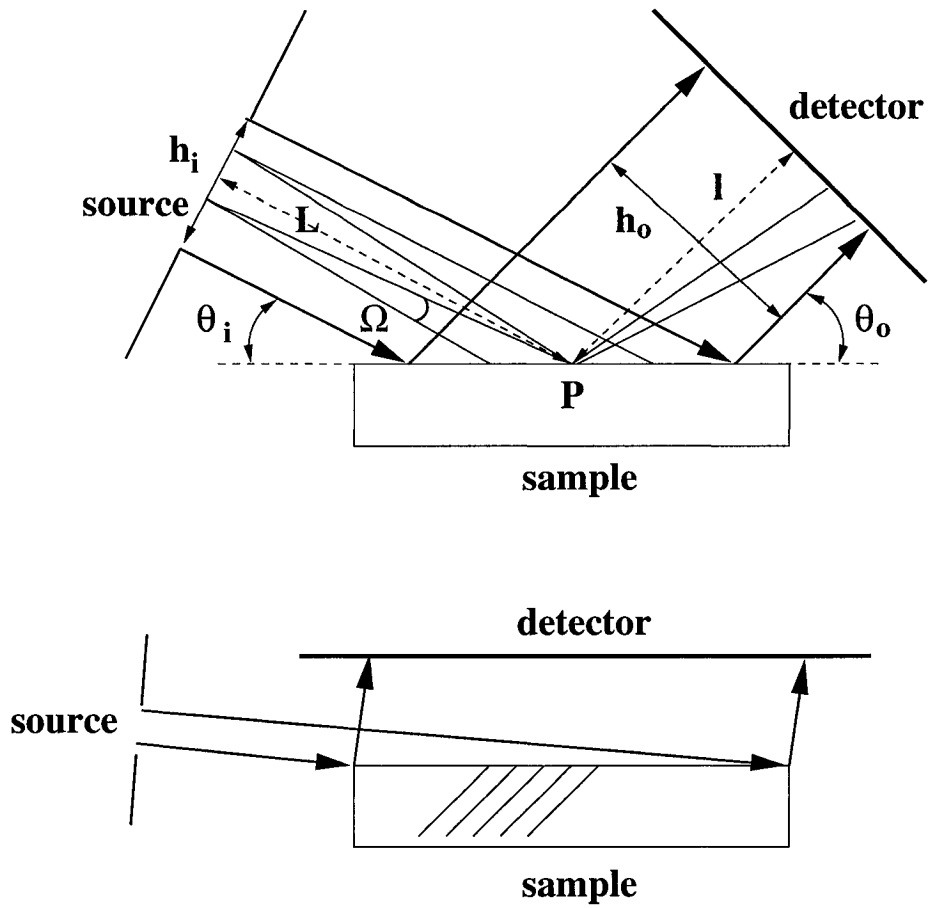

Figure 2.13: Berg-Barrett technique: best spatial resolution is achieved when a small source at far distance is employed, the incident beam is at grazing angle with the crystal surface, and the crystal cut and diffracting planes are set so that diffraction is almost perpendicular to the surface.

detector will be:

$$s = l\,\omega, \tag{2.41}$$

where $\omega = \frac{h_i}{L}$, the angle subtended to the source at point P or $\omega = \Omega$, the natural divergence of the source, whichever smaller. This immediately implies that better resolution is achieved by using a small source very far from the sample (or a very low divergence source), and placing the detector as close as possible to the sample. If the detecting surface is placed parallel and very close to the sample, the sample-detector distance and, therefore, resolution will be the same and maximum for all the points. The size of the illuminated area on the sample and the corresponding size of the total image on the detector will be also determined by simple geometry:

$$A = \frac{h_i}{\sin\theta_i}, \tag{2.42}$$

$$h_o = \frac{A}{\sin\theta_o} = h_i \frac{\sin\theta_o}{\sin\theta_i}, \tag{2.43}$$

where, θ_i and θ_o are the incident and exit angles respectively. Therefore, to cover a bigger area of the sample and have a maximum magnification on the image, θ_i should be very small (grazing angle incident) and θ_o close to 90° . Fig. 2.13 shows a Berg-Barrett XDI setup. X-rays from a small source (a fine focus x-ray tube or a synchrotron source) are incident on the sample at grazing angle. The crystal is cut so that for a suitable diffraction order the diffracted rays are as close as possible to normal to the surface. The other factor that should be considered concerning the resolution is the resolution of the detector itself. When films are used, the image is directly recorded on a nuclear emulsion plate. In case of CCD or TV cameras, x-rays hit a phosphor screen and the optical image produced this way is recorded by

an optical CCD. To record a noticeable trace of x-rays, they have to cross a certain thickness of the film or phosphor screen which will smear the image. To minimize this effect, the sensitive plate must be as thin as possible and placed normal to the x-rays. Inclined beams will have a bigger trace after passing a certain thickness. high efficiency films and use of soft x-rays ($\lambda > 10$ Å) will help to reduce the film thickness. The following advantages of synchrotron sources compared to laboratory sources make them preferable for this technique:

1. Small size, large source-sample distance, and well collimated beam of a synchrotron source increase the resolution of the image.

2. Low divergence of a synchrotron source makes it possible to place the detector far from the sample which facilitates the instrumentation.

3. High flux of photons makes it possible to choose higher order and weak Bragg reflections to fulfill the requirement for the exit beams being normal to the surface. The high intensity also reduces the exposure time of the detector.

2.3.4.2 Section and Projection topography techniques

Section topography or *Lang topography* is a transmission technique first invented by Lang in 1958 to observe dislocations in silicon crystals [84]. Fig. 2.14 shows a schematic of this technique. A fine ($\sim$10 μm) x-ray beam is incident on the sample at some angle to satisfy the Bragg condition for the desired reflection. The diffracted beam goes through a series of multiple reflections inside the crystal and, as a result, two wide bands of diffracted and direct beams emerge from the exit surface of the crystal. The diffracted beam, therefore, images a small three dimensional region inside

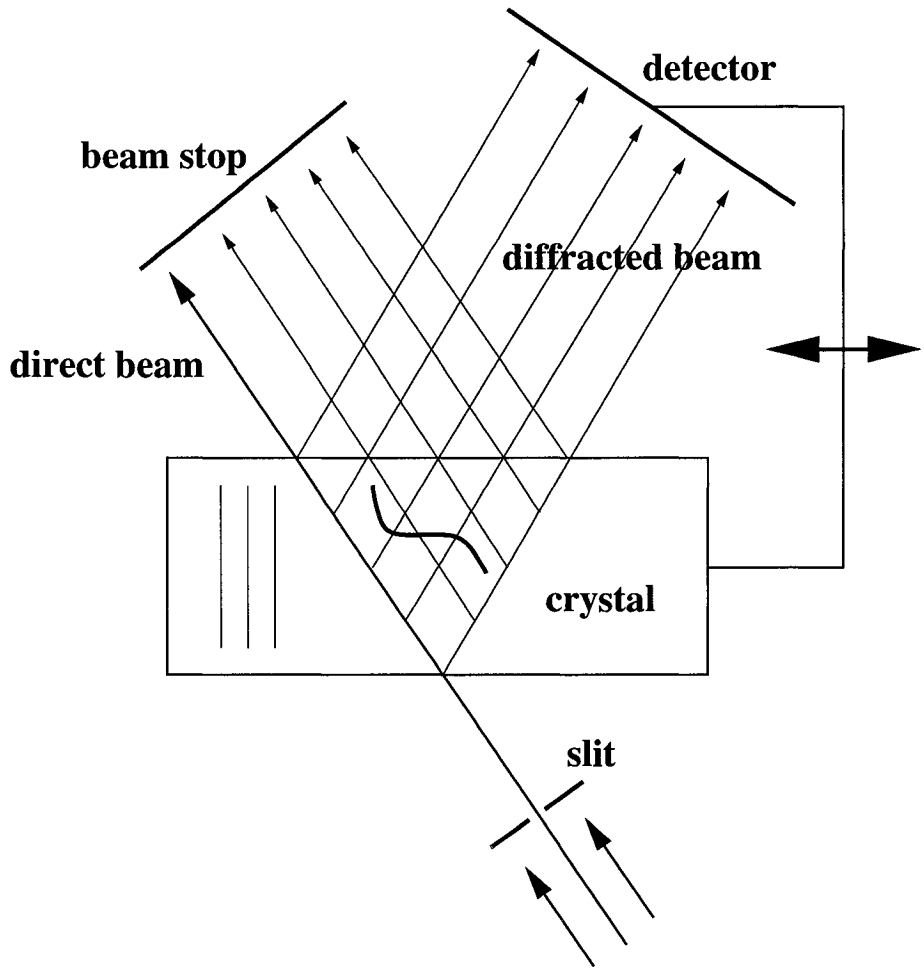

Figure 2.14: Lang topography technique: multiple diffractions of the incident beam produce a 3-D image of the imperfections in a *section* inside the crystal. To cover bigger areas, the detector and sample are translated together with respect to the incident beam. The result is then called a *projection topography.*

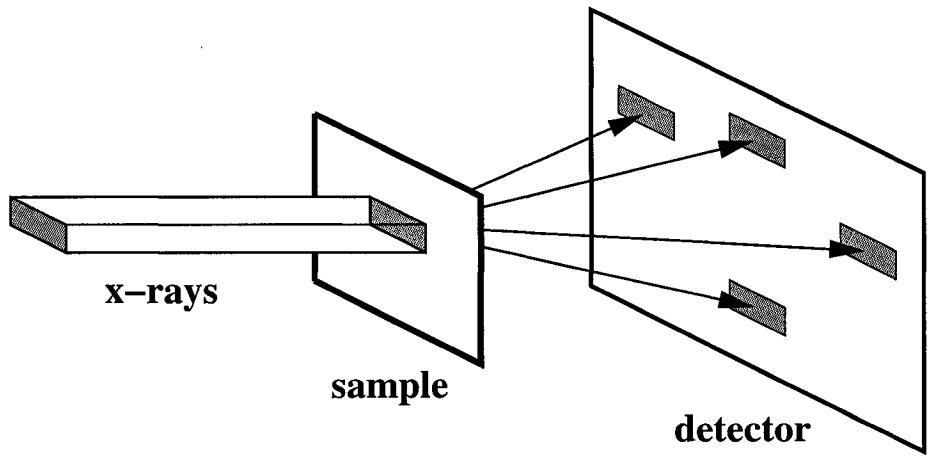

Figure 2.15: White beam topography: Laue spots form simultaneously for different wavelengths in the white incident beam.

the crystal, named a "section" by Lang. To cover bigger areas, sample and detector are translated together with respect to the incident beam keeping the diffraction condition valid. This way, an image of the defects in the crystal is projected to the film and, hence, the name *projection topography.*

2.3.4.3 White beam topography

This is a simple transmission technique which takes advantage of the continuous wavelength spectrum of synchrotron radiation. X-rays from a synchrotron source hit the sample and different atomic planes satisfying Bragg condition for different wavelengths in the beam form diffraction patterns, called *Laue patterns*, on the detector (Fig. 2.15). Each Laue spot is itself a topograph of the illuminated area at some wavelength. For a synchrotron, the x-ray source is small and very far from the sample. So, the detector can be placed far enough from the sample (see sec. 2.3.4.1) to observe the details of each Laue spot. White beam topography has the advantage

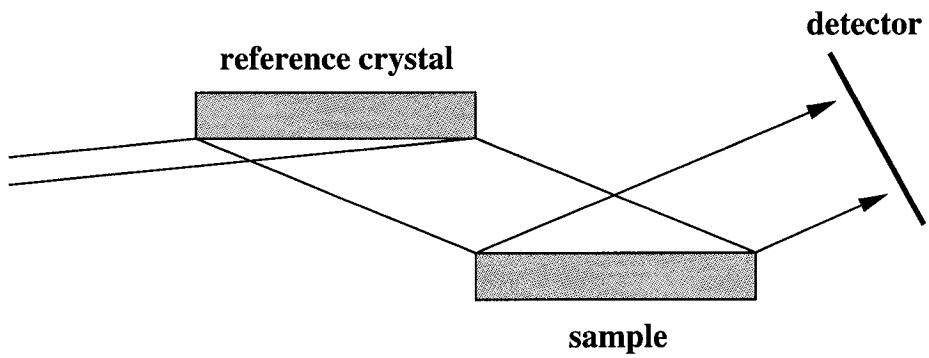

Figure 2.16: Double crystal topography

that several reflections form at the same time and there is no need to reorient the crystal to observe different reflections. As an example, Kawado [74] used synchrotron white beam topography to get a 3-D map of dislocations in silicon wafers.

2.3.4.4 Double crystal topography

This technique was first introduced by Bonse [11] in 1958 to study single dislocations. A good review of the applications of this method is given by Hart [56]. In this method the incident beam first diffracts off a high quality reference crystal before reaching the sample (Fig 2.16). The divergence of the beam after reflecting from the reference crystal is no bigger than the rocking curve of this crystal. Reflection from the reference crystal is usually asymmetric to collimate the beam used for the sample. This expands the beam and at the same time decreases the beam divergence. The sample is set so that the intensity is at the FWHM of the rocking curve of the sample. This method is very sensitive to small lattice distortions and strain, because, any small changes in the local lattice orientation or spacing causes a rapid and almost linear change in the intensity.

2.3.4.5 Plane wave XDI

In the double crystal method, the rocking curve of the reference crystal must be as narrow as possible to increase the sensitivity of the method. An even more sensitive technique can be realized by using an almost plane wave for diffraction from the sample. The idea was first implemented by Authier [7] in 1961 using a narrow slit to allow only the central part of the beam diffracted by a nearly perfect crystal in transmission mode, pass to the sample. Synchrotron sources have made plane wave topography much more practical, powerful, and precise to map very small lattice distortions. Often a plane-wave monochromator or a set of crystals are used to produce a nearly plane beam with large cross section from a synchrotron x-ray beam. The small size of the source and large source-sample distance allows for high resolution and bigger sample-detector distance. Also the tunability of synchrotron sources provides the choice of wavelength. This technique has been used, for example, by Chikaura [24, 25] to study microdefects in thin silicon crystals, Kitano [81] to detect lattice distortions as small as 0.2 arc second in big 6 inches silicon wafers, more recently by Kimura [77] with varying magnification to measure dislocations in silicon with less than 0.5 μm spatial resolution, and by Kawado [73] to measure surface strain in silicon wafers. Plane wave topography is the ideal method to measure very small lattice distortions. A good review of this technique and comparison with other methods is given by Hart [56]. First a series of images are taken for different positions of the rocking curve of the sample. Then, the sample is rotated about the diffraction vector $\mathbf{q}$ (Fig. 2.4) by 90, 180, and 270 degrees and the images are repeated. Changes in lattice parameters for a given area with respect to a reference area on the sample are determined by comparing the peak positions of the reflectivity curves for the two

places. Placing an analyzer crystal before the detector helps to distinguish between lattice spacing and lattice disorientation. It is fundamentally important to differentiate between these two. For example, Ishikawa [63] used this modification to map the equi-spacing contours in GaAs single crystals. Following Bonse assumption [103] that the contrast arises from local deviations from Bragg's law, the total change in Bragg angle, $\Delta\theta_B$, can be imagined to consist of two parts: a true lattice rotation, $\delta\theta_B$, and a change due to lattice strain, $\frac{\delta d}{d}$:

$$\Delta\theta_B = \delta\theta_B + \frac{\delta d}{d} \tan\theta_B. \tag{2.44}$$

These are two different phenomena which should be well separated when studying deformations in crystals. We have addressed this issue in our study of silicon cantilever in proper way. (See chap.4).

Chapter 3

X-ray microdiffraction study of 90° domains in barium titanate

Ferroelectrics are materials that have an electric dipole moment even in the absence of an external electric field. What distinguishes ferroelectrics is the fact that it is possible to reverse the polarization by applying a sufficiently strong electric field. This is the main property used in many of their applications. Ferroelectricity has been known for a very long time. Teophratus (a Greek author) mentioned that "lyngourion" (tourmaline, probably) attracted little pieces of wood when cooled down after heating. Ferroelectricity in its modern form was discovered by Valasek [121] in 1921. The first ferroelectric crystal discovered in modern ages was Rochelle salt [122]. Since then many other simple and complex ferroelectric materials have been discovered and studied. Regarding their chemical formula, ferroelectrics are classified in two groups: materials with hydrogen bounds, such as KH_2PO_4 (KDP) and TGS (triglycine sulfate), and double-oxides such as $BaTiO_3$, $LiTaO_3$, $LiNbO_3$, $PbTiO_3$, $KNbO_3$, etc. Because of their very high dielectric constant, ferroelectrics have been used to make high capacity capacitors. Some ferroelectrics including $BaTiO_3$, $LiTaO_3$, and $LiNbO_3$ are transparent to light and are used in optical devices such as optical switches [137].

They have been also used as micro-sensors and actuators [99]. The most recent (and, perhaps, the most important) application of ferroelectric crystals is the Non-Volatile Random Access Memories (NVRAMs)[124, 32, 64, 5, 99]. In this type of RAM memories ferroelectric domains are used as the storing units to store the information. Unlike conventional memories, once the information is stored, no voltage is needed to keep it which has several practical advantages.

In this chapter we briefly review some physical aspects of ferroelectrics relevant to our study. There are good classic texts [86, 137] and reviews [30, 37, 28, 31] available on the general theory of ferroelectricity and their applications. We also review the most important work done in this field with particular emphasis on Barium Titanate, the material studied in this thesis. A detailed description of the experimental setup and the results will follow the theory section.

3.1 Physics of Ferroelectricity

Ferroelectrics are materials that in a certain range of temperature develop spontaneous electric dipole moment. In this regard they are pyroelectric, but, what distinguishes them is that the electric dipole moment in ferroelectric materials can be reversed by applying a sufficiently large electric field. In ferroelectrics dipole moments develop when the material undergoes a phase transition from a high symmetry *paraelectric* phase to a low symmetry *ferroelectric* phase. The ferroelectric state is the state with a non-zero *spontaneous polarization*, $\mathbf{P_s}$. The transition temperature is called the *Curie Temperature*, T_c. Table 3.1 lists some well known ferroelectric materials with their T_c and P_s values. Phase transition in ferroelectrics can be best understood in a phenomenological treatment given by Landau and Ginzberg[82, 132].

Material	T_c (C)	P_s (μC cm^{-2} at RT)
KH_2PO_4	-150	4.75
TGS	49	2.8
$BaTiO_3$	-90,0,120	26
$LiNbO_3$	1210	71
$LiTaO_3$	620	50
$PbTiO_3$	490	75

Table 3.1: Some ferroelectric crystals.

The free energy per unit volume, $\mathcal{F}$, of a crystal with center of symmetry can be expanded in a power series of the polarization P value (the *order parameter*):

$$\mathcal{F}(P,T,E) = -\mathbf{E}\cdot\mathbf{P} + \mathcal{F}_0 + \frac{1}{2}\alpha P^2 + \frac{1}{4}\beta P^4 + \frac{1}{6}\gamma P^6 + \cdots, \tag{3.1}$$

where for generality the interaction energy with an electric field $\mathbf{E}$ has been also added. In principle, α, β, and γ can be functions of temperature T. Because of the assumed symmetry, only even powers appear in the series. The equilibrium state corresponds to the value of P that minimizes the free energy:

$$\mathcal{F}' = \frac{\partial \mathcal{F}}{\partial P} = -E + \alpha P + \beta P^3 + \gamma P^5 = 0, \tag{3.2}$$

$$\mathcal{F}'' = \frac{\partial^2 \mathcal{F}}{\partial P^2} > 0, \tag{3.3}$$

where E is the electric field in the direction of polarization. To derive the principle concepts, we first assume that there is no external electric field. If we consider only the square term in free energy, equilibrium state only occurs at $P_s = 0$. Next approximation is to take the first two terms and set γ to zero. Then we get:

$$P_s = \begin{cases} 0, \\ \pm\sqrt{-\frac{\alpha}{\beta}}, \end{cases} \tag{3.4}$$

and the corresponding second derivatives:

$$\mathcal{F}'' = \begin{cases} \alpha, \\ -2\alpha. \end{cases} \tag{3.5}$$

Therefore, α should be positive for $P_s = 0$, and negative for $P_s \neq 0$ in order to have a local minimum in the free energy. This requires α to change sign at some temperature, T_0, so that α becomes negative for $T < T_0$:

$$\alpha = a(T - T_0), \tag{3.6}$$

where a is another constant. T_0 is, therefore, the temperature below which the material gains spontaneous dipole moment. This is by definition the Curie temperature, $T_c = T_0$. Equation 3.4 requires that $\beta > 0$. If $\beta < 0$, there will be no ferroelectric phase in this approximation and, therefore, the P^6 term in eq. 3.1 must be also considered. Let's first consider the case where $\beta > 0$. Figure 3.1(a) shows the free energy curves below, at, and above the transition temperature T_c for this case. As can be seen from these graphs, the polarization continuously changes from $P_s = 0$ to

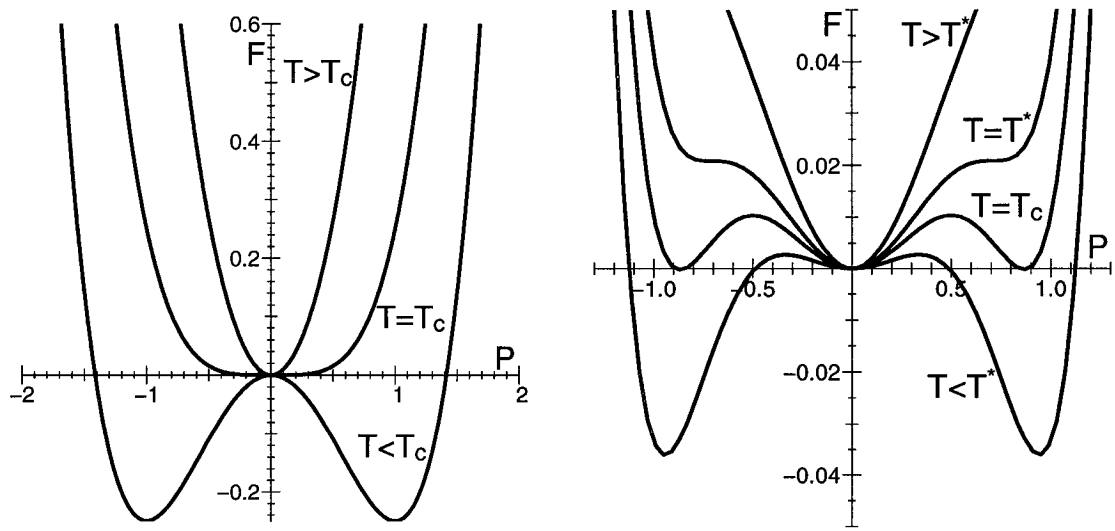

Figure 3.1: Phase transitions in ferroelectric crystals. (a) Continuous (second order) phase transition. (b) Discontinuous (first order) phase transition.

$P_s = \sqrt{\frac{-\alpha}{\beta}}$ as temperature decreases from above to bellow the transition temperature. This is, therefore, called a *continuous* or *second order* phase transition. Ferroelectric transition in lithium tantalate, $LiTaO_3$ is of this kind. If $\beta < 0$, we need to keep the P^6 term. In this case the equilibrium values for the polarization are:

$$P_s^2 = \begin{cases} 0, \\ \sqrt{-\frac{\beta}{2\gamma}}\,(1 \mp [1 - \frac{4\alpha\gamma}{\beta^2}]^{1/2}). \end{cases} \tag{3.7}$$

This requires that $\gamma > 0$ and

$$[1 - \frac{4\alpha\gamma}{\beta^2}]^{1/2} > 0 \rightarrow T \leq T^*, \tag{3.8}$$

where the *tricritical temperature* T^* is defined as bellow:

$$T^* \equiv T_0 + \frac{\beta^2}{4a\gamma}. \tag{3.9}$$

If $T_0 < T \leq T^*$ the free energy curve will have two local minima other than the one at $P_s = 0$. The free energy curves for this case are plotted in Fig. 3.1(b). For some temperature $T_c < T^*$ the local minima at $P_s \neq 0$ will have the same values as the one at $P_s = 0$. At this transition temperature the polarization can suddenly jump from zero to some nonzero value. This is, therefore, called a *discontinuous* or *first order* phase transition. Ferroelectric phase transition in $BaTiO_3$ is of this kind.

From structural point of view, phase transition in ferroelectric crystals is either *displacive* or *order-disorder* types. In a displacive ferroelectric phase transition (like phase transition in the Perovskite family with ABO_3 generic formula, including $BaTiO_3$) ferroelectricity is a result of displacement of ions which results in separating the centers of the positive and negative charges in the unit cell (see sec. 3.2 for more details). In this type of transition when an atom is displaced from its equilibrium position, the force from the local electric field exerted on the atom grows faster than the restoring elastic force. As a result, a permanent polarization forms. This phenomenon is known as *polarization catastrophe.* At the beginning the electric field is large and the restoring force is small causing a fast development of the electric dipole moment. As the separation of the ions increases, so does the restoring force stopping the growth of the polarization at the equilibrium value. In the order-disorder ferroelectric transition, on the other hand, each individual unit cell has a dipole moment, but they are randomly oriented above T_c. Below T_c, they all point in the same direction in each domain. Ferroelectric materials with hydrogen bonds, for example,

KH_2PO_4 have this type of transition.

Electrical properties of ferroelectric crystals are directly related to the structure of their polarization state. For instance, the electric susceptibility is the ratio of polarization vector to the applied electric field. Here, as the first approximation, we can assume that $\beta = \gamma \simeq 0$. Then from eq. 3.2, and eq. 3.6 we get:

$$\chi = \frac{P}{E} = \frac{1}{a(T - T_0)}. \tag{3.10}$$

These quantities provide tools for the study of phase transition in ferroelectric materials by means of electric measurements.

According to eq. 3.4 and Fig. 3.1, in one dimension there are two equivalent minima for the free energy corresponding to $P = \pm P_s$. Similarly, in three dimensions the minima of the free energy corresponds to more than one equivalent state of polarization. Below the phase transition, different regions in the crystal can, in principle, have any of the energetically equivalent polarization states. Each one of these regions is called a *ferroelectric domain.* The boundary between two neighboring domains is called a *domain wall.* A multi-domain crystal costs more energy both because there is a positive surface energy (*surface tension*) associated to the domain walls, and also because in continuous variation of polarization from one domain to the other, polarization has to take values other than those of the minima which increase the free energy. This extra energy is often called *domain wall energy.* Therefore, ideally, a single domain state is energetically more favorable. What, however, change the situation are the crystal surfaces. Fig. 3.2 demonstrates a single-domain piece of crystal. Polarization creates surface charges of opposite signs on the crystal surfaces. Separation of positive and negative charges on the crystal surface costs electrostatic

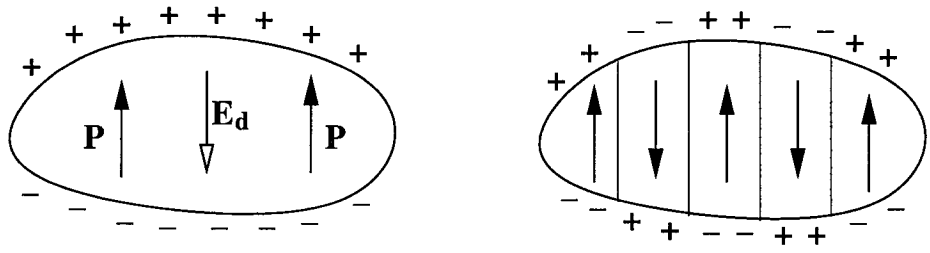

Figure 3.2: Domain formation in ferroelectrics. In a finite size single-domain ferroelectric crystal domains form to minimize the total electrostatic and surface energies.

energy making a single-domain state less desirable. In fact what happens is that these charges create a *depolarizing electric field* $\mathbf{E}_d$ inside the crystal in the opposite direction of the initial polarization which is strong enough to reverse the polarization of some regions and create a multi-domain structure. The equilibrium state of the crystal is determined by competition between the electrostatic energy of the polarization charges on the surface and the domains wall energy. Crystal defects can also force the crystal to form domains again because of the concentration of charges. Formation of domains creates another problem. Polarization charges can accumulate on the domain walls, if the normal component of the polarization vector varies across the wall. To reduce this effect, ferroelectric domains arrange their orientations so that the electrostatic energy becomes minimum. This often creates antiparallel or head-to-tail configurations (see sec. 3.2). It is important to realize that a perfect and infinite ferroelectric crystal would consist of only one single domain. In practice, ferroelectric crystals usually consist of many domains randomly oriented in the possible directions. The average dipole moment in the macroscopic scale is, therefore, zero. By applying a sufficiently large electric field the dipole moments of the domains can be aligned so that they have a non-zero component in the direction of the field. This process is called *polling*. To pole a ferroelectric crystal, usually, the temper-

ature is risen above the transition temperature, then, an electric field is applied to the crystal in the proper direction and the crystal is cooled down slowly [51]. By definition, ferroelectric domains polarization can be reoriented at room temperature by applying a large electric field known as *coercive field* E_c . *Polarization switching* is a rather complicated phenomena which involves heterogeneous nucleation of new domains and forward and/or sidewise motion of domain walls to create the new state of polarization [86, 97]. Ishibashi [62] proposed a lattice model to explain polarization reversal in ferroelectrics. The velocity of sideway motion of domain walls follows an exponential law [97]:

$$v = v_\infty e^{-\frac{\delta}{E}}. \tag{3.11}$$

where E is the applied electric field and δ is called the *activation field.* This formula implies a nucleation process for the sidewise motion of domain walls. Many of the applications of ferroelectric crystals are based on polarization switching. For example, in NVRAMs information is written by switching the polarization of domains in certain regions of the crystal [124]. It is known that domain wall motion plays an important role in polarization switching. The formation of domains in ferroelectric crystals often creates strain fields around the domain walls. This is mostly because neighboring domains have different lattices which have to match in the domain wall region. Many static and dynamic properties of ferroelectrics depend on the fine structure of domain walls and the associated strain field around them. Strain field and domain wall structure are also important factors in the crystal *fatigue* (change of the ferroelectric properties by time) which affects domain switching in ferroelectric devices [40]. Experimental results for many ferroelectric crystals show that the strain field around domain walls usually expand well beyond the domain wall area [76, 112, 66].

3.2 The structure of ferroelectric domains in $BaTiO_3$

Ferroelectricity in barium titanate, $BaTiO_3$, was first discovered by Wul [136] in 1946. $BaTiO_3$ belongs to the Perovskite family with ABO_3 generic structure with A and B being mono- (or divalent) and tetra- (or pentavlent) metals. Because of their simpler structure compared to older compounds and, of course, their applications, $BaTiO_3$ and other ferroelectrics from Perovskite family, such as $PbTiO_3$, $KNbO_3$, $LiNbO_3$, and $LiTaO_3$ attracted a lot of attention. Now, $BaTiO_3$ is one of the most studied ferroelectrics and is considered a classic example of ferroelectrics materials. In 1950 Mason and Matthias [90] proposed a theoretical model to describe the structural phase transition in $BaTiO_3$. Devonshire [34, 35, 36] described a macroscopic thermodynamic theory of phase transition in $BaTiO_3$. In 1960 Cochran [26, 27] explained the microscopic theory of ferroelectricity in $BaTiO_3$ in terms of lattice dynamics. $BaTiO_3$ undergoes several phase transitions: It has cubic lattice in paraelectric phase above 120 °C. between 120 °C to 0 °C it is in ferroelectric phase and has tetragonal structure with polarization vector along one of the $\langle 100 \rangle$ directions of the cubic phase. Below 0 °C it remains ferroelectric, but the structure changes. Between 0 °C to -70 °C the structure is orthorhombic with polarization along one of the $\langle 110 \rangle$ directions of the cubic phase. Below -70 °C the rhombohedral phase is stable with polarization along one of the $\langle 111 \rangle$ cubic directions. The paraelectric to ferroelectric phase transition at 120 °C is responsible for ferroelectricity at room temperature. The transition is a first-order displacive type. Fig. 3.3 illustrates the structural change during this transition. Ba^{2+} ions are at the corners, Ti^{4+} at the center, and O^{2-} ions at the faces centers. because of the symmetry, the center of positive and negative charges coincide and there is no net polarization in the unit cell. Upon transition, structure changes

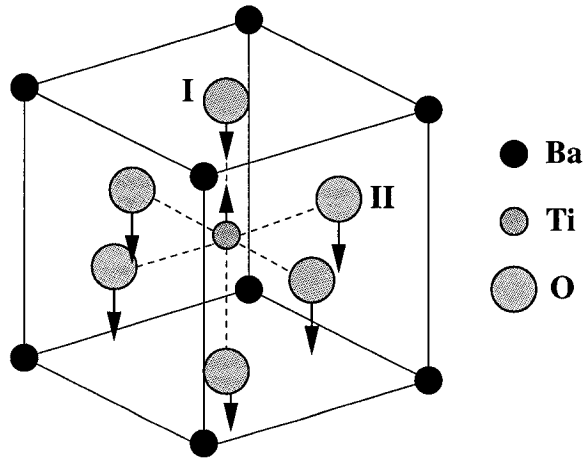

Figure 3.3: Structural phase transition in $BaTiO_3$: A dipole moment develops when positive and negative ions are displaced relative to each other at 120 °C.

from cubic to tetragonal (a= 3.9945 Å and c = 4.0335 Å) with $P4mm\,(C_{4v})$ space group. The lattice distortion is given by $\frac{c}{a}$ ratio which is $\sim$ 1.01 for $BaTiO_3$. Taking the barium atoms as reference, the octahedra of O^{2-} moves a little down and the titanium ion moves in the opposite direction separating the centers of positive and negative charges and creating a dipole moment in the unit cell. There are two types of oxygen ions in the unit cell: the two on the top and bottom (type I) have different displacements than the ones on the faces (type II). Table 3.2 lists the atom positions and relative displacements for different ions during the phase transition [55]. Because of the six-fold cubic symmetry before the transition, all the six cubic $\langle 100 \rangle$ directions are energetically equivalent and the dipole moment can, in principle, develop along any of these six directions when the crystal undergoes the phase transition. This results in domains with anti-parallel (180°) or perpendicular (90°) polarizations (Fig. 3.4(a)). To minimize the electrostatic energy, the polarization vectors in the neighboring 90° domains align to form charge-natural walls and, therefore, follow a

Atom	Position	Displacement (Å)
Ba	0,0,0 (origin)	0.0
Ti	$\frac{1}{2}, \frac{1}{2}, \frac{1}{2} + \delta Z_{\mathrm{Ti}}$	0.0135
O_I	$\frac{1}{2}, \frac{1}{2}, \delta Z_{O_I}$	-0.024
O_{II}	$\frac{1}{2}, 0, \frac{1}{2} + \delta Z_{O_{II}}$; $0, \frac{1}{2}, \frac{1}{2} + \delta Z_{O_{II}}$	-0.0150

Table 3.2: Atoms displacement during phase transition in $BaTiO_3$ (From x-ray and neutron measurements by Harada et al [55])

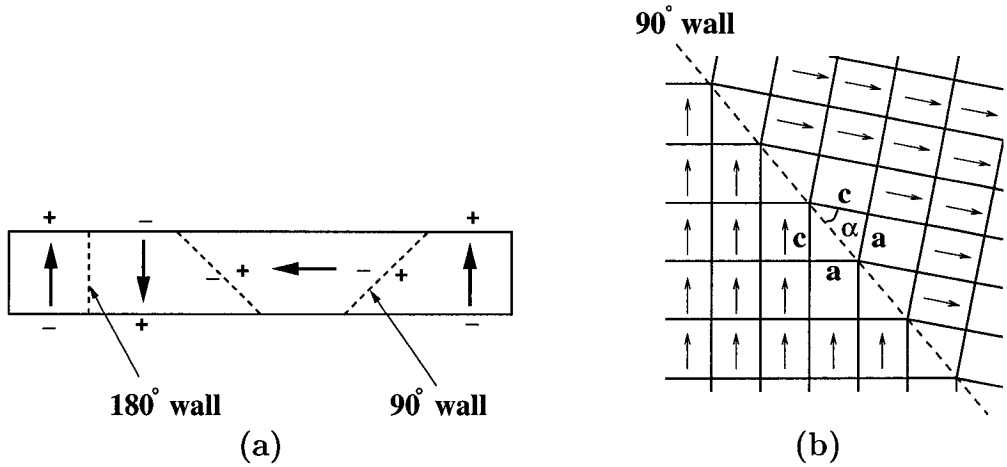

Figure 3.4: Orientation of domain walls in $BaTiO_3$. (a) 180° and 90° walls. (b) Lattice matching across a 90° domain wall.

head-to-tail arrangement. The lattices across the domain walls should match together to relieve the strain. *Twinning* is the phenomenon when two lattices share some crystal sites. Cao et al. [17] did a full study on twinning in 90° and 180° domains in Perovskite crystals. Fig. 3.4(b) shows a perfect lattice matching for two 90° domains. This defines the orientation of the wall with respect to the tetragonal axes of the two lattices:

$$\alpha = \tan^{-1}(\frac{a}{c}) \simeq 44.71°. \tag{3.12}$$

So, if the two lattices match perfectly, the angle between the polarization vectors (c axes) in the two adjacent 90° domains must be ~89.42° instead of 90°. The transformation of lattice from one domain to the other one takes place over a finite distance defined as *domain wall thickness.* In the case of 90° domains, there are two proposed scenarios for the change of the polarization vector from one domain to the other one: in the domain wall region the magnitude of the polarization vector diminishes gradually without rotation and then grows again in the perpendicular direction, or the polarization vector rotates by 90° as one moves from one domain to the other one. Experimental evidences are in favor of the second scenario [138]. The thickness of 90° and 180° domain walls and the associated domain wall energy are important factors in the subject of domain dynamics, for example, domain switching. For this reason they have been studied and debated for long time. Table 3.3 summarizes the results of some of the work done to measure wall parameters of $BaTiO_3$.

Merz [91, 92] used polarization electric measurements and optical microscopy to study the structure of domains in $BaTiO_3$ single crystals. Merz [93] and Little [87] used the same methods to study the dynamics of 90° and 180° domain walls. Miller and Savage [95, 96] specifically measured the sidewise motion of domain walls and

	σ_w (mJ/cm^2)		t_w (Å)	
Author	180°	90°	180°	90°
Padilla [107]	16	-	5.6	-
Merz [93]	7	-	1	-
Zhirov [141]	10	2-4	5-20	50-100
Yakunin [138]	-	-	-	50
Floquet [48]	-	-	-	40-60

Table 3.3: Domain wall surface energy, σ_w, and wall thickness t_w for $BaTiO_3$.

domain wall velocity in single crystal $BaTiO_3$. Optical techniques are applicable only to transparent crystals and have limited resolution. Transmission electron microscopy (TEM) has been used as an accurate method to investigate the domains structure in thin films of ferroelectric materials. For example, Yakunin et al. [138] studied the 90° domain walls in 500-2000 Å $BaTiO_3$ thin films. Snoeck at al. [125] used TEM to measure the motion of domain walls in $BaTiO_3$ thin films. Stemmer et al. [128] used TEM to measure the atomistic structure of domain walls in $PbTiO_3$, another Perovskite ferroelectric material similar to $BaTiO_3$. TEM, however, is only applicable to very thin films which may have different structure than the bulk samples. Scanning probe microscopy techniques have also been used to study mostly other ferroelectric materials. For example, Saurenbach et al. [120] used atomic force microscopy (AFM) to image domain walls in $Gd_2(MoO_4)_3$, a ferroelectric-ferroelastic crystal. Yang et al [139] successfully measured the motion of a single 180° domain wall in lithium

tantalate ($LiTaO_3$) single crystal with nanometer resolution using near-field scanning optical microscopy (NSOM) technique. Scanning microscopy techniques, although have very good spatial resolution, can only measure quantities on the surface of the sample and provide little information on bulk quantities such as internal strain and lattice rotation.

X-ray diffraction has always been a popular technique to investigate the structure and dynamics of ferroelectric crystals. The main advantages are that x-ray diffraction is a fast sensitive and non-destructive bulk probe with atom-size resolution that directly measures the lattice structure. Evans [44, 43] did a detailed x-ray study to determine the atoms positions in tetragonal $BaTiO_3$. Later, Harada et al. [55] compared x-ray and neutron diffraction methods to get more accurate data. More recently, Chandrasekaran et al. [21] emphasized on the importance of considering the anomalous scattering in noncentrosymmetric ferroelectric crystals including $BaTiO_3$. The study of domains and domain walls structure in $BaTiO_3$ with x-ray diffraction, however, doesn't have a very long history. Valot et al. [133] used the relative change in the intensities of $\langle 002 \rangle$ and $\langle 200 \rangle$ Bragg peaks when applying an electric field or heating the sample as an indirect measure of the evolution of 90° domains. They also attributed the profile of several Bragg peaks to the microstructure of 90° domains. In an extensive study, Floquet et al. [48] combined x-ray powder diffraction and high resolution TEM to investigate the fine structure of 90° domain walls in $BaTiO_3$. In particular, they studied the thickness of the walls and the effect of stress in shaping the walls, again in an indirect way used before [133]. In another work, Floquet and Valot [47] proposed a structural model to interpret the width of the 90° domain walls obtained in their x-ray measurements of powder $BaTiO_3$. They found that do-

main walls have internal structure and their width is about 16% of the grain size. More recently, there have been work to measure *in situ* dynamics of domain walls by x-ray diffraction. Zolotoyabko et al. [142] used x-ray pulses synchronized with a high-frequency electric field to measure the time dependent variations of the lattice parameters in thin films of single crystal $BaTiO_3$.

In all the work mentioned above, proper understanding of the internal microstructure of domains and domain walls is a key. X-ray microdiffraction seems to be the appropriate tool to directly address this issue. It can directly probe the bulk and surface microstructure of domains and domain walls in all types of ferroelectric materials. Some work have been done so far using this technique. Fogarty et al. [49] used high resolution XDI technique to image morphology of the antiparallel domains in thick $BaTiO_3$ crystals with 1-10 μm resolution. Using x-ray topography, Drakopoulos et al. [38] studied the inversion of 180° domains in $LiNbO_3$ and found that the domain walls thickness is in the order of 0.3 μm, larger than the theoretical values. Kim et al. [76] used x-ray topography to measure the strain field around 180° domain walls in $LiNbO_3$ and $LiTaO_3$ and found that strain field extends a few micrometers around the walls. Rogan et al. [112] carried out a direct measurement of strain field around domain walls in $BaTiO_3$ using a microfocused x-ray beam and found that, in contrast to theoretical calculations and previous measurements, the strain field extends several micrometers around 90° domain walls.

In most of the microstructure studies done so far, the measurements were indirect and based on pre-assumptions about the structure of domains and domain walls. A few cases where direct measurements of the structure of individual domains with fairly good resolution and accuracy were done [112], the results failed to provide a complete

description of the fine structure of the domain structure. For example, the important fact that the properties of domains and domain walls in the bulk and near the surface of the crystal are different, was not fully taken into account when interpreting the data. In the following sections we will explain how we exploited the power of x-ray microdiffraction combined with a detailed analysis to properly address some of the important problems related to the fine structure of 90° domains and domain walls in ferroelectric $BaTiO_3$ crystals.

3.3 The x-ray microfocusing experiment

Our experiment was done at the 8-ID side section of IMM/XOR-CAT (IBM, McGill, MIT, X-ray Operations,and Research Collaborative Access Team) beamline at the Advanced Photon Source, Argonne National Laboratory. We used two samples in our measurements. They both were zero-field-cooled 99.99% pure barium titanate single crystals from MTI Corporation [143] measured 5×5×1 mm with their bigger faces cut parallel to (100) planes. For rectangular shape ferroelectric samples, the 180° domain walls perpendicular to the crystal surface are commonly called $c-c$ domains where as 90° domain walls at 45° to the surface (like our sample), and 90°domain walls perpendicular to the surface are referred to as $a-c$ and $a-a$ domain walls, respectively. Both Our crystals had stripe-shape 90° domains with their polarizations parallel and perpendicular to the crystal surface. These domains were separated by 90° $a-c$ domain walls at 45° to the surface. The stripes were extended over the whole length of the sample and were ~10 μm wide on average. The setup for our experiment is schematically shown in Fig. 3.5(a). We used an x-ray Fresnel zone plate 250 μm in diameter with a 37 cm focal length at 7.5 keV to focus the synchrotron beam. The

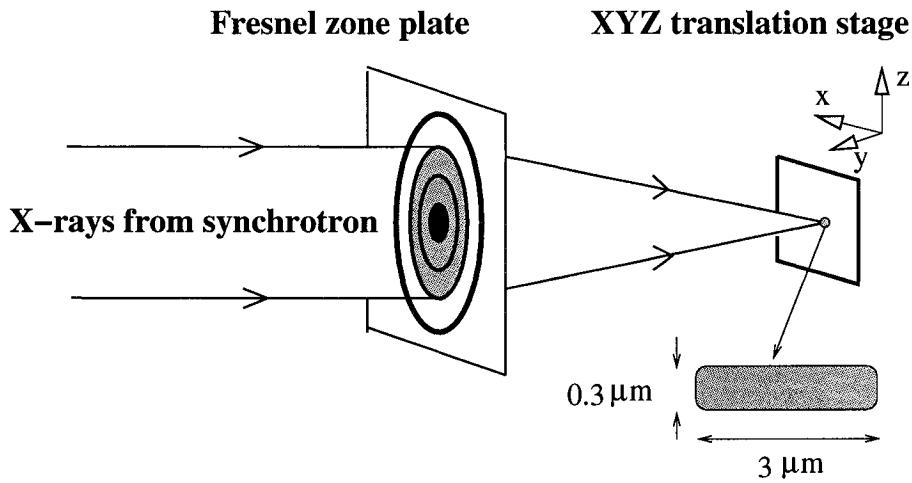

(a)

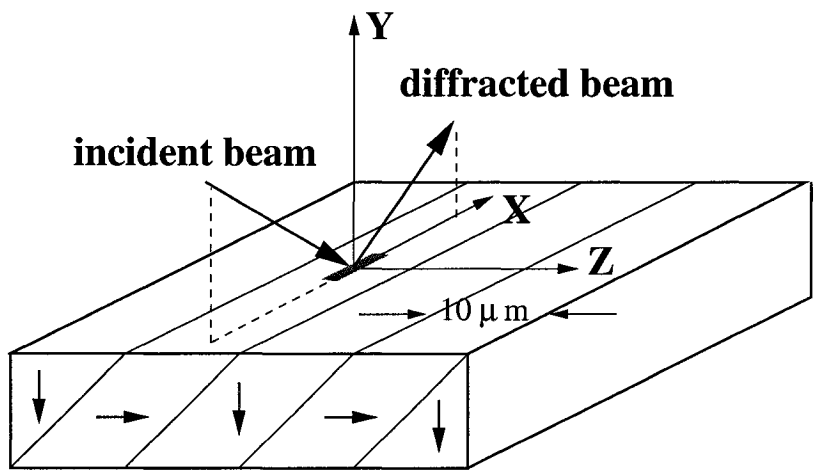

(b)

Figure 3.5: (a) Microfocusing setup. (b) Domains configuration in the $BaTiO_3$ sample and diffraction geometry.

focal area was as small as 0.3 μm in the direction perpendicular to the domain walls (diffraction limited in this dimension) and 3 μm parallel to the strips (Fig. 3.5(b)) with an efficiency of $\sim$30% of the illuminated flux. In x-ray scanning microscopy usually the sample is moved with respect to a fixed beam. In our case, we used a three dimensional XYZ translation stage with 30 nm step size over a 25 mm travel range. The stage was built by assembling together three translation stages (models 9064-X and 9064-Z) from NewFocus [144] company. Each stage was equipped with a picomotor actuator (model 8322) from the same company. These picomotors use a piezoelectric crystal to turn a fine-pitch screw. The models we used had $<$ 30 nm nominal step size over 25 mm travel range. In practice, to reproduce a movement with this resolution, one needs a readout system to register the absolute position of the stage and a feedback mechanism to control the motion of the actuators. To this end, we mounted a state-of-the-art optical encoder (Mercury 3000 from MicroE Systems [145]) on each stage. These encoders consist of two parts: a linear optical grating, and an optical encoder. The gratings had 20 μm wide parallel lines and were mounted on the body of the stages. An array detector, a diode laser, and electronic circuitry were integrated into the optical encoders which were mounted on the moving parts of the states. Figure 3.6 shows a picture of our assembled translation stage. The way these encoders work is as following: an interference pattern of the grating illuminated by the laser form on the detector array. When the stage moves with respect to the body, the array detector can sense the movement by measuring the displacement of the interference pattern. This pattern is digitally interpolated to allow measuring a fraction of an interference fringe. For example, we used 1024$\times$ interpolation factor which provided 20 nm linear resolution. The standard drivers and readout softwares supplied by the vendors did

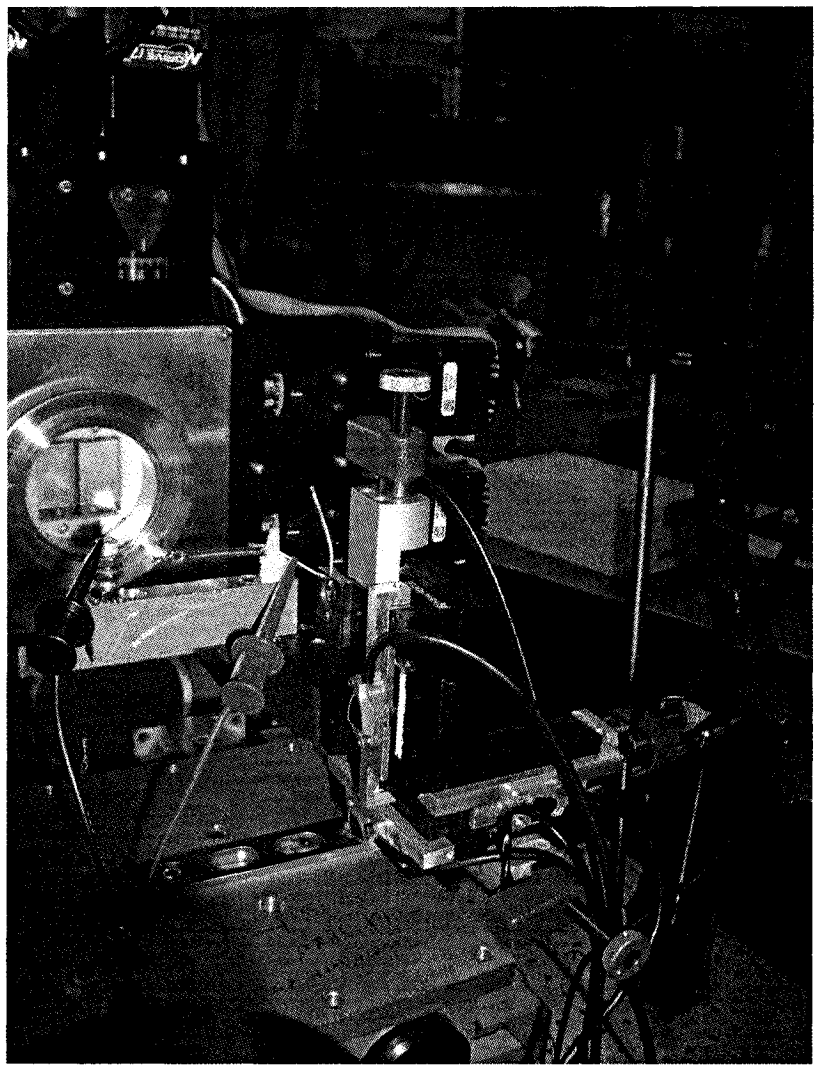

Figure 3.6: Picture of the XYZ translation stage

not meet our needs for an automated closed-circuit feedback mechanism. We had to rewrite most of them in Linux operating system and add new codes to embed them into SPEC [146], the program we use to operate our diffractometer. In our developed version, the encoders and picomotors are linked trough a feedback mechanism. The position is read by the encoders and, the picomotors are asked to correct the motion and position the stage at the required place. Our tests showed, both relative and absolute positioning of the XYZ stage with better than 50 nm resolution. The stage was mounted at the center of a three circle diffractometer. These angles are labeled θ (sample rotation), 2θ (detector angle), and χ (out-of-plane diffraction angle). To measure the x-rays we used a high resolution area detector consisting of a CCD camera on a microscope imaging an x-ray scintullator placed at ~30 cm from the sample. The combination of these gave us 1.5 μm spatial resolution. In our first run of experiments a 60×60 μm^2 area of the sample was scanned in 3 μm steps. At each point 2θ was set for (001) and (100) Bragg peaks corresponding to the c and a domains and θ scans were performed in 0.002° steps. A Lorentzian function was fit to the measured peaks at each point. Fig. 3.7(a) shows two dimensional maps of the integrated intensity of (100) peak. Fig. 3.7(b) represents the same quantity for (001) peak in the same scan area. On each image bright and dark stripes indicate strong and weak diffractions for one type of domains (for example, c domains). As can be seen, the bright stripes in one of the images line up with the dark stripes in the other one confirming the alternating $c-a$ 90° domains. The width of the domains were ~10 μm. Examples of the two Bragg peaks at the center of two adjacent domains along with the fit results are demonstrated in Fig. 3.7(c). Again, it is evident that the maxima of one type of domains corresponds to the minima of the other type and vice versa.

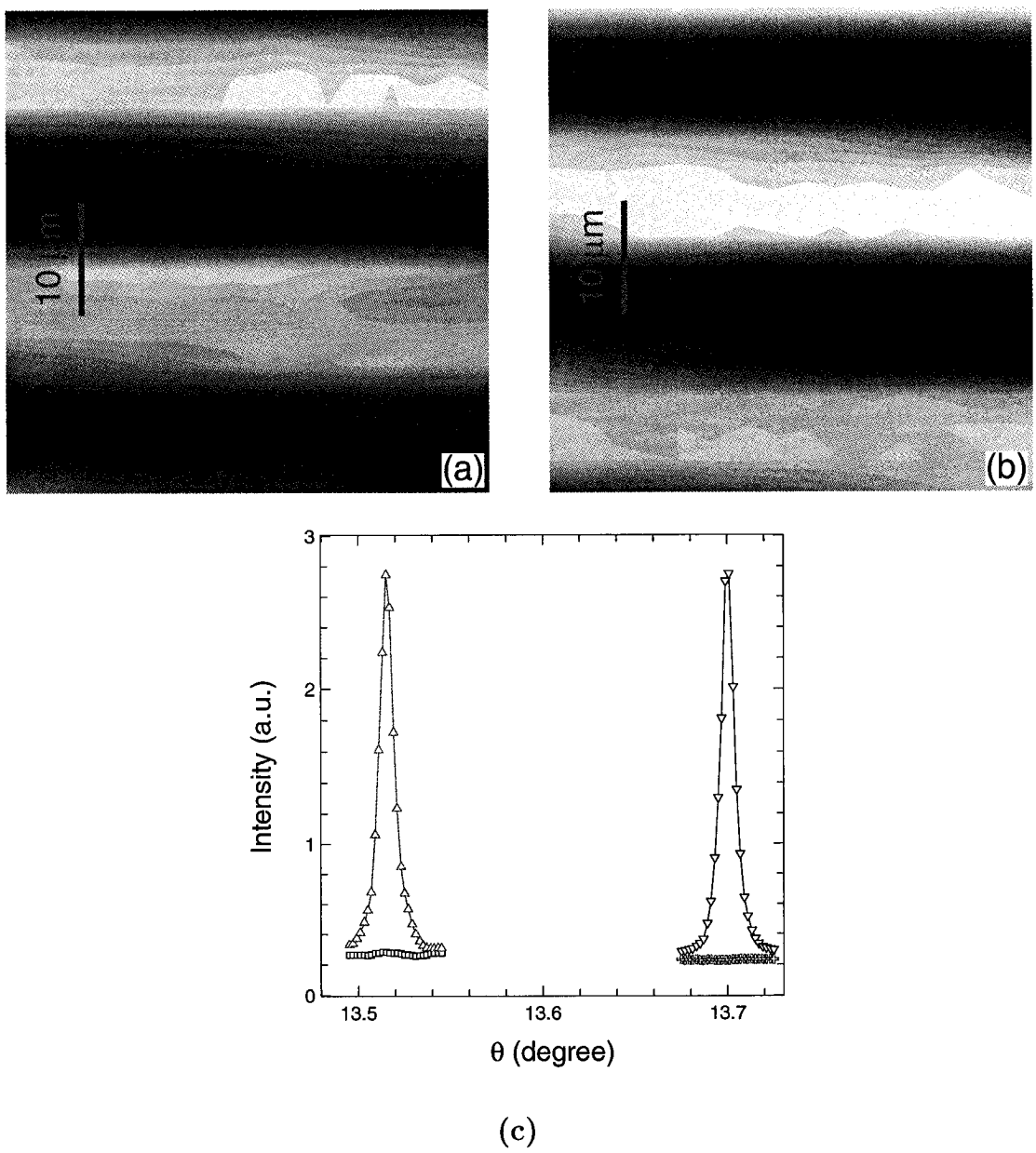

Figure 3.7: Alternating 90° domains in $BaTiO_3$. (a) maps of integrated intensity for (100) and (001) peaks in the same region. (c) Integrated intensity data (points) and fits (solid lines) at the center of a (100) domain (black) and a (001) domain (red).

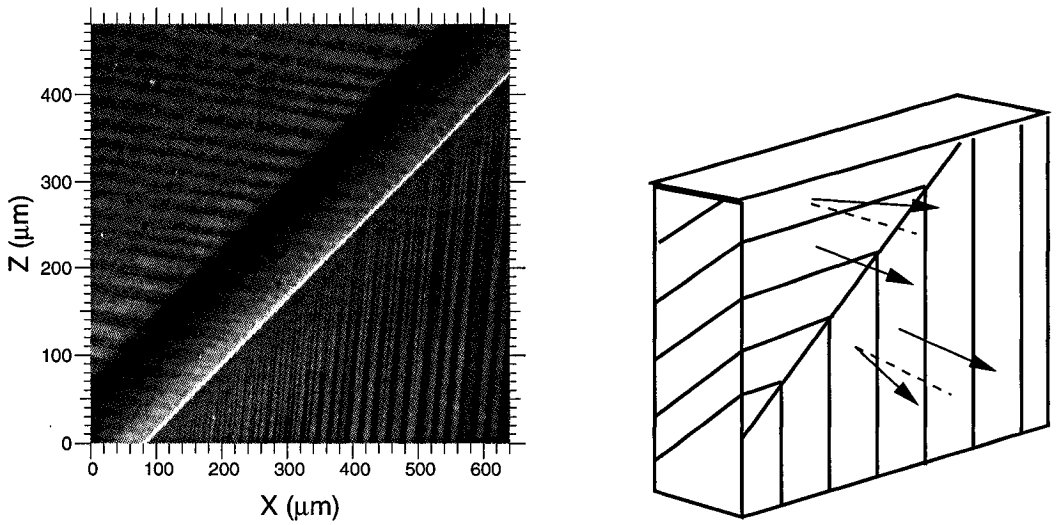

(a) (b)

Figure 3.8: Domains geometry in our $BaTiO_3$. sample: (a) Polarized microscope image of domains pattern across a diagonal $a - c$ wall. (b) (001) and (100) Bragg peaks associated with the four domains.

One of our $BaTiO_3$ samples had a big diagonal $c - a$ wall at 45 ° to the crystal edges. Bragg peaks pattern is more complicated for this sample because there are (001) and (100) peaks on each side of this wall leading to a total of four distinct Bragg peaks. Fig. 3.8(a) shows a polarized microscope image of the domains near this wall. The orientations of the four peaks with respect to each other are illustrated in Fig. 3.8(b).

In our primary measurements at McGill we used our high resolution diffractometer in our lab to characterize the structure of this sample. We used Cu k_α ($\lambda = 1.540$ Å) and a scintillation detector in our experiments. Since the beam was much larger than the domains width, we were able to measure both a and c domains by proper settings of the detector and sample. Two Bragg peaks were identified to uniquely define the reciprocal lattice and then a two dimensional mesh scan in 5×10^{-4} $Å^{-1}$ steps in the

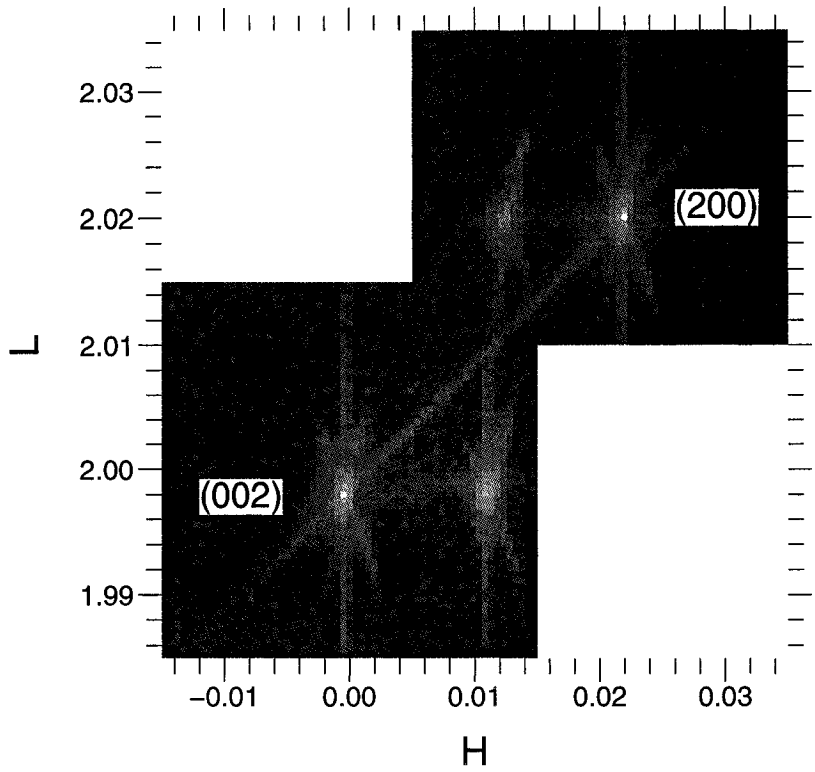

Figure 3.9: Reciprocal space map of the (002) and (200) peaks for the two sections of the $BaTiO_3$ sample. The two brighter peaks on the diagonal line correspond to one section.

reciprocal lattice coordinates was performed to obtain a direct map of the reciprocal space. The result of the scan is shown in Fig. 3.9. Table 3.4 summarizes the results of fitting a Gaussian function to the peak shapes in the reciprocal coordinates for both of the (002) and (200) peaks belonging to one of the sections (the labeled ones) of the sample. Since these are second order diffractions of (001) and (100) peaks, the lattice constants can be calculated using the Bragg's law:

$$d = 2 \times \frac{\lambda}{2\sin(\frac{2\theta}{2})}. \tag{3.13}$$

Peak	2θ (degree)	H	L	H_{FWHM}	L_{FWHM}
(002)	44.8610	-4.4×10^{-4}	1.9980	2.4×10^{-4}	3.5×10^{-4}
(200)	45.3864	2.185×10^{-2}	2.0201	1.9×10^{-4}	3.7×10^{-4}

Table 3.4: $BaTiO_3$ (002) and (200) reciprocal space coordinates.

For a tetragonal lattice the diffraction vector q is given by:

$$q = 2\pi[(\frac{H}{a}) + (\frac{L}{c})]. \tag{3.14}$$

H and L are Miller indices. The uncertainty in q is therefore:

$$\frac{\delta q}{q} = [(\frac{H}{a})^2 + (\frac{L}{c})^2]^{-1}\,[(\frac{H}{a})\delta H + (\frac{L}{c})\delta L]. \tag{3.15}$$

Estimating the errors in peak positions to be ~20% of the FWHM, we calculated $\frac{\delta q}{q}$ for (002) and (200) peaks from eq. 3.15. Relative uncertainty in lattice constant is equal to:

$$\frac{\delta d}{d} = \frac{\delta q}{q}. \tag{3.16}$$

From these calculations we found: $c = 4.0360 \pm 0.0006$ Å, $a = 3.9917 \pm 0.0006$ Å. The angle of the 90 domain walls then can be calculated from eq. 3.12: $\alpha = 44.684 \pm 0.008°$. The deviation of the angle between polarization axes of the two neighboring domains from 90° is then equal to: $90 - 2\alpha = 0.632 \pm 0.016$. We can also find the same angle by calculating the angle between $\mathbf{q}_{002}$ and $\mathbf{q}_{200}$ using the coordinates in table 3.4. This gives us 0.6445° which agrees with the previous value within the

calculated uncertainty.

In our second series of measurements, we used the same setup as in Fig. 3.5(b), but did a one-dimensional ~40 μm scan of the sample in z direction (perpendicular to the domains) in 0.5 μm steps. This range was enough to cover approximately 4 domain widths. At each position, a $\theta - 2\theta$ scan in 0.001° steps, a 2θ scan in 0.001° steps, and a χ scan in 0.04° steps were measured for the (002) Bragg peak (c domains). The measurements were repeated for the (200) peak (a domains). Integrated intensity for the (002) and (200) reflections are plotted in Fig. 3.10. The alternating ~10 μm wide patterns of c and a domains are clearly seen in these measurements. The width of the domains agree with our first measurement, but show better resolution. The 45° domain walls implies that diffraction must be visible from both c and a domains within an area of the size of the absorption length of the x-rays. The x-ray wavelength used in these measurements was 1.674 Å by comparing the peak positions measured here with those obtained in our high resolution measurements using Cu kα_1 radiation. For this wavelength, the absorption length of $BaTiO_3$ is ~5.41 μm which agrees with the width of the inter-domain regions where two domains overlap.

To obtain more quantitative information about the domains structure, a simple diffraction model (Fig. 3.11) was developed. This model was based on the fact that the integrated intensity for each domain is proportional to only the material in that domain, but both domains contribute to absorption (see Appendix A for details). First an alternating geometry of c and a domains separated by 45° domain walls at certain positions were defined. Then, the diffraction intensity from a small volume under the crystal surface was calculated considering the total absorption of the material above. The total integrated intensity for each type of domains was obtained by

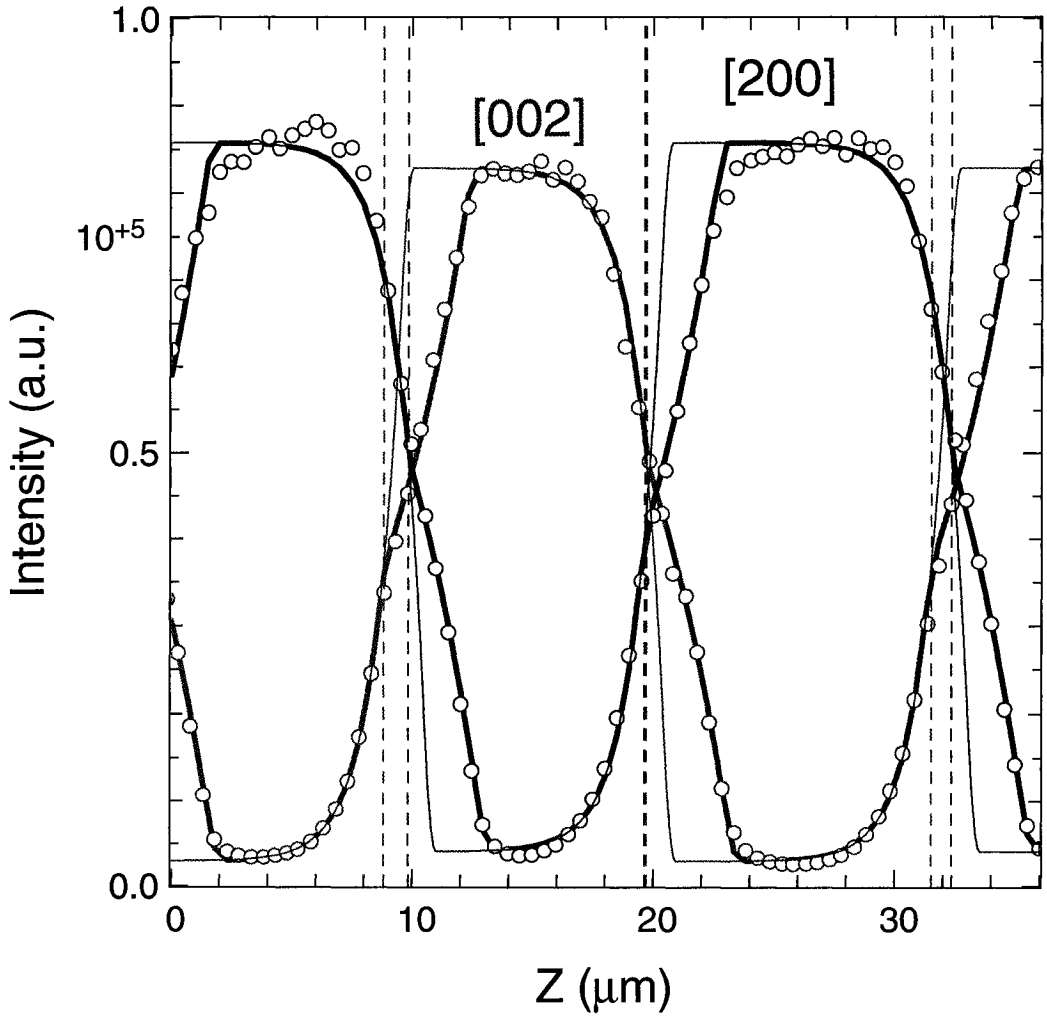

Figure 3.10: Integrated intensity for (002) and (200) domains along the z axis (perpendicular to the domains strips). The thin solid lines show the results of fit to straight 45° wall model. The thicker solid lines are fits to the modified broken-line wall profile. Dashed lines indicate the places in this model where the orientation of the walls changes from bulk-like to surface-like region. These positions line up with the positions of the "kinks" in the data.

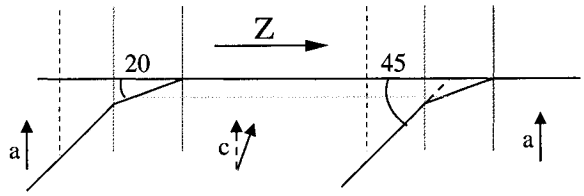

Figure 3.11: Model to explain the integrated intensity from alternating $c-a$ domains. Both the straight-line and the modified broken-line wall profiles are shown.

integrating over the thickness of that domain at the specified point. Repeating this calculation for several points across the domain pattern provided the integrated intensities as a function of position for both domains. One can, then, vary the positions of the domain walls to fit the obtained integrated intensity to the experimental data. The result of the fit is shown as thin solid lines in Fig. 3.10. It is immediately evident that this simple straight-wall model cannot adequately explain our data. There are some "kinks" where data points start to deviate from this model. We extended our model by assuming a double-slope profile for the domain walls as shown in Fig. 3.11 and let the slopes of the wall vary in our fit. This considerably improved the results of our fit as the thick solid lines show in Fig. 3.10. Our investigations, for the first time, revealed that there is a $\sim$1 μm surface-like layer near the crystal surface where the domain walls orientation changes from 45° to $\sim$20°. This modified structure is probably adopted by the domain walls to minimize the deformation energy near the crystal surface. The effect of the crystal surface, as described in our work, on the structure of domains near the surface has not been adequately considered by others who tried to model or measure the domain wall profiles [41, 102, 112]. The two angles of the domain walls and the transition point from bulk-like to surface-like orientations were obtained from fitting the model to our data. The transition points are also plotted

by dashed lines in Fig. 3.10. It can be seen that these points line up nicely with the kinks observed in the data. Furthermore, from the fit results we can unambiguously determine the intersections of the walls with the crystal surface.

To discover more about the fine structure of the domains, we fit a modified Gaussian function with a flat area to the θ, $\theta - 2\theta$, and χ scans at each step of our z scans. Fig. 3.12 summarizes the fit results for the (002) domains. Relative strain $\Delta c/c$ was calculated from the peak values of 2θ scans. Peak parameters in the middle of the central domain was used as reference to calculate strain and all other angle changes. We can use the results of our model for the domain walls to draw the positions of the intersections of the walls with the crystal surface (red dash-dot lines), the kinks (green dashed lines), and one absorption length below the crystal surface (blue dot lines) on all the windows. In this figure diffraction is associated to the central domain in Fig. 3.12(a). Near the crystal surface this domain is thicker on the left side (135° edge) and thinner on the right side (45° edge). Strain is tensile on the left side and has its maximum value in the surface-like area. It is almost constant in the middle of the domain and becomes compressive with a larger absolute value on the right side. This is best understood if we consider this domain as a crystallite "clamped" between the two neighboring (200) domains [102]. The (002) domain is thick on the left side near the surface where its (200) neighbor is thin and, therefore, gets less distorted by this neighbor. On the contrary, the (002) domain is thin on the right side where its (200) neighbor is thick, making the distortion by its neighbor more profound. In both cases lattice distortion is more obvious in the surface-like area. Finite size effect due to asymmetric thicknesses and the extreme strains at the two sides of the (002) domain are manifested in the peak width as shown in Fig. 3.12(d).

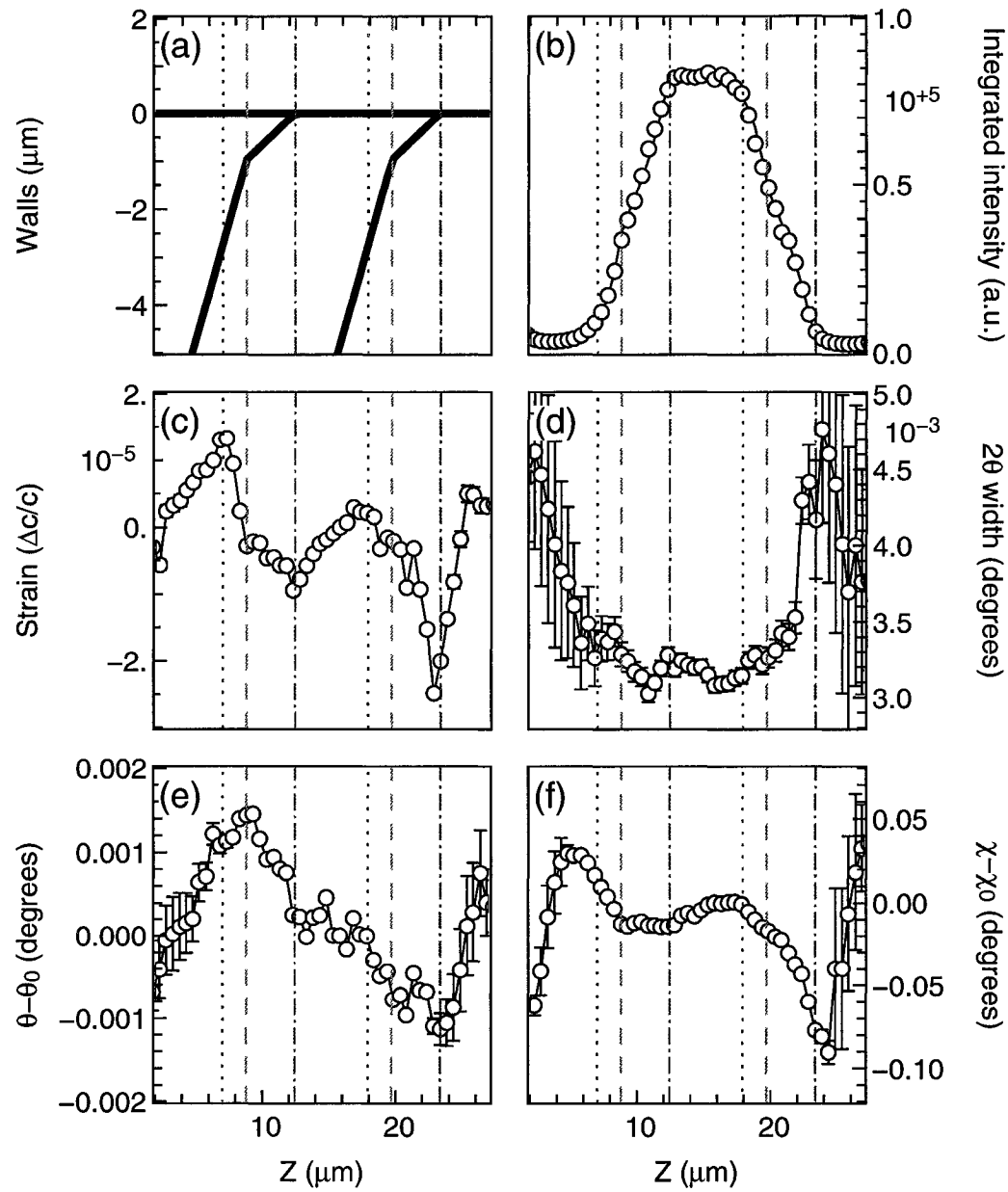

Figure 3.12: Summary of the model and scan fit results for (002) domains: (a) Domain walls profile. (b) Integrated intensity. (c) Relative out-of-plane strain peaking in the surface-like area. (d) 2θ width shows finite size and lattice distortion effects. (e) crystal angle rotation. (f) χ angle rotation. The asymmetric behavior due to varying domain thickness near the surface is observed in all the graphs. Intersections of the domain walls with crystal surface (red dash-dot lines), the kink positions (green dashed lines) and one absorption length under the crystal surface (blue dot lines) show how the variations in the plots register with the characteristic points of the model.

This asymmetric behavior is observed in other peak parameters as well. also observed the same asymmetric behavior in the strain profile, but, The (002) domain axis undergoes asymmetric rotations in both θ and χ angles. Again the effects are in opposite directions and enhanced in the surface-like area under the crystal surface. Each domain observed as a crystallite doesn't line up completely with the crystal axes. The maximum and minimum of the c axis rotation in θ are associated with the kinks positions where the domain wall orientation changes.

From these observations we can argue that the departure of the domain wall shape from simple 45° wall and also the asymmetric thicknesses of the domains near the surface are responsible for the complicated behavior of the domains characteristics. We should also consider the long range domain-domain interaction a factor in domains morphology. The elastic fields around the domain walls extend several microns around the walls although the walls themselves are much thinner.

Similar asymmetric pattern in the strain was observed by Rogan et al. [112], but the reason for that was unknown to them. They used white beam Laue microdiffraction on a similar $BaTiO_3$ crystal with 40μm wide domains instead of 10μm and found normal strain about two order of magnitudes bigger than our measurements. The reason might be that in their measurements the x-ray data was averaged over 70 μm depth of the crystal and their experiment had about 10 times less spatial scan resolution. Our model and results help to understand the source of the asymmetry in all these quantities.

3.4 X-ray diffraction imaging of $BaTiO_3$ domains

To complete our study and compare the two microdiffraction methods, we also did an XDI study of ferroelectric domains in $BaTiO_3$. We used a parallel beam diffraction geometry and a CCD camera with 0.645 μm resolution in both x and z directions. With this technique we were able to record x-ray diffraction data of a 500×500 μm^2 area in a single scan (see sec. 2.3.2). The detector was set for the (200) reflection and the rocking curve of the sample was measured in 0.002° steps. Figs. 3.13 (a)-(f) exhibit snapshots of the recorded images in 0.01° intervals. The strip-shape domain patterns are clearly visible in these images. Also, it can be seen that different areas on the sample are slightly tilted with respect to each other so that each area appears bright at a different angle as the sample rocks. Even more interesting is the short range non-uniformity of intensities within each domain. Fig. 3.13 (g) is the rocking curve obtained by averaging over the entire sample area. The positions of the snapshots are labeled on this graph. As mentioned before, x-ray microbeam scanning has the advantage that it provides structural information from a specific micron-size region on the sample. Since the focused beam is intense, once it is pointed to the desired area on the sample, diffraction signal to noise ratio is normally good and data acquisition can be done quickly. It is, however, a scanning technique and, like others, we need to first find the region of interest on the sample. In all scanning probe microscopy techniques this is usually achieved by doing a coarse point-by-point scan of a big area to get a rough image and then move the probe to the desired area for a higher resolution scan. X-ray topography, on the other hand, has the advantage that we can take an image of the whole sample at once with high enough resolution. The diffraction signal is not as strong as with a microfocused beam, but, this is not a big

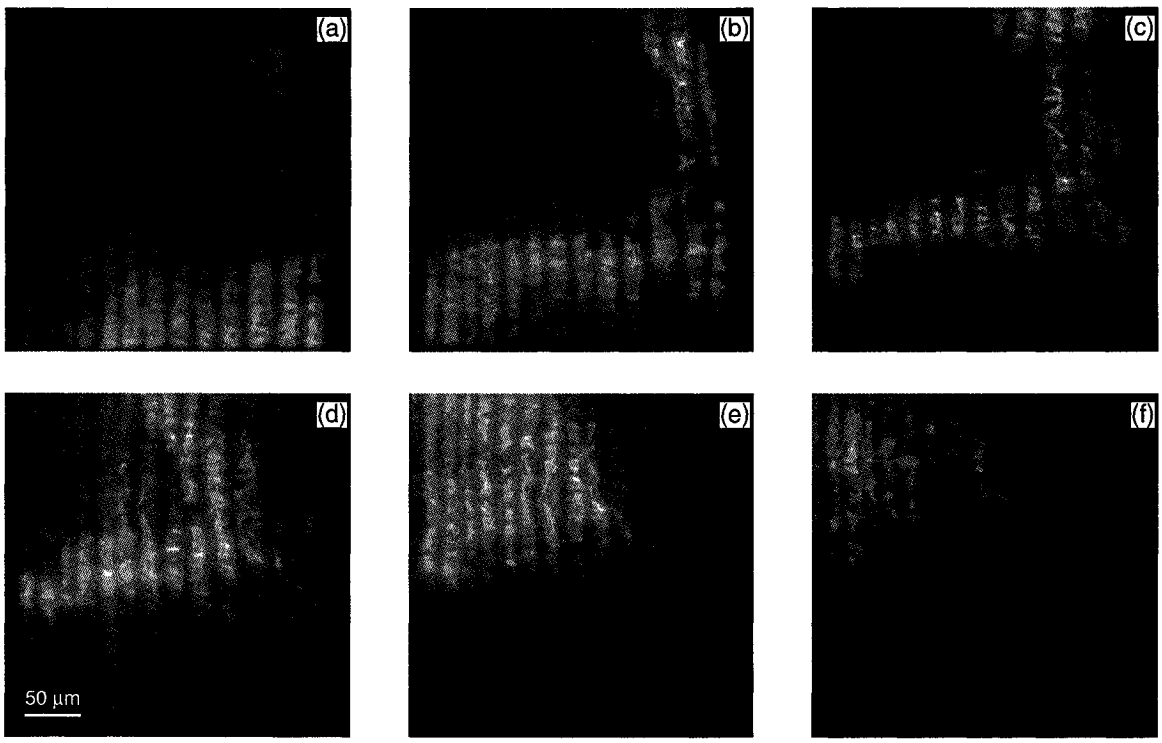

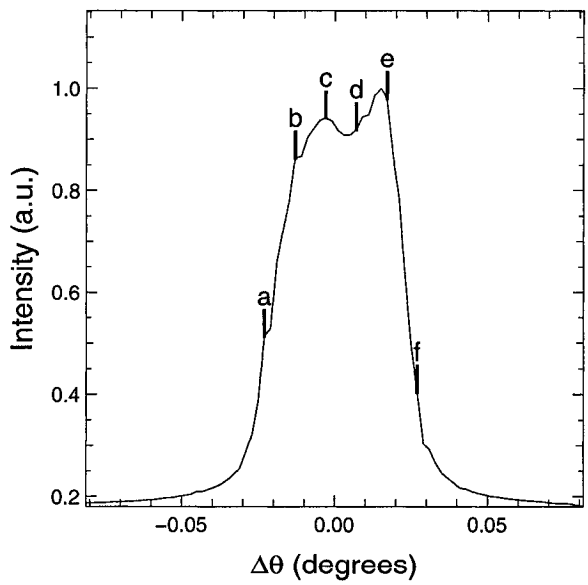

(g)

Figure 3.13: (a)-(f) Topography snapshots of (200) domains in $BaTiO_3$ in 0.01°intervals. (g) Positions of the snapshots on the rocking curve of the whole sample area. Scan step was 0.002°.

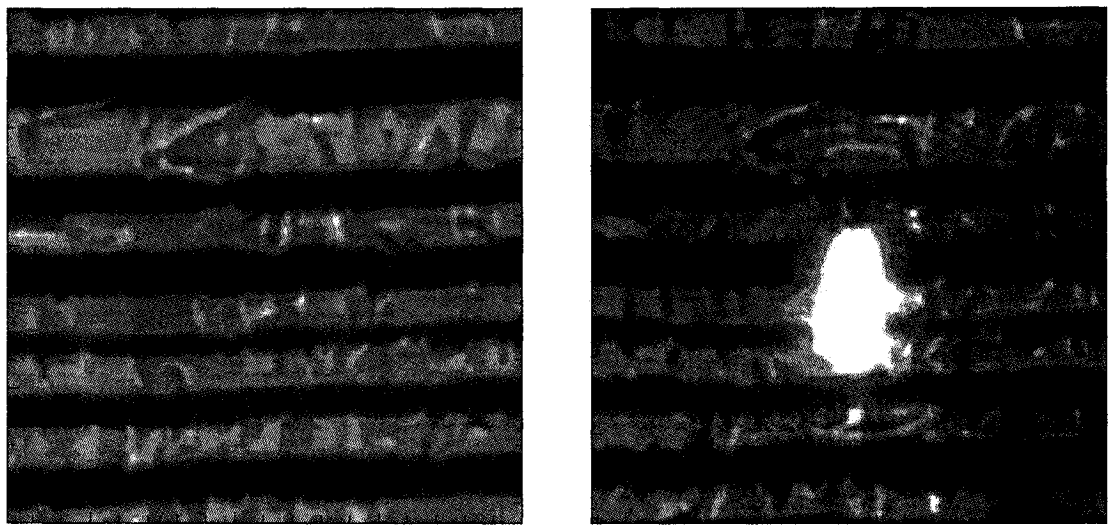

(a) (b)

Figure 3.14: Topographic images (a) before, and (b) after inserting the Fresnel zone plate. The combination of the two techniques helps to quickly register the microfocused beam on the sample and later move the beam to the desired position.

issue with high flux synchrotron sources.

We decided to combine these two methods to take advantage of both. Fig. 3.14 (a) shows a topography image of the domains pattern taken with a wide beam (XDI mode). We then inserted the Fresnel zone plate into the beam at a focal length from the sample to switch to microfocusing mode. A Fresnel zone plate focuses only part of the incident beam (30% in our case) and the rest of the beam passes through directly. Normally the direct beam is stopped by using an *Order Sorting Aperture* (OSA) after the zone plate. This is, basically, a diaphragm to allow only the focused beam pass trough. Without an OSA, both the direct and focused beam will shine on the sample and the result will be similar to what is seen in Fig. 3.14 (b). Comparing the two images helps us to register the coordinates of any point on the sample to the position of the focused beam. Having done this, we can easily move the sample to bring the

desired point (for example, a domain wall) to the focal point. Now we can switch back to microfocusing mode by inserting the OSA again and begin to do our diffraction experiment by the microfocused beam. This eliminates the need for a point-by-point scan and saves considerable amount of time and effort.

Chapter 4

X-ray diffraction imaging of a silicon microcantilever

Micromachining is the method to make micron-size devices such as microsensors and transducers from bigger bulk materials or produce microstructures on bigger pieces. A good example is fabrication of cantilevers used in different scanning probe microscopy techniques from bulk single crystals [135]. Usually micromachining involves processes like etching, doping, annealing, and oxidation which may introduce residual strain and/or dislocations into the final product [60]. For instance, a common method used to control the etch depth in fabrication of silicon devices is to dope high concentration of boron ions to the desired depth of the material. Boron ions are resistant to the etchant (KOH, for example) terminating the etching process at the desired depth. Etch stops like boron, being a different kind of atoms forced into the sample lattice, introduce residual strain and dislocations to the original material [104]. Although the crystal is usually annealed to relieve the residual strain, some effects persist. A quantitative understanding of the imperfections introduced by the manufacturing process can help to improve this process or at least characterize these effects in the final products. In addition to the imperfections caused by the fabrication process,

small distortions can develop in these devices as a result of thermal variations or mechanical deformations applied to them. These can be unwanted effects or what exactly the device is designed to measure. For example, a microcantilever may be designed to measure small forces, torques, surface strains, or thermal variations. In any case, If we want to understand the behavior of the device, a quantitative method is needed to measure these effects [108]. Applications are quite wide and include: semiconductor industry [65], Scanning Probe Microscopy (SPM) [114, 113], microsensors [131], and optical devices [61, 54]. Measuring lattice reorientation and strain in micromachined single crystal cantilevers used as sensors in different types of SPM instruments, is important both for manufacturers and users of these devices [113, 114, 131, 42, 126]. Different techniques are available to study the quality of small crystals. Wolf [33] and Srikar [126] used Raman spectroscopy to measure bending stresses in micromachined silicon devices. High resolution x-ray diffractometery is another standard technique for this purpose. For instance, Cargill [18] used this technique to study lattice compression in doped Si:As crystals. Noyan et al. [105] has reviews how this technique is used to measure the residual stresses in thin film structures. Murray et al. [100] also used x-ray diffraction to study the heterogeneous distribution of stress in thin film/substrate composites.

X-ray diffraction imaging (also called x-ray topography, see sec. 2.3.2) is a powerful non-destructive technique which can provide detailed information about local imperfections in nearly perfect crystals. There are many old [103] and newer [13, 6, 16, 45] references to learn the fundamental principles of this powerful technique. The main advantages of this technique, as described in sec. 2.3.2, is that it can provide diffraction data from the whole illuminated area on the sample in short time. Also, de-

pending on the experiment setup, it has very good sensitivity to lattice distortions. Newkirk [103, pages 431–457] used this method to study dislocations in silicon crystals. Kimura and Ishikawa [79, 78] used plane wave x-ray topography to measure the strain field in silicon crystals. Ludwig [89], Dudley [39], and Lida [85] studied defects structure in high quality crystals using XDI. Murray et al. [101] used x-ray topography to measure strain fields near SiGe etched lines of various widths and Ni dots on silicon substrates. Noyan et al. [106] used synchrotron x-ray topography with a microfocused beam to characterize the interface between a polycrystalline Al thin film on single crystal silicon substrates. One of the remaining difficulties is, however, to properly identify, resolve, and distinguish between lattice rotation and lattice strain in small crystals comparable in size with the spatial resolution of the topography images (a few μm). There has been work to measure strain and lattice curvature in big crystals under large loads. Yang et al. [140] measured Poisson ratio and anticlastic curvature in silicon crystals with large deflections. Kaldor et al. [71] studied the effect of smaller loads. However, the important problem of lattice distortion in slightly distorted micron-size crystals deserves more detailed and quantitative studies.

We used high resolution (both angular and spatial) plane wave XDI technique (sec. 2.3.4.5) to measure complete two-dimensional maps of lattice reorientation, twist, and out-of-plane strain field in a micron-size single crystal silicon cantilever. These cantilevers were fabricated by micromachining methods to be used in scanning probe microscopes. Apart from practical applications that these cantilevers have, for us they were perfect samples to test our XDI setup. We studied lattice distortions in the free standing state of the cantilever where no force is applied. Then we applied a small force to the cantilever to bend it by $\sim 7 \times 10^{-4}$ rad and measured the same quantities

for the bent cantilever. Our results show $\sim$ 8 mdeg lattice twist between the cantilever and its much thicker supporting base. Anticlastic curvature and out-of-plane strain both follow a nearly parabolic profile across the cantilever width. We found that the cantilever gets curved across when it is bent with a minimum $\sim$0.3 m radius of anticlastic curvature in the middle of the cantilever width. We also measured the relative strain map of the cantilever. Our calculation showed increasing strain toward the fixed end of the cantilever. The average strain reaches a maximum of 2×10^{-5} at the edges of the cantilever. We discovered an area as big as the cantilever width near the junction with the base where these quantities are highly non-uniform probably because of the abrupt change in the crystal thickness and the etching process.

In this chapter we will first describe the details of the setup we used and the experiments we did. Because of the complex nature of the data, a great amount of data analysis and modeling were required to extract useful information and compare them with the theory. The most important procedures and steps in analyzing our data will be presented. Next, we will show the results we obtained and discuss them in the context of the existing theories for deformation of crystals.

4.1 The x-ray diffraction imaging experiment

The experiments were carried out at the 8-ID-E side section of IMM/XOR-CAT (IBM, MIT, McGill X-ray Operation and Research Collaborative Access Team) at the Advanced Photon Source, Argonne National Laboratory. Our samples were single crystal silicon sensors made by NANOSENSORS Company [147]. Each sensor had a bulky holder and a much smaller cantilever with an integrated tip. The whole sensors were etched from a highly doped (to increase conductivity) silicon single crystal. These

sensors were made of same material and, in theory, had the same lattice everywhere. This helps to minimize the inherent strain and also thermal deformations if the ambient temperature changes. Also, the monolithic structure of the sensors provides an "absolutely straight" cantilevers as the company claims. The cantilever part was about 450 μm long, 52 μm wide, and 1.7 μm thick with a trapezoid cross section. The base part was about 315 μm thick. Fig. 4.1 shows a technical drawing of the entire sensor, an optical microscope image of the cantilever, and a non-scaled drawing of its cross section. Crystallographic orientations of the sample are also shown: the cantilever surface is perpendicular to the $\langle 001 \rangle$ direction. Fig. 4.2(a) shows a schematic drawing of the experiment setup. The size of the source was 50 μm in horizontal and 350 μm in vertical. 7.5 keV ($\lambda = 1.653$ Å) x-rays from the source shined on a (022)-cut silicon monochromator located at 55 m from the source. The divergence of the incident beam was negligible for the purpose of our experiments. After diffracting off the monochromator, the wavelength spread of the beam is determined by the Darwin width of the silicon (022) reflection which is $\sim 6 \times 10^{-5}$ Å. Since the sample is almost a perfect crystal, we need to consider dynamical theory of x-ray diffraction (sec. 2.2) to understand the experiment. We measured the (004) Bragg peak of the sample. For this reflection the extinction length of the x-rays is ~ 27.5 μm which is an order of magnitude bigger than the cantilever thickness. Therefore, finite thickness of the cantilever plays an important role in increasing the divergence of the diffracted beam. As discussed in sec. 2.3.3, an analyzer after the sample and before the detector can help to remove the ambiguity between lattice reorientation and strain effects on the diffraction angle. We used a channel-cut analyzer [75] consisting of two parallel silicon (111) surfaces. The analyzer at each position selects only those diffracted rays

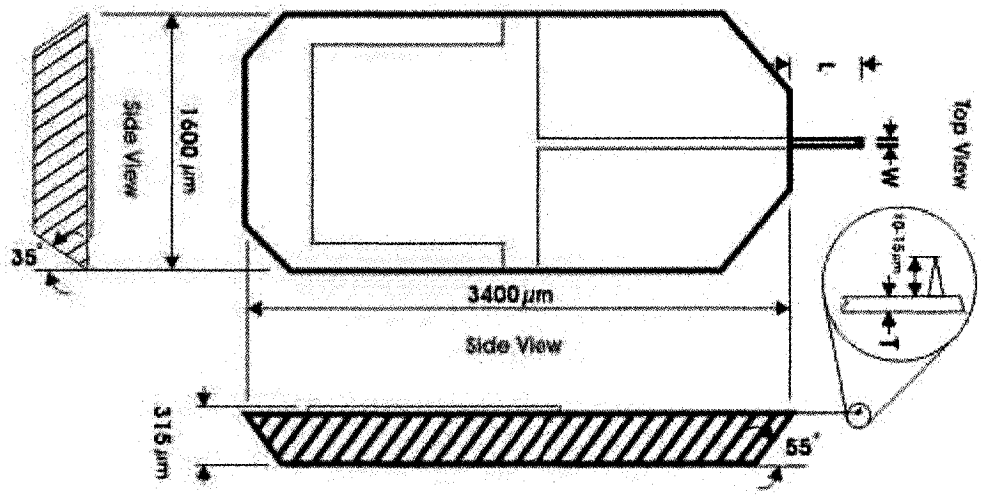

(a)

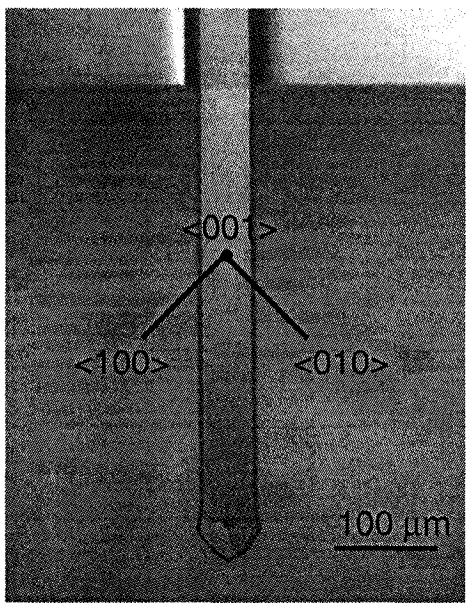

(b)

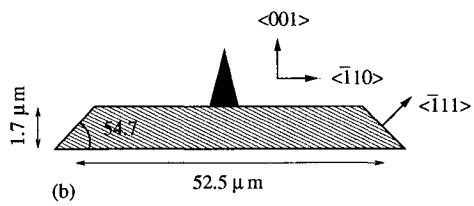

(c)

Figure 4.1: Cantilever geometry: (a) technical drawing. (b) Optical microscope image with 20× magnification. (c) Cantilever cross section (not-scaled).

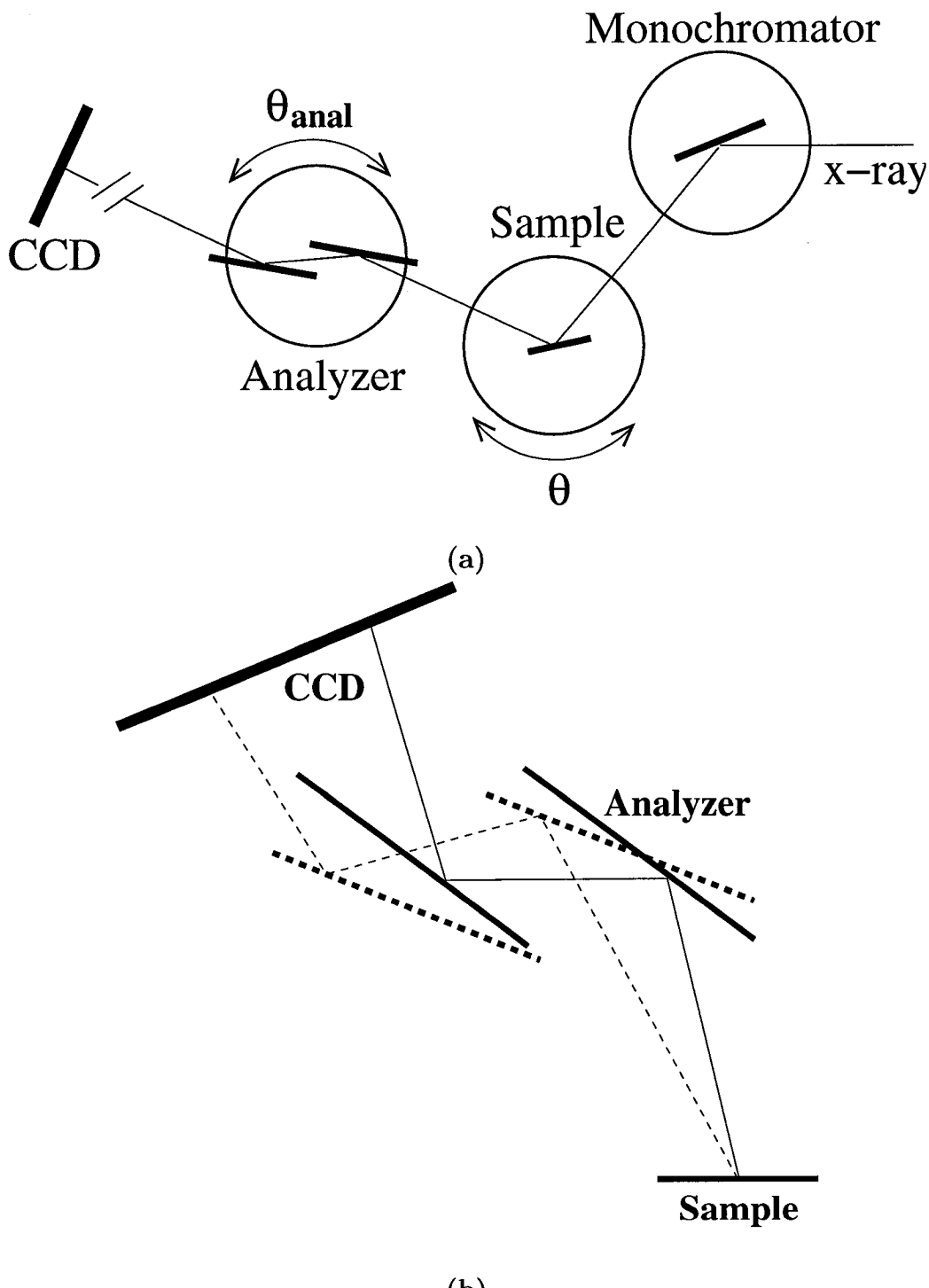

Figure 4.2: X-ray diffraction imaging setup for the silicon cantilever: (a) Schematic of the experiment setup. A mesh scan of sample angle (θ) and channel-cut analyzer (θ_{anal}) provides a 4D [θ-2θ at each (x,y) point of the sample] stack of diffraction images. (b) Each θ_{anal} position picks only a set of parallel diffracted rays which then have to be restacked for the lateral shift on the CCD.

from the sample that satisfy the Bragg condition for Si(111). Sample and analyzer angles are denoted by θ and θ_{anal}, respectively. After setting the diffractometer for silicon (004) peak, we scanned θ in 0.625 mdeg steps in a $\pm 0.01^{\circ}$ interval and at each step performed a similar scan of θ_{anal} in 0.5 mdeg steps. For each value of θ and θ_{anal} in this mesh scan the diffracted x-rays were recorded by a CCD camera. The camera was equipped with an optical microscope and located $\sim$20 cm from the sample. The CCD had 0.645 μm square pixels. Several such mesh scans were recorded. To measure the effects of bending on the cantilever, an electric field was applied to the cantilever by applying a voltage between the cantilever and a metallic electrode placed behind the cantilever and very close to its tip. Since the sample was doped, the electric field can apply a localized force to the cantilever. We noticed an interesting phenomenon when applying electric field to the cantilever: it takes seconds for the cantilever to deform when the voltage is turned on, or relax to the original shape after the voltage is disconnected. We believe this is because of the ionizing effects of the incident x-rays. X-rays generate extra charges in the cantilever which disturb the applied electric field. When the electric field is established or disconnected, the ionization charges have to re-arrange by creating ionization currents. Reaching to the final equilibrium state with these currents is probably a slow process during which the electric field keeps varying.

4.2 Results and discussion

4.2.1 Restacking the CCD images

The first step in analyzing the data was to re-arrange the recorded images. As mentioned in the previous section, for each θ_{anal} the analyzer uniquely defines the diffraction angle 2θ. However, as can be seen in fig. 4.2(b), the analyzer rotation translates the image on the CCD. The recorded data are 4-dimensional arrays of intensities: at each (x,y) point on the detector intensity is recorded for a mesh of θ and 2θ values. We like to use the notation $\mathrm{I}(x, y, 2\theta, \theta)$ for the data to emphasize on this fact. For a fixed position of the sample (θ=const.), this forms a stack of CCD images in which each frame is translated with respect to the previous one by a small value as a result of 2θ scan. The diffracted ray from a given point on the sample, therefore, gets recorded at different pixels of the CCD. We, consequently, had to reconstruct the stack of images by moving each frame back by the amount it was shifted with respect to the first frame. This ensures us that there is a one-to-one correspondence between the points on the detector and those on the sample. At each given (x_0, y_0) point on the sample $\mathrm{I}(x_0, y_0, 2\theta, \theta)$ can then be treated as two-dimensional map of 2θ-θ scan intensity. We called the reconstruction process *restacking*. The per-frame shift is equal to $x_{off} = L \times \delta(\theta_{anal})$, where L is the detector-sample distance and $\delta(\theta_{anal})$ is the analyzer scan step. In our setup $x_{off} = 1.75$ μm which was equivalent to 2.7 pixels. In the restacking process each frame in an analyzer scan was digitally shifted back by the integer part of the total shift for that frame. Then, a new frame was reconstructed by interpolating the shifted frame and the preceding frame using the fractional part of the shift value as interpolation factor. To test the restacking

code, a test image was shifted by a known value to build a stack of images. The restacked images then were compared with the original image. The results confirmed that the restacking process was correct. This process was then applied to the raw data to obtain restacked images of the cantilever.

4.2.2 Thickness variations, resolution

For silicon (004) reflection both the absorption length (57.8 μm) and the extinction length (27.5 μm) were an order of magnitude bigger than the thickness of the cantilever (1.7 μm). The base, on the other hand, was 315 μm thick which is an order of magnitude bigger than the extinction length of the x-rays. For the base, the incident x-rays will get diffracted within the extinction length no matter what the actual thickness of the base be. The cantilever was not, however, thick enough to diffract all the incident x-rays and most of them passed through. Therefore, the integrated intensity is proportional to the thickness of the cantilever at each point. From these arguments we expect a much higher integrated intensity for the base compared to the cantilever. Fig. 4.3(a) shows a 2D plot of the integrated intensity of the cantilever and its base averaged over 2θ and θ angles. The brighter base is clearly distinguishable from the less bright cantilever. Small variations of the thickness of the cantilever causes intensity variations in Fig. 4.3(b). For example the tip appears substantially brighter because there is more material there. Of course, it is possible that the intensity of the incident beam itself is not uniform all over the cantilever. This can be easily verified by moving the whole sample with respect to the beam and comparing the two images. If the intensity pattern changes, it means that the non-uniformity comes form the beam, otherwise, it is due to variations in the cantilever thickness.

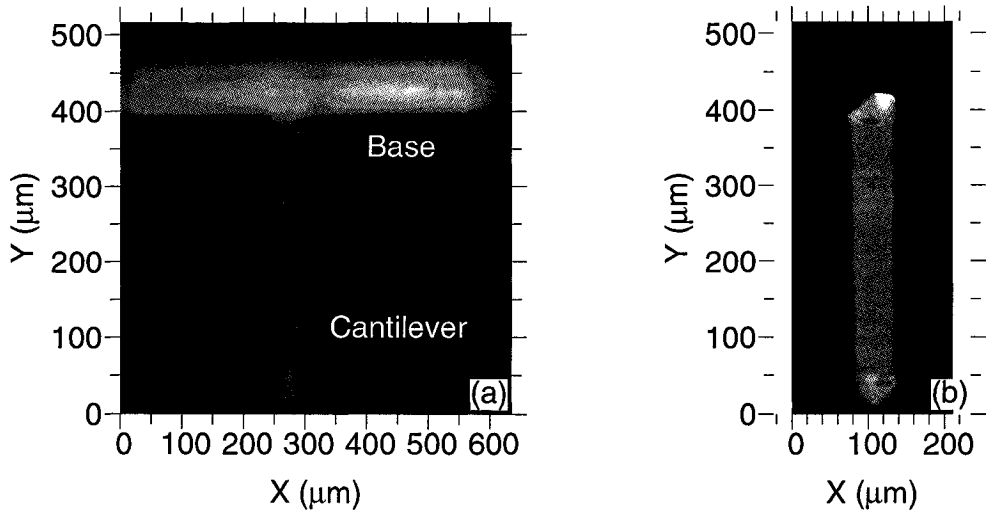

Figure 4.3: 2D plots of integrated intensity averaged over 2θ and θ: (a) The base appears brighter, because it is much thicker. (b) Intensity variations reveal small thickness non-uniformities over the cantilever area.

In the setup we used, the cantilever surface was in symmetric Bragg diffraction geometry. This means that regardless of the x-ray wavelength, the incident and exit angles with the crystal surface are always equal (see sec. 2.2.3). However, because of the trapezoid cross section of the cantilever, the two wedge-shape surfaces on the sides of the cantilever are in asymmetric Laue diffraction geometry (see Fig. 4.4). This implies that even if the incident rays are parallel, the exit angle will be different for different wavelengths within the Darwin width of the incident beam. In fact since the cantilever thickness is less than the extinction length, the width of the reflectivity curve is bigger than the Darwin width because of the finite size effect. This enhances the divergence of the diffracted rays from the two edges. Our investigations and modeling proved that diffraction from the two small edges have a big effect in reducing the spatial resolution of the CCD image near the cantilever edges to about 5 μm. The thickness of the cantilever is not constant at the edges which makes the case even

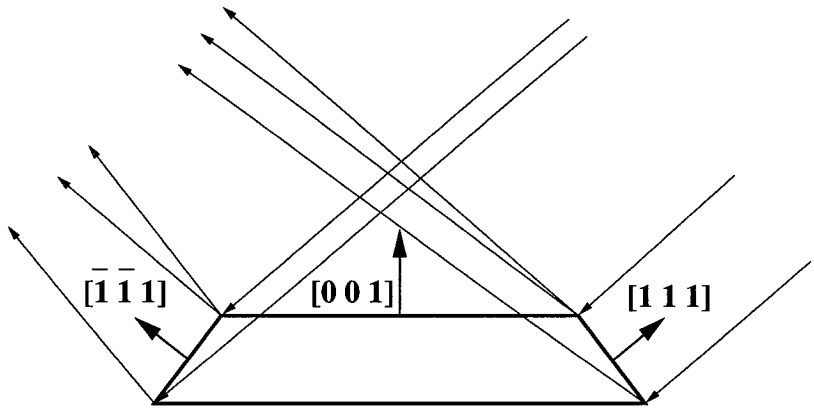

Figure 4.4: Diffraction geometry for the cantilever surfaces: The main surface normal to [001] direction is in symmetric Bragg case. The two edges are in asymmetric Laue cases.

more complicated. In our samples the cantilevers were extended on top of the base part. The asymmetric diffraction from the edges causes intensity contrast on the base along these edges. Table 4.1 summarizes diffraction parameters (see sec. 2.2.1 for definition of parameters) for different surfaces of the cantilever. The values in this table have been calculated for polarized 7.5 keV x-rays [15].

Surface normal	γ	$\Delta\theta_i^{cen}$ (mdeg)	$\Delta\theta_e^{cen}$ (mdeg)	w_i ($\times 10^{-2}$ mdeg)	w_e ($\times 10^{-2}$ mdeg)
$[\bar{1}\,\bar{1}\,1]$	3.38	-1.23	0.37	10.33	-3.05
[0 0 1]	-1	1.04	1.04	-5.62	-5.62
[1 1 1]	0.296	0.37	-1.23	3.05	10.33

Table 4.1: Dynamical diffraction parameters for the cantilever surfaces

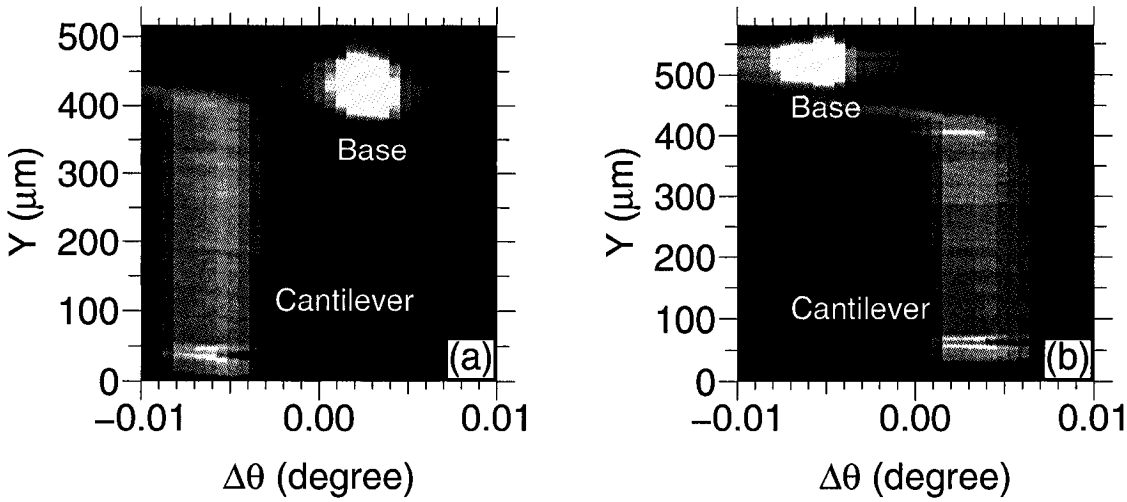

Figure 4.5: Integrated intensity (averaged over θ_{anal}) at x=275 μm vs. θ for two different samples. Cantilever is twisted with respect to the base by ~8 mdeg.

4.2.3 Measuring the cantilever twist

Our next interesting observation without much further analysis was that the straightness of the sensor could be verified from our data. In Fig. 4.5 (a) and (b) the integrated intensities averaged over 2θ are plotted versus θ along a vertical axis at the center of the cantilever for two different samples. The entire cantilever appears at the same θ angle which is slightly different from the angle of the base. This means that the cantilever itself is very straight, but the whole cantilever is twisted with respect to the base right at the junction point. The twist angle is about 8 mdeg and is in opposite directions for the two samples. The twist direction seems to be random; In two of the three samples we studied the cantilever was twisted to the left and in the third one to the right by the same amount. We propose some possible reasons for the twist:

1. The sensors are shaped from silicon wafers by wet etching. The surface of the original wafers may be miscut with respect to the $\langle 001 \rangle$ direction. In shaping the cantilever, first a big amount of material is etched from the back and then

etching is done from the front until the two etch fronts meet [135]. The base is etched less and only from one side. Since etching removes atoms in exact crystallographic directions, the final surface of the cantilever will be exactly parallel to the $\langle 001 \rangle$ planes, which may not be the case for the base. Therefore, it is likely that etching causes a small misorientation between the base and the cantilever.

2. The cantilevers are highly doped with boron atoms during the manufacturing process. Different concentrations of boron atoms in the base and cantilever may result in strain field near the junction that can disturb the orientation of the lattice by small amount.

3. There is always a thin ($\sim 10-20$ Å) silicon native oxide layer on silicon surface. This "skin" of silicon oxide can produce surface tension. Near the junction, the cantilever has oxide layer on its both sides, but the base has only one layer of oxide on top. Since the cantilever is at least two orders of magnitude thinner than the base, the effect of surface tension is greater for the cantilever. Surface tension may not be symmetric near the junction and cause small rotation of the cantilever lattice.

4. The cantilever is a very long and thin piece attached to the much thicker base. There might be some instability near the junction that perturbs the perfect alignment between the two lattices.

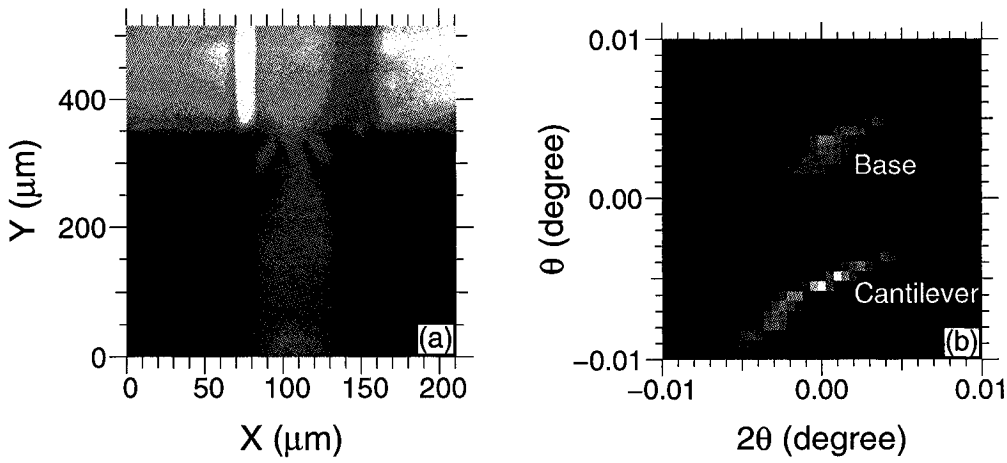

Figure 4.6: Lattice distortions near the cantilever-base junction is complicated: (a) Intensity map of the junction area near the Bragg peak. (b) $\theta - 2\theta$ map for the point marked on the left panel with coordinates (100,300). Two Bragg peaks are visible in the junction area.

In general, the structure of the junction area, where the cantilever and base lattices match, is complicated. Fig. 4.6(a) shows an intensity map of this area for θ and 2θ values near the Bragg peak. For the points close enough to the junction, two Bragg peaks (one for the cantilever and another for the base) can simultaneously be detected as Fig. 4.6(b) shows, as if the two lattices are mixed.

4.2.4 Bent versus unbent cantilever

To proceed with our analysis, we needed more quantitative information about diffraction from each point of the sample. First, to compare the bent and unbent states of the cantilever we needed a way to measure how much the cantilever was bent when the electric field was applied. We measured this by comparing the lengths of the CCD images for the two cases. As shown schematically in Fig. 4.7 (a), because of the diffraction geometry, the bent cantilever appears longer on the CCD. Fig. 4.7 (b)

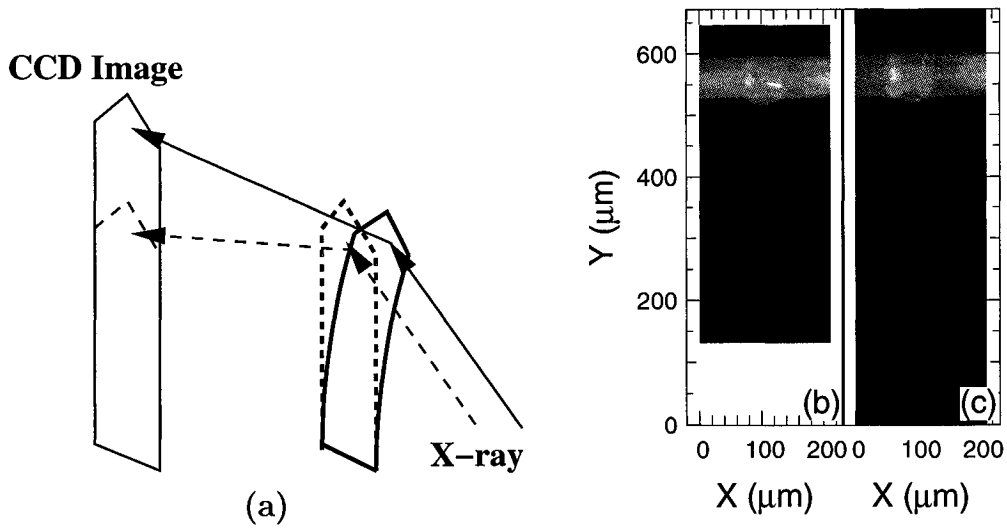

Figure 4.7: Bent and unbent cantilever images:(a) Bent cantilever produces longer image on the CCD. Integrated intensity for (b) unbent, and (c) bent cantilevers.

and (c) compare the images we obtained for the two cases. Using simple geometry considerations (see Appendix B), We calculated the slope of the bent cantilever near the tip:

$$\phi_L = \frac{\Delta h}{2D \sin \theta_B}. \tag{4.1}$$

In this formula Δh is the length difference between the two states, D is the detector-sample distance, and θ_B is the Bragg angle. In our setup Δh =$\sim$175 μm, D $\simeq$20 cm, and θ_B =37.5°. The slope we obtained from eq. 4.1 was about $7.2 \pm 0.4 \times 10^{-4}$ rad. The error was mainly in measuring the detector-sample distance D, and calculating the difference between the lengths of the images. The error in Bragg angle is negligible. Next, to measure the peak parameters such as center, height, and width, we fit a two-dimensional Gaussian function to the data at every (x, y) point on the image. It should be reminded that for a fixed (x, y) point, the 4D stack of images gives us a 2D image in θ-2θ space. We fit both the unbent and bent data. Fig.4.8 (a) shows

an example of the peak shape in θ-2θ space for a point near the center of the unbent cantilever. The peak shape specially for the unbent cantilever has a complex structure and does not completely resemble a simple 2D Gaussian function. This introduces a systematic error to our fit results which is important, for example, in calculating strain. Fig. 4.8 (b) is a plot of the same data in the reciprocal space. q_l and q_t are components of the diffraction vector normal and parallel to the crystal surface. The fact that peak shapes in the reciprocal space extend along q_l is a confirmation that these data correspond to the same point on the sample and, hence, proper restacking of data. Similar plots for the bent cantilever (Fig. 4.8 (c) and (d)) and base (Fig 4.8 (e) and (f)) are also shown. The FWHM contours of the 2D Gaussian fit functions are also plotted for comparison. As can be seen, for the bent cantilever the peak shape is considerably wider in q_t direction which suggests that the lateral size of the diffraction volume (across the cantilever width) is smaller due to anticlastic curvature of the bent cantilever [83]. Several factors can be responsible for the peak width in q_l direction: Strain causes a lattice spacing distribution from the top to the bottom of the cantilever which may increase the peak width. This, however, doesn't seem to be the dominant factor, because, as Fig. 4.8 (b) and (d) show, the width of the unbent and bent in q_l direction are almost equal. Wavelength spread of the incident beam (after the monochromator) is another factor. Different wavelengths in the incoming beam can satisfy Bragg condition with slightly different incident angles and, thus, result in diverging diffracted rays. The other very important factor is the finite thickness of the cantilever which also contributes to peak broadening in q_l direction. We show the effects of these two factors together in Fig. 4.9. Using Dumond diagrams we can calculate the effect of wavelength spread from the monochromator Si(022) reflection

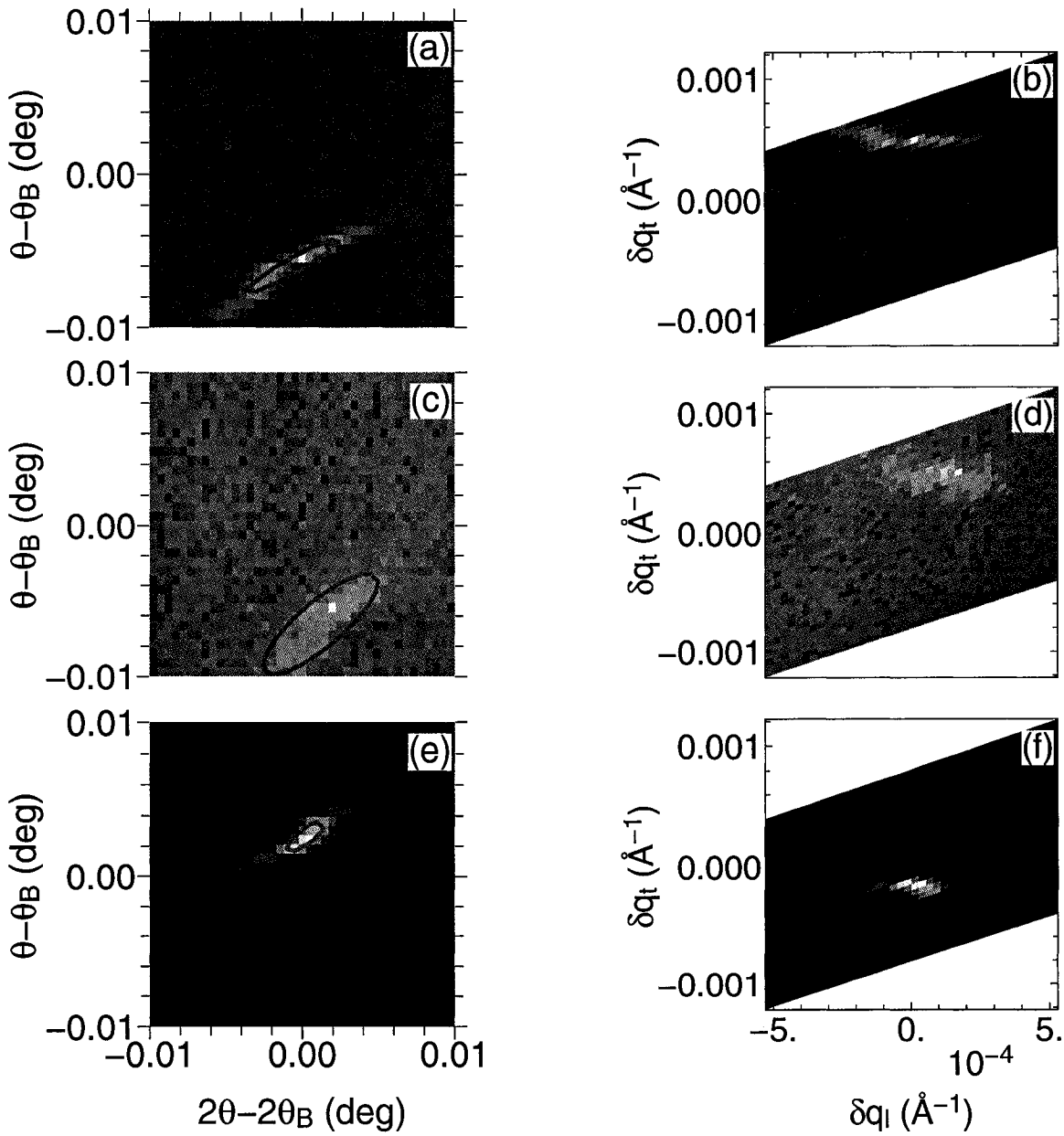

Figure 4.8: Two dimensional Bragg peaks of unbent cantilever [(a) and (b)], bent cantilever [(c) and (d)], and the base [(e) and (f)] in θ-2θ and reciprocal spaces. Solid ellipses show the FWHM contours of the 2D Gaussian fit functions.

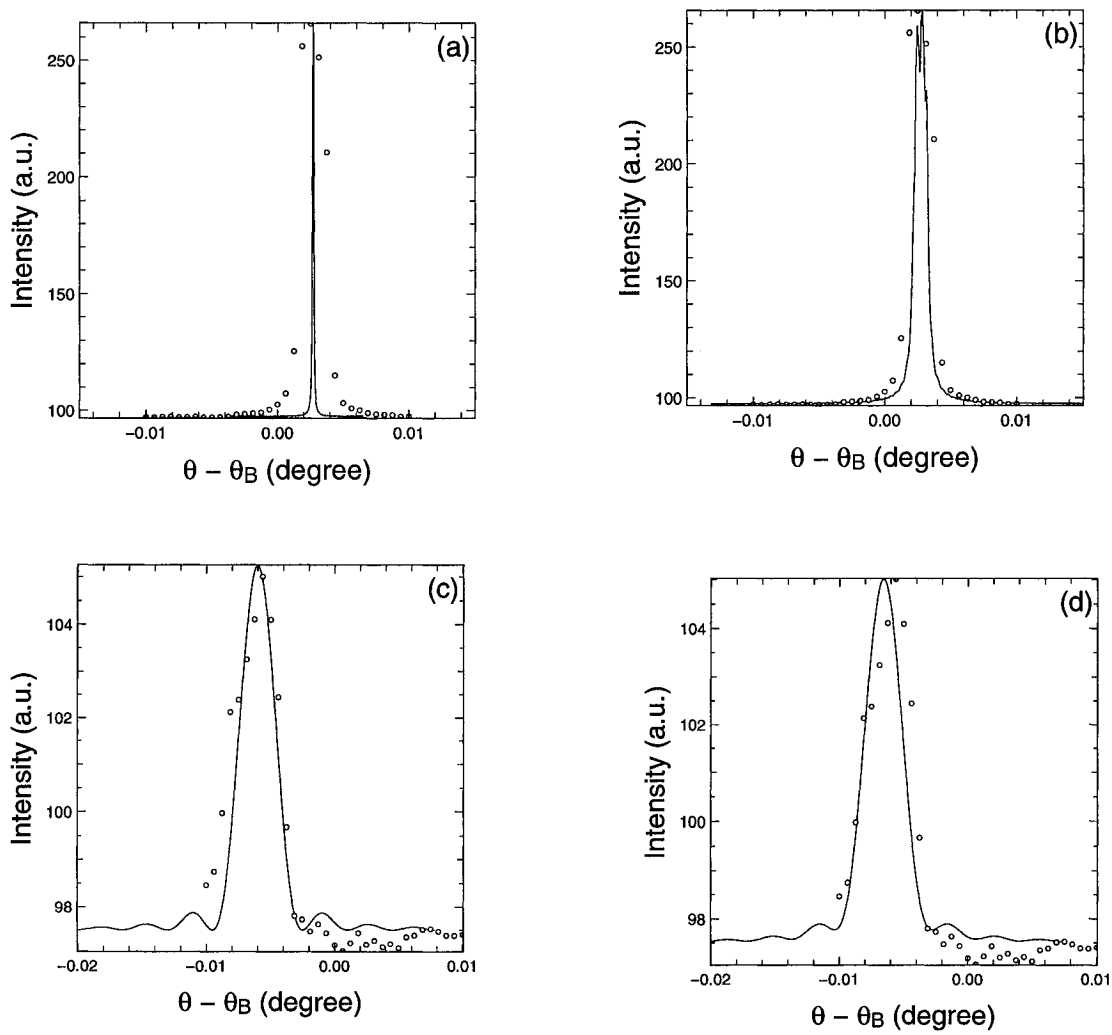

Figure 4.9: Rocking curves for: base [(a) and (b)] and cantilever [(c) and (d)] before and after taking into account the effect of the monochromator wavelength spread.

on the sample Si(004) rocking curve. Fig. 4.9 (a) and (b) show the Darwin reflectivity curves calculated without and with wavelength spread effects on top of the diffraction data for the base. As can be seen, wavelength spread is the main reason for peak broadening here and without that the experimental data is much wider than the Darwin curve. The base is much thicker than the extinction length and, therefore, the size of base does not play a role. Fig. 4.9 (c) and (d) show the same plots for the cantilever. Here, the wavelength spread correction doesn't make a big difference (if any), because, the Darwin curves are already about 10 times wider than those of the base due to the small thickness of the cantilever. For the cantilever, therefore, the finite size effect is the dominant peak broadening factor. The effect of finite thickness of the cantilever on peak broadening in q_l direction is visible in Fig. 4.8(b) and (f). In symmetric Bragg case, the Darwin width of diffraction of parallel beams from the monochromator, sample, and analyzer are 1.2, 0.45, 2.25 ($\times 10^{-4}$ Å^{-1}) respectively. The width of the base peak is in the same order, but, the cantilever peak is wider due to its finite size.

As can be seen from Fig. 4.7, to compare each point on the bent cantilever data with the same point on the unbent cantilever, we needed to map the xy coordinate system of the bent cantilever to the unbent one. This requires a coordinate transformation with proper scaling and shift values. The slope of the cantilever at each y coordinate along its length determines where the diffracted beam from that point will go on the CCD. This way, by calculating the slope of the cantilever along its length (see Appendix C) we were able to relate the two y coordinates. Then, the integrated intensities of the two rows at the corresponding y coordinates were used to interpolate the x coordinates and find the scaling and shift values. Fig. 4.10 show

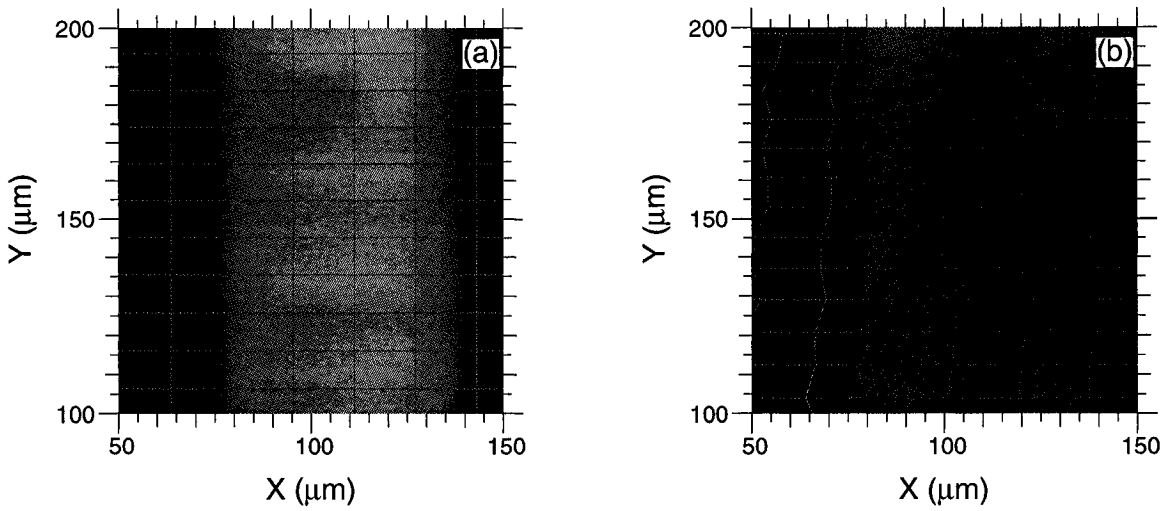

Figure 4.10: $x-y$ coordinates of the bent state (b) are mapped to the unbent system (a), to compare the two data sets.

a 100×100 μm^2 of the two coordinate systems after the mapping.

4.2.5 Strain and anticlastic curvature

After fitting our bent and unbent data with the 2D Gaussian functions, we could get a 2D map of several peak parameters such as peak height, center, and width. Before presenting the data for the cantilever, it is informative to see what the effect of bending is on the base. We examined a long slice of the base in the free and bent states. Fig. 4.11 (a) shows the slice we chose on the base. The variations of 2θ and θ are plotted in Fig. 4.11 (b) and (c) across the base. Dash-dot lines show the positions of the two edges of the cantilever. Dynamical diffraction effects can also contribute to the 2θ changes near the cantilever edges, because, diffraction from these area is not symmetric. More investigations need to be done to completely separate these effects. To calculate the strain we chose the 2θ value for the base along the central axis of the

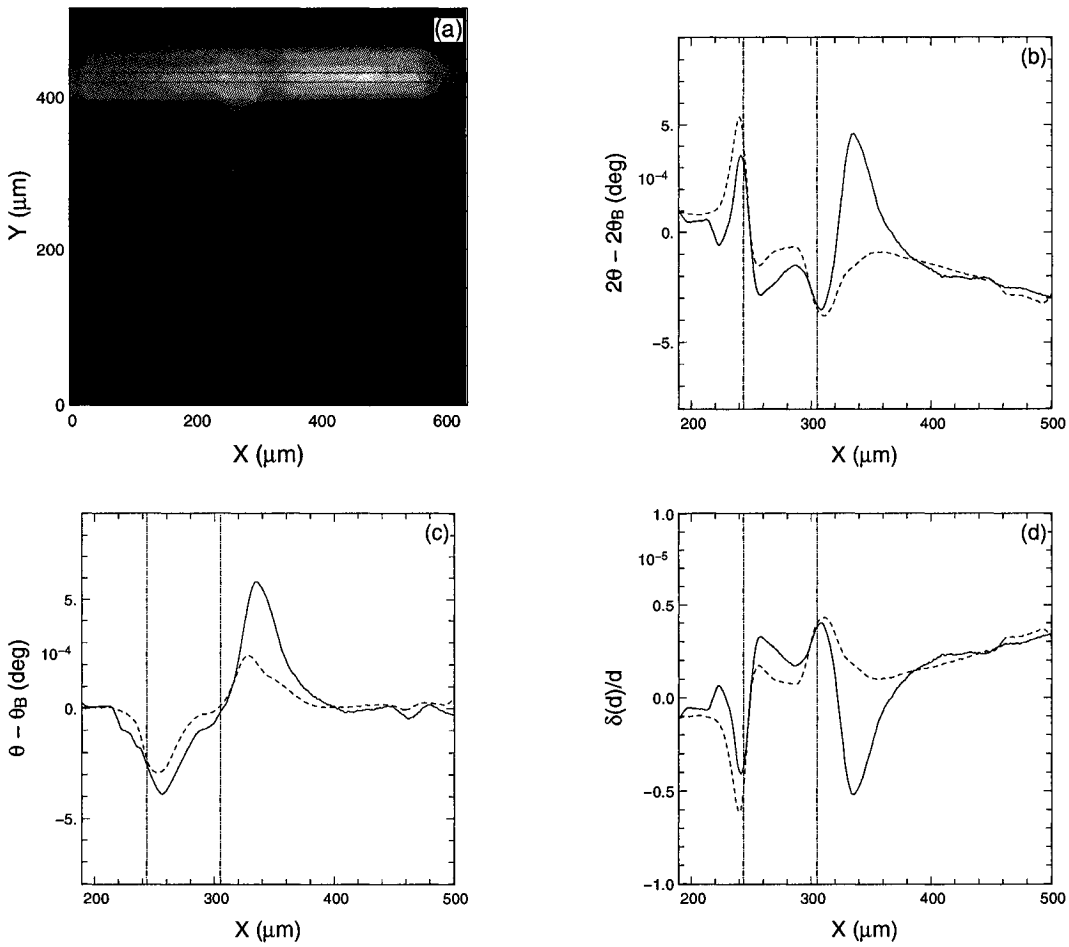

Figure 4.11: Fit results for the unbent (dashed) and bent (solid) states of the base: (a) The chosen slice of the base, (b) 2θ angle, (c) θ angle, (d) strain. The dash-dot lines show the positions of the cantilever edges.

cantilever as our reference point. The reference values for the unbent and bent states were different by 2.4 mdeg which we think is, probably, a thermal effect, because, the bent cantilever measurement was done in the night. This amount of change for silicon is equivalent to about 2.3 °C change in the temperature which is reasonable. The change in the reference lattice constants between the unbent and bent states introduces a systematic error of order of 5×10^{-6} to our strain calculations. Using the reference lattice constants for each state, we calculated the strain profile across the base. Fig. 4.11 (d) compares the two cases. As can be seen, even for the unbent state (dashed curve) there is a strain profile which is more obvious near the cantilever edges. We should recall that the cantilever trapezoidal shape extends on top of the base all the way to the area where our measurements were done. The strain profile on the base changes asymmetrically when the cantilever is bent as shown by the solid curve. This can be due to the twisted cantilever.

We now present our results for the cantilever itself. Fig. 4.12 compares the fit parameters for the two states of the cantilever. We calculated the transformed bent data maps by interpolating the bent data into the transformed coordinates as illustrated in Fig. 4.10(b). The cutoff near the tip position is due to the fact that the image of the bent cantilever exceeded the CCD recording area. Small intensity variations in Fig. 4.12 (a) is indication of thickness or beam non-uniformity as explained earlier in sec. 4.2.2. Fig. 4.12 (c) shows an interesting result of our experiment: According to the Euler-Bernoulli model [50], when a solid beam is bent along its length, it will also slightly bend across its width (Fig. 4.13(b)). This is called *anticlastic curvature* which is less than the original bending by a factor called *Poisson ratio*. The fact that different points across the cantilever width diffract at slightly different θ angles

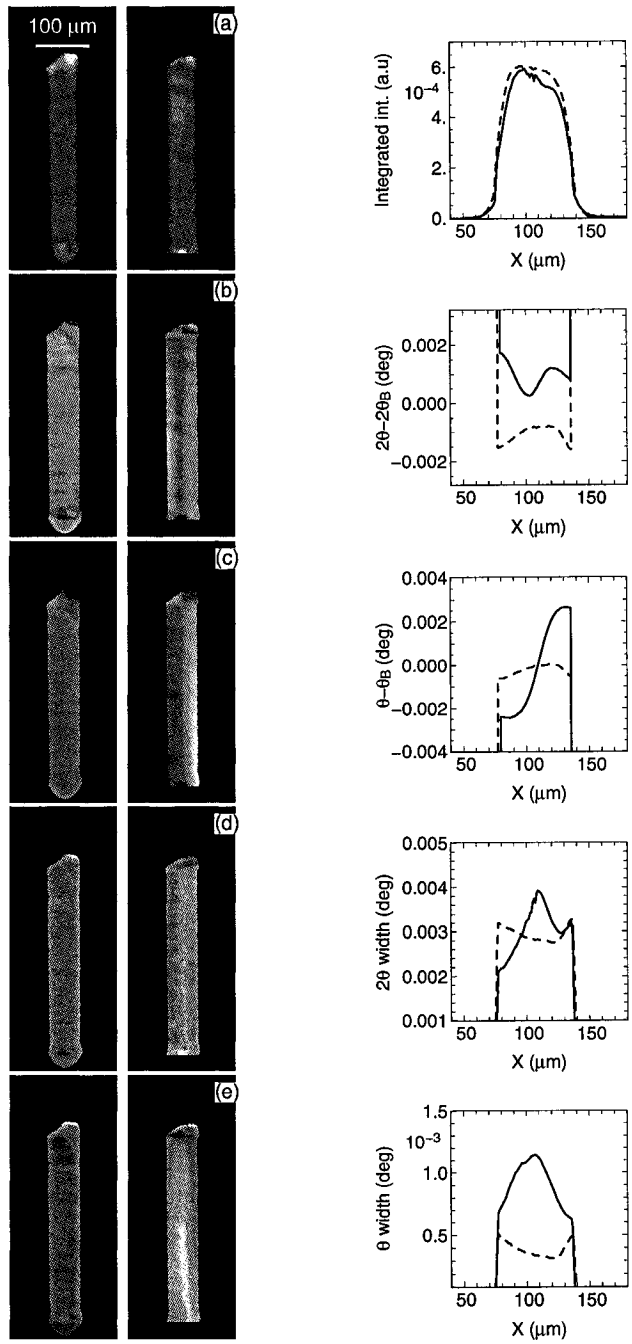

Figure 4.12: Fit results: (a) Integrated intensity, (b) 2θ, (c) θ, (d) 2θ width, (e) θ width. Left and middle columns show the 2D unbent and bent states. On the right column, dashed and solid lines are 1D cross sections of the unbent and bent states averaged over 65 μm.

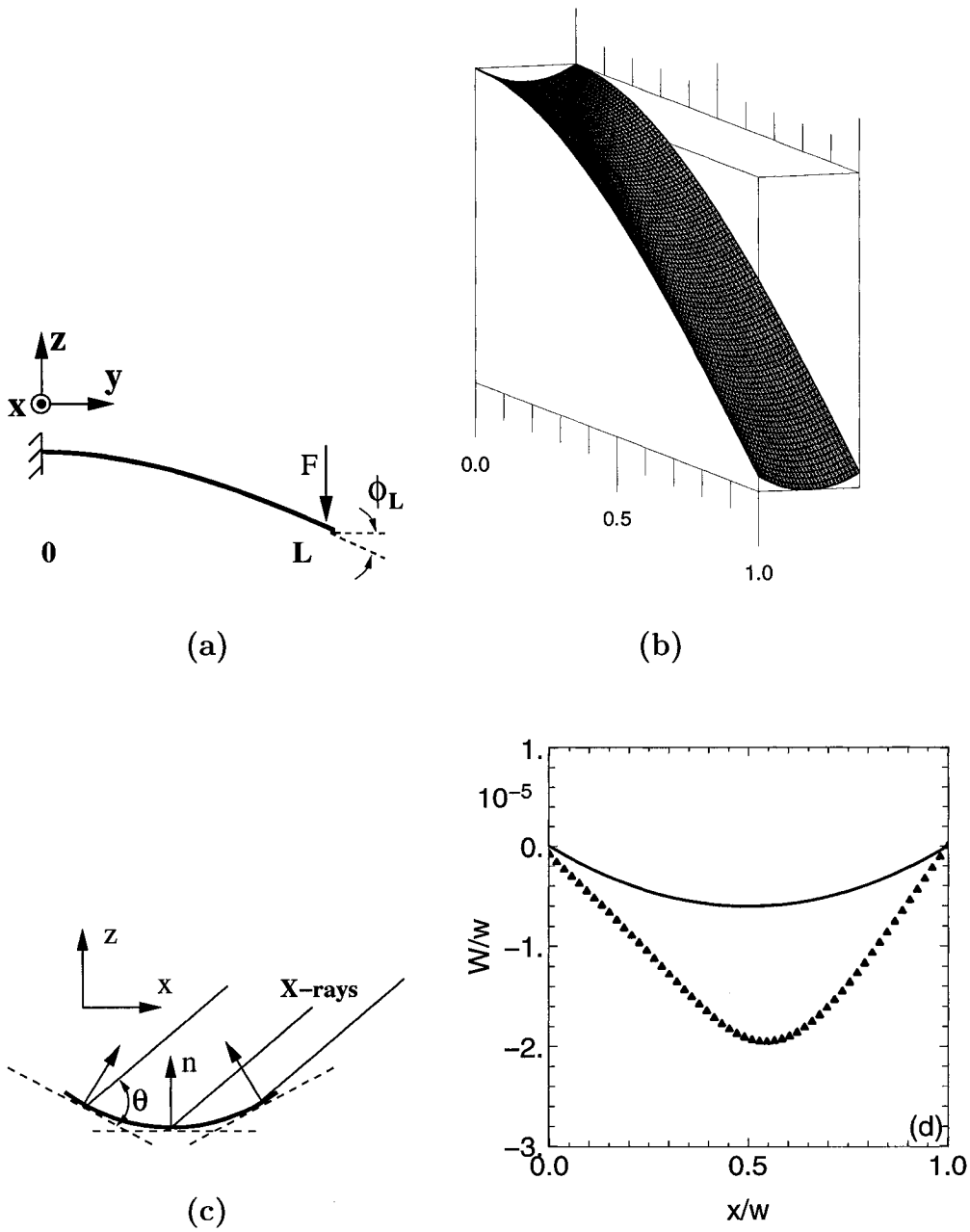

Figure 4.13: (a) Cantilever beam under localized point force F. (b) 3D demonstration of anticlastic curvature (exaggerated in z direction). (c) sample orientation angle, θ, is a direct measure of the curvature slope across the cantilever. (d) Anticlastic curvature: points (data), solid line (model).

indicates that the cantilever is curved in this direction. Notice that θ for the center of the cantilever did not change, only an increase of angles from one side to the other indicating a curved surface. The diffraction geometry across the cantilever width is shown in Fig. 4.13(c). In our case the force applied to the cantilever was a localized force near the tip. Using Euler-Bernoulli equation for a beam [50], we derived the equations for three dimensional deformations of a simple beam subjected to a localized force near the tip (Fig. 4.13(a)). Our model was similar to the description for a bent beam with a uniform bending moment [50] except we used a localized force applied near the tip of the cantilever. The details of the model can be found in Appendix C. In this model we assume a simple cantilever beam with length L fixed at one end. If a localized force F is applied to the free end of the cantilever, the (normalized to L) displacement of the cantilever in the direction perpendicular to the cantilever surface will be:

$$W = \frac{w}{L} = \phi_L(Y^2 - \frac{Y^3}{3}) + \nu\phi_L(Z^2 - X^2), \tag{4.2}$$

where $\phi_L = \frac{FL^2}{2EI}$ is the slope at the free end (see Fig. 4.13(a)), E is the *modulus of elasticity*, I is the *area moment of inertia* with respect to x axis, ν is Poisson ratio, and $X = x/L$, $Y = y/L$, and $Z = z/L$ are the normalized coordinates. The $-\nu\phi_L X^2$ term represents the parabolic anticlastic curvature which is, by a factor of ν, smaller than the actual bending along the cantilever.

In our measurements $\phi_L = 7.2 \times 10^{-4}$ rad. The Poisson ratio for crystals is usually direction dependent. For silicon, $\nu = 0.279$ for strains in $\langle\bar{1}10\rangle$ direction caused by stress in $\langle 001\rangle$ direction [14]. We used the θ variations across the cantilever as a direct measure of the cantilever anticlastic curvature. Our results (Fig. 4.12(c)) show that anticlastic curvature varies slightly along the cantilever length in agreement with

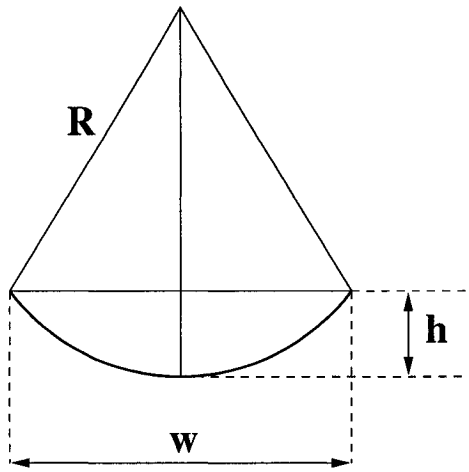

Figure 4.14: Anticlastic radius

our model. If the bending is small compared to the cantilever width, the radius of anticlastic curvature of the cantilever can be calculated using the simple sketch in Fig. 4.14:

$$R \simeq \frac{(w/2)^2}{2h}. \tag{4.3}$$

In this formula, h is the vertical displacement of the center of the cantilever with respect to the edges and w is the cantilever width. The average radius of curvature from our measurements was about $0.32 \pm 0.03\ m$. The error in Bragg angle was very small. We assumed an upper limit of 5% error in measuring the cantilever width which was more than our actual error.

Anticlastic curvature of the cantilever is plotted in Fig. 4.13(d) with dots. The parabolic profile predicted by our model with $\phi_L = 7.2 \times 10^{-4}$ rad is also plotted with solid line. We can also show that the anticlastic curvature we measured agrees with the changes in the lateral width of the Bragg peak in the bent case. As Fig. 4.8 and Fig. 4.12 (d) show, the lateral FWHM of the Bragg peak for the bent cantilever is

considerably bigger than the unbent state. The lateral (across the cantilever width) size of the coherent diffraction area is of order of anticlastic radius of curvature times the Darwin width of the Si(004) reflection ($\sim$ 0.43 mdeg). This is equal to 2.25 μm. On the other hand the lateral width of the Bragg peak in Fig. 4.8(d) is about $\delta q_t = 2.2 \times 10{-}4$ Å^{-1}. 2π over this length is equal to 2.85 μm which is close to 2.25 μm.

There are, however, discrepancies between our simple model and our data. The actual curvature is more than what our simple model predicts. Also, it doesn't show a perfect parabolic shape. it is rather sharply bent in the middle and is more straight on the sides. Possible reasons for these are discussed at the end of this section.

Another important quantity we were able to measure was the out-of-plane strain. This is basically the change in lattice spacing which can be calculated from Bragg's law:

$$\frac{\delta(d)}{d} = -\cot(\frac{2\theta}{2})\,\delta(\frac{2\theta}{2}), \tag{4.4}$$

where d is the lattice spacing and λ is the x-rays wavelength. The same quantity is also given by the derivative of eq. 4.2:

$$\epsilon_{zz} = \frac{\partial W}{\partial Z} = 2\nu\phi_L Z. \tag{4.5}$$

In our measurements x-rays penetrate through the entire cantilever thickness. Therefore, the 2θ change we measure is averaged over the cantilever thickness. According to eq. 4.5 the average of ϵ_{zz} should be zero. However, when we properly matched the unbent and bent cantilever data points and calculate the strain for each case using the reference lattice constant from the base, (Fig. 4.12(b)), we obtained non-zero strain maps shown in Fig. 4.15(a) and (b). Cross sections of the 2-dimensional maps

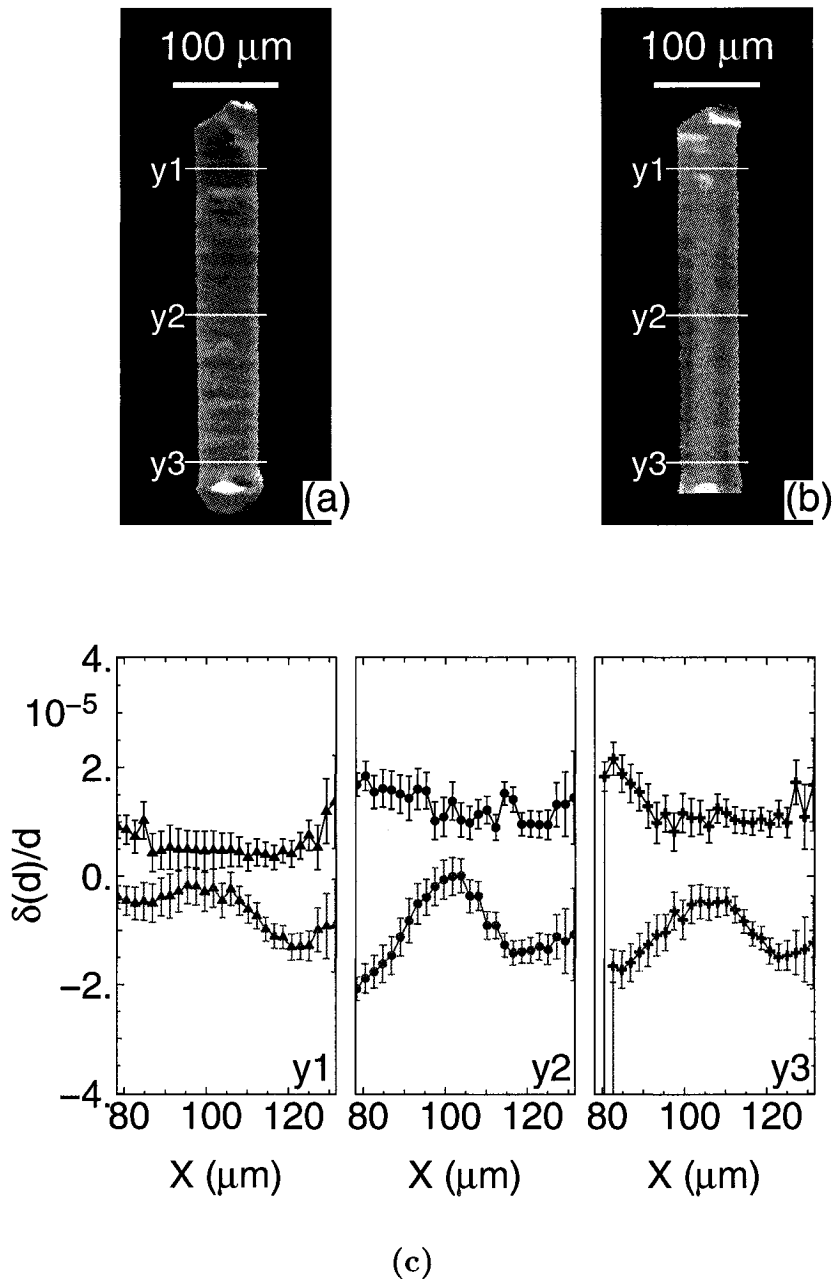

Figure 4.15: Out of plane strains: (a) Unbent cantilever. (b) Bent cantilever. (c) Cross sections at $y1 = 100$ μm, $y2 = 325$ μm, and $y3 = 550$ μm for the unbent (black) and bent (red) cantilevers.

across the cantilever at $y1 = 100$ μm, $y2 = 325$ μm, and $y3 = 550$ μm are shown in Fig. 4.15(c). There is a measurable strain even in the unbent cantilever which increases when the cantilever gets bent. The non-zero strain shows an asymmetry between diffraction from the top and bottom of the cantilever. Our model doesn't satisfy the boundary conditions at the fixed end of the cantilever. The data, however, shows that the variation of strain is less near the base, probably, because the cantilever has less anticlastic curvature in this area. The maximum strain from our data is about 2×10^{-5}.

Now we explain possible reasons for the discrepancies observed in measuring the anticlastic curvature and strain in our data. We think the simple beam model in Appendix C does not completely describe all the features we observed in our experiment. Our samples were highly doped to increase the conductivity. These extra atoms can, in principle, cause extra strain and dislocations in the original lattice [104]. The cantilever and base are shaped from a bulk wafer crystal using wet etching. It is likely that the surface of the original wafer is miscut with respect to the $\langle 100 \rangle$ atomic planes. As mentioned before, cantilever is etched from both sides and is two order of magnitudes thinner than the base. This can cause extra strain on the cantilever. Another very important factor, we think, is the native silicon oxide layer on the silicon surface. Usually, a thin ($\sim 10 - 20$ Å) layer of silicon dioxide forms on silicon surface in the vicinity of air. Recent studies [70] have shown that the native oxide layer on silicon surface can be, indeed, an order of magnitude thicker depending on the preparation method. This "skin" of silicon dioxide exerts extra surface tension on the sample. In this sense, what we have is a composite cantilever instead of a simple beam. Since the cantilever is thinner than the base by, at least, two orders of mag-

nitude, we expect the surface tension to apply a bigger distortion on the cantilever. For the points near the two edges, because of the trapezoid cross section of the cantilever, the complete symmetry between top and bottom breaks down. On the other hand, the cantilever thickness is even less in this region and it is likely that surface tension produces a big strain which propagates across the cantilever. This might be the reason for non-parabolic shape of the anticlastic curvature and big strain fields in this area.

When the more distorted cantilever lattice meets the less distorted base lattice at the junction area, the differences can cause the complicated strain field in this area which propagates into the cantilever lattice. The extent of this field must be of the order of the cantilever width which agrees with our observations. The thickness difference between the cantilever and base leads to another very fundamental issue. The thickness of the cantilever is about one order of magnitude smaller than the extinction length of the x-rays, as opposed to the base which is about one order of magnitude thicker than the extinction length. This means that x-rays penetrate completely through the thickness and diffract from all the material at both the front and back surfaces of the cantilever. Therefore, to understand the diffraction data, we should consider full dynamical diffraction of x-rays from a polyhedral shape deformed crystal [116, 117, 118]. To include the surface effects, we need a more sophisticated elasticity model which contains a composite beam. These are not trivial tasks and need more time and effort which are subjects of future work.

Chapter 5

Conclusion

In this thesis we designed and built a setup to do x-ray microdiffraction (microscopy) experiments using both x-ray microbeam scanning and x-ray diffraction imaging (topography) techniques. Both setups were finally implemented at the 8-ID-E side section of IMM/XOR-CAT (IBM, MIT, and McGill X-ray Operation and Research Collaboration Access Team) at the Advanced Photon Source, Argonne Nation Laboratory.

Our group was already involved in time-resolved and coherent x-ray diffraction experiments. The main motivation behind this work was to build a new setup to expand our group research to the x-ray microdiffraction domain. Knowing that many interesting properties of materials have their roots in the microstructure of the systems, this would give us new tools to study the physics of materials on the micrometer scale.

Our microbeam scanning setup consists of the following components (see Fig. 3.5):

- A Fresnel zone plate with a 37 cm focal length to focus 7.5 keV synchrotron x-rays to an area as small as 3 μm in horizontal and 0.3 μm in vertical.
- A fully motorized 3-axis XYZ translation stage with motion control feedback.

With the help of this stage we can scan the sample with respect to the microfocused beam in three directions with 30 nm step size over a 25 mm travel range. This stage was assembled and calibrated at McGill and then moved to the APS.

- A high resolution three circle diffractometer.
- A CCD camera with an optical microscope which is used to take images of an x-ray scintullator at 30 cm from the center of the diffractometer.

Our X-ray Diffraction Imaging (XDI) setup was based on the triple-crystal plane-wave topography technique (sec. 2.3.4.5). The main elements of this setup are (see Fig. 4.2(a)):

- A silicon (022) monochromator.
- A high resolution three circle diffractometer.
- A double crystal channel-cut analyzer consisting of two parallel silicon (111) crystals to remove the ambiguity of measuring the diffraction angle.
- A CCD camera with optical microscope providing 0.645 μm pixel size in both x and y directions.

One of the most important tasks to do after building the new setups was to test them and determine characteristics such as angular and spatial resolutions as well as other limitations on their use. To achieve this goal, we did two case studies. Apart from the scientific interest and practical applications of these two experiments, they were mainly chosen to characterize our setups. For us they served as working grounds to develop the necessary tools for doing x-ray microdiffraction experiments, discover challenges one has to face, and try to understand and resolve them.

In our first experiment, we used our microfocusing and XDI setups to study the microstructure of 90° ferroelectric domains and domain walls in barium titanate ($BaTiO_3$) single crystals. Our sample had 10 μm wide alternating stripe-shape a and c domains. $BaTiO_3$ is a well studied material, however, the fine structure of these domains and the profile and dimension of the domain boundaries have been the subject of debate since its discovery. For us, the two types of domains, having different crystallographic structures and micrometer dimensions, provided an ideal system to be studied with our microdiffraction setups. Before doing x-ray microdiffraction measurements, we measured the precise lattice constants of our samples by directly mapping the Bragg peaks in the reciprocal space. This was done using our high resolution diffractometer and Cu kα_1 radiation at McGill. Calculation of domains orientation using lattice constants and direct measurement of the angle between the diffraction vectors in the reciprocal space agreed within the experimental errors. We found that the average angle of the domain walls with the crystal surface was 44.684±0.008°. Then, we used our microfocusing setup to scan a 60 μm×60 μm square of our sample in 3 μm steps. At each step we measured both the a and c Bragg peaks. After fitting the data we were able to get two-dimensional maps of the two types of domains (Fig. 3.7). This measurement showed alternating 10 μm wide stripe-shape a and c domains pattern in agreement with our optical measurements. In another measurement, to determine the fine structure of domain walls, we scanned a 40 μm distance of our sample perpendicular to the domains orientation in 0.5 μm steps. At each point we measured $\theta - 2\theta$, 2θ, and χ scans for a and c domains. In this measurement also we observed 10 μm wide domains and a ~5 μm inter-domain region where both the neighboring domains had detectable contributions. This agrees

with the ~45° orientation of the 90° domain walls and the 5.41 μm absorption length of the crystal for the wavelength we used. To obtain detailed information about the structure of the domain walls, we fit our data to a simple model based on partial contributions of a and c domains separated by 45° walls to diffraction of x-rays at each point. Integrated intensity of diffraction from domains showed sudden "kinks" (see Fig. 3.10) which could not be adequately explained by this simple model. To explain this feature of data, we replaced the straight-line walls in our model by "broken" wall shapes whose orientation change near the crystal surface (see Fig. 3.11). The new model considerably improved our fit results. We discovered a ~1 μm thick surface-like layer underneath the crystal surface where the orientation of domain walls changes from ~45° to ~20°. This deviation from bulk profile is to minimize the total deformation energy near the crystal surface. We then fit our scan peaks to Gaussian functions to study variations of the peak angles and widths. From these fits we were able to plot domain orientation and the change in the lattice constant (strain) across the a and c domains. Our results showed that the lattice is under tension at one side of each domain and is compressed by almost the same amount at the other side (Fig. 3.12(c)). Maximum strain occurs where the kink in the data is observed within the surface-like layer. This behavior can be explained if each domain lattice is considered as a crystallite clamped between the two neighboring domains. Difference between domains thicknesses near the crystal surface causes domain-domain interactions of opposite signs and, thus, compressive and tensile strains at the domain walls. The two angles of each domain wall, the transition point from bulk-like to surface-like angle, and the intersection of each domain wall with the crystal surface can be unambiguously deduced from the results of our fit. The finite size effect due

to domain thickness variation is manifested in the peak width which is also more profound near the domain boundaries. From θ and χ angles we could get information on the rotation of the domains axes. Again, domain rotation angle is asymmetric and more obvious in the surface-like region. We also realized that the elastic distortion field around the domain walls expands several microns away from the walls.

In another set of experiments, we combined our microfocusing and XDI microdiffraction setups together to image the 90° domains in our sample. In this experiment an area of 500 μm$\times$500 μm on the sample was illuminated by a parallel x-ray beam and the rocking curve of the sample was recorded with a CCD detector with 0.645 μm resolution in both horizontal and vertical directions. From the topography images we observed that different areas on the sample are slightly tilted with respect to each other so that they appear bright at different angles as the crystal rocks (see Fig. 3.13). We then inserted the Fresnel zone plate into the beam to switch to the microfocusing mode. In the XDI mode we can get a quick image of the whole area of the sample at once and areas of interest can be identified. When we switch to the microfocusing mode by inserting the Fresnel zone plate, the position of each spot on the sample can be registered with respect to the microfocused beam (Fig. 3.14). This eliminates the need to scan the whole sample, common in almost all scanning techniques, to find the desired area on the sample.

There were other subjects that we were initially planning to study but they didn't fit in the time frame of this thesis. The most exciting one, perhaps, is the domain switching and dynamics of domain walls motion. Theories exist to explain the development of new domains, domain switching, and motion of domain walls [86, 62, 97]. There are also studies of the motion of domain walls in ferroelectric

materials [139, 125]. Our idea was to apply an electric field to our sample and study the motion of a single domain wall in real time using a fast x-ray detector such as a streak camera. Our microdiffraction setups allow us to study the changes in the structure of two adjacent domains with enough resolution when applying an electric field. The other interesting topic to study is the 180° domains. In principal, x-rays cannot discriminate between 180° domains, because, they have the same structure (Friedel's law). However, by applying an electric field, the polarization of the domains will expand or shrink depending on whether they are parallel or antiparallel to the electric field. This can make one orientation of domains favorable in an x-ray study. These topics are subjects of future work in the ferroelectric materials.

In our second project, we did a unique set of measurements to study lattice distortions in a micron-size single crystal silicon cantilever used in scanning probe microscopy. Our cantilevers were 450 μm long, 50 μm wide, and 1.7 μm thick. Identifying these imperfections is important for the SPM device manufacturers and users. For us, however, measuring lattice distortions in such a tiny and literally perfect crystal was more a way to better understand our new setups. We did several plane wave XDI measurements on our cantilevers in the free (unbent) state. Our setup was a triple-crystal (monochromator, sample, analyzer) in all of our experiments. We performed sample and analyzer scans with 0.625 mdeg and 0.5 mdeg resolutions and recorded the images of the whole cantilever using a CCD camera with 0.645 μm pixel size. In order to track each point of the sample in a series of images recorded in each scan, we developed a mechanism to correct for the per-frame shift caused by rocking the analyzer. To understand this phenomenon we had to do several simulations and tests. We called this procedure *restacking* which, to our knowledge, has not been utilized

by others before. With the aid of the analyzer we were able to uniquely associate the image points to the corresponding places on the sample. This is a major and not so trivial issue in XDI. To interpret the results of this type of experiments, a full understanding of the diffraction in the context of dynamical diffraction is necessary. For example, we realized that the small wedge-shape surfaces at the two sides of the cantilever behave differently and considerably reduce the spatial resolution of the images.

By calculating the integrated intensity from our measurements we were able to map the small variations in the cantilever thickness (Fig. 4.3(b)), because, the cantilever thickness was an order of magnitude smaller than the extinction length of the x-rays. These variations can be a result of non-uniform etching during the manufacturing process. This proves that XDI can be used to get a 2D map of the thickness variations in sufficiently thin crystals.

Sample angle, showed that the cantilever itself was very straight but the whole cantilever piece was twisted at the junction with respect to the bulky base, even though they were one single piece of crystal (see Fig. 4.5). Our measurements showed a 0.008° twist angle to the left or right for different samples. The cause for the twist is, most likely, different etching for the base and cantilever, additional dopant atoms, thickness difference between the base and the cantilever, or surface tension exerted by the thin oxide layer on the surface of the sample. We still need to do more measurements to clearly identify the cause for the twist. Near the base we could measure two separate Bragg peaks at each point, one for the base and another one for the cantilever (Fig. 4.6(b)) showing the complicated structure of this area.

We repeated the measurements with the cantilever slightly bent by applying an

electric field. The bent angle was measured indirectly by comparing the image lengths of the bent and unbent cantilevers. This showed that the slope of the bend cantilever at its end was in the order of 7×10^{-4} rad. The Bragg peak shapes in the reciprocal space showed wider peaks in the direction perpendicular to the diffraction vector (Fig. 4.8), an indication of anticlastic curvature of the bent cantilever. To obtain quantitative and detailed information about the lattice distortions, we fit a two-dimensional Gaussian peak shape to the θ-2θ diffraction pattern of each point of the sample. For one-to-one comparison of the points on the bent and unbent cantilevers, we developed a sophisticated method to transform coordinate of the bent cantilever to the unbent coordinates system. After fitting and coordinate transformation, we obtained very interesting results: a complete two-dimensional map of anticlastic curvature and strain field for the cantilever.

Variations of the sample scan angle across the cantilever width directly measures the anticlastic curvature. Precise measurements of this parameter showed about 4 mdeg change across the cantilever width. This translates to a radius of curvature of about 0.3 m. To compare this and other results with theory, we calculated the three dimensional deformations of a simple cantilever beam fixed at one end and subjected to a localized force at its free end (Appendix C). The anticlastic curvature we measured was almost 4 times bigger than what our simple model predicts (see Fig. 4.13 (d)) and didn't exactly show the parabolic profile as in simple the model. The cantilever was rather sharply bent in the middle and less curved at the two sides.

Another very important quantity is the out-of-plane strain which can be calculated from the changes in the lattice spacing with respect to the base lattice constant which we considered as reference. This is itself given by variations of the diffraction angle

2θ. Our calculation showed non-zero strain even in the unbent state. The strain has nearly parabolic shape across the cantilever width and reaches a maximum 2 $\times 10^{-5}$ near the edges of the cantilever. According to our simple model the strain averaged over the cantilever thickness must be zero. Our measurements suggests that the top and bottom parts of the cantilever are not exactly symmetrical leading to a non-zero average strain profile.

The discrepancies between our results and the predictions of the simple cantilever model suggest that our cantilevers are not, indeed, simple homogeneous beams. The cantilever and base parts were etched differently. The cantilever part was etched from both sides, but, the base only from one side. In general the cantilever was at least two order of magnitude thinner than the base and is more likely to be susceptible to surface effects. The samples were highly doped to increase their conductivity which may introduce extra strains and dislocations in the lattice. Another possible factor is the skin of silicon oxide on the surface of the cantilevers. This layer can produce surface tension on the crystal and exert extra pressure on the internal material. Near the base-cantilever joint area the thin cantilever has oxide layer both on top and bottom surfaces. The thicker base, on the other hand, has oxide only on the top surface. This can be a reason for the complicated strain distribution in this area and the twist between the cantilever and the base. The symmetry between the top and bottom of the cantilever breaks down near the two wedge-shape edges of the cantilever. These areas have also less thickness and more affected by the surface tension. We think these can be a source of asymmetry and non-zero strain in these areas which propagates across the cantilever width. Another more fundamental issue is that we need to incorporate dynamical diffraction from thin deformed crystals with polyhedral

cross section into our models to be able to properly explain our data. Considering the complexities in the structure of these cantilever, it seems unfeasible to find a simple analytical model which also satisfies all the imposed boundary conditions. Instead, a Finite Element calculation seems to be more practical for this purpose and is, therefore, recommended. Also, from experimental point of view, larger deflections of the cantilever will help to better distinguish deformation effects from dynamical diffraction and residual strain effects. These are all subjects of future work in this area.

The two systems studied in this thesis are just examples of what can be accomplished by x-ray microdiffraction techniques. These systems didn't have any special feature other than a microstructure detectable by x-rays. The results of these studies confirm how modern x-ray sources and x-ray optical devices can be utilized to design unique x-ray microdiffraction experiments to study the microstructure of literally any system that can be studied by x-rays. With the increasing need to fabricate micro and nano devices and growing number of micromachining facilities, x-ray microdiffraction seems to be a very promising and necessary method to control, test, and characterize these products. Our studies also show that dynamical theory of x-ray diffraction plays an essential role in proper interpretation and understanding of x-ray microdiffraction studies of high quality crystals on micrometer scales. In our studies we combined spatial and angular scans to get full diffraction data from each point of the sample. We also developed techniques, many unique and original in their nature, to interpret and analysis x-ray microdiffraction data. We believe these experimental and analytical methods can be applied to similar x-ray microdiffraction experiment. We demonstrated how the strengths of x-ray microfocusing and diffraction imaging

techniques, when combined together, can be exploited to perform more precise and faster measurements. We intend to continue and extend our work in this area and believe this will open a new path in our research to study a wide range of interesting physical phenomena in materials.

Appendix A

A model for x-ray microdiffraction from 90° domains in $BaTiO_3$

A model is developed here to describe x-ray microdiffraction from 90° domains in $BaTiO_3$. We assume an alternating series of a and c domains separated by sharp interfaces. z and y are coordinates in the direction of domains extension and into the crystal surface, respectively, as shown in Fig. A.1. Each domain boundary intersects the crystal surface at Z_n, and has an arbitrary profile given by function $Y_n(z')$:

$$Y_n(z') = \begin{cases} 0 & , z' \leq Z_n, \\ W_n(z') & , z' > Z_n. \end{cases} \tag{A.1}$$

Incident and diffracted beams are in $x - y$ plane (see Fig. 3.5) and the sample is scanned in z direction. The diffraction signal $\delta(dI)$ from a small volume $dy \times dz'$ centered at point (y,z') of the crystal is proportional to this volume and the total absorption by all the material above:

$$\delta(dI) = e^{-2\mu y}\, dydz', \tag{A.2}$$

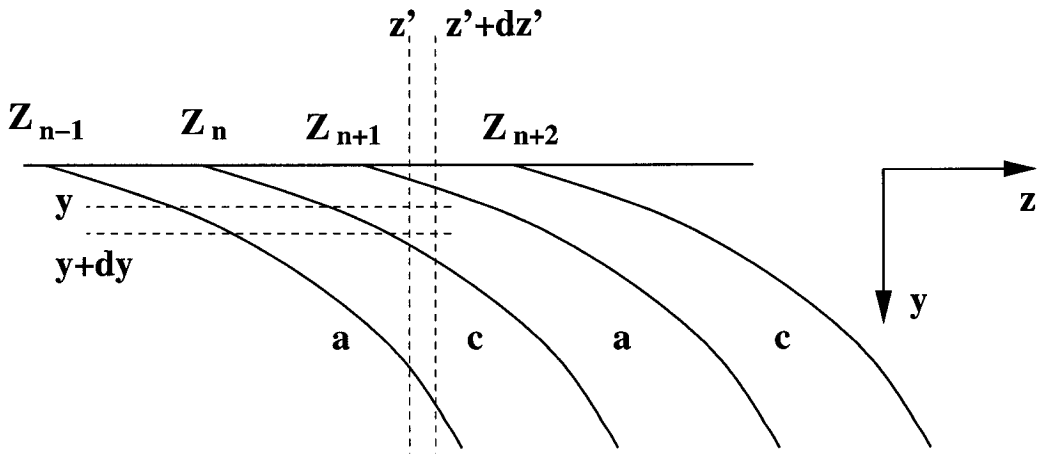

Figure A.1: Microdiffraction model for 90° domains

where μ is the absorption coefficient of the crystal. For this narrow beam, diffraction of a single domain between walls n and $n+1$ is then equal to:

$$\begin{aligned} dI_n &= dz' \int_{Y_{n+1}(z')}^{Y_n(z')} e^{-2\mu y}\, dy \\ &= \frac{1}{2\mu}[e^{-2\mu Y_{n+1}(z')} - e^{-2\mu Y_n(z')}]. \end{aligned} \tag{A.3}$$

One more integration over z' gives the total diffraction for the microbeam:

$$I_n = \frac{1}{2\mu}[\int_{z-\frac{b}{2}}^{z+\frac{b}{2}} e^{-2\mu Y_{n+1}(z')} dz' - \int_{z-\frac{b}{2}}^{z+\frac{b}{2}} e^{-2\mu Y_n(z')} dz'], \tag{A.4}$$

where z is the center of the microbeam and b is its width in the scan direction. To obtain the total diffraction signal of c or a domain types at each point z, we have to add only those I_n terms corresponding to that domain type. This means adding odd or even terms separately. Integrals in eq. A.4 can be calculated either analytically for simple geometries, or numerically for more complicated cases. For example, function

$W_n(z)$ for straight 45° walls is given by:

$$W_n(z') = (z - Z_n). \tag{A.5}$$

In our proposed domain wall profile, the domain boundary consists of two line segments each with different slops:

$$W_n(z'; \alpha_1, \alpha_2, h) = \begin{cases} (z' - Z_n)\tan\alpha_1 & , z' \leq Z_n + h\cot\alpha_1, \\ h + (z' - h\cot\alpha_1)\tan\alpha_2 & , z' > Z_n + h\cot\alpha_1. \end{cases} \tag{A.6}$$

where α_1 and α_2 are near-surface and bulk slopes of the wall and h is the depth where the slope changes (the kink).

Appendix B

Slope of a bent cantilever and its diffraction image

Suppose a set of planes parallel to z axis are set to Bragg diffraction. If we take $-y$ axis along the incident wave vector, $\mathbf{k}_i = k(0, -1, 0)$, the exit wave vector $\mathbf{k}_e$ will be in $x - y$ plane (Fig. B). If the planes are tilted by a small angle, χ, the reciprocal vector, $\mathbf{G}$, normal to the surface will be given by:

$$\mathbf{G} = G(\cos\chi\cos\theta_B, \cos\chi\sin\theta_B, \sin\chi), \tag{B.1}$$

where θ_B is the Bragg angle. In this case $\mathbf{k}_e$ will also have an azimuth angle α with the $x - y$ plane:

$$\mathbf{k}_e = k(\cos\alpha\sin 2\theta_B, -\cos\alpha\cos 2\theta_B, \sin\alpha). \tag{B.2}$$

From Laue condition (eq. 2.17) we have:

$$\mathbf{k}_e - \mathbf{k}_i = \mathbf{G}. \tag{B.3}$$

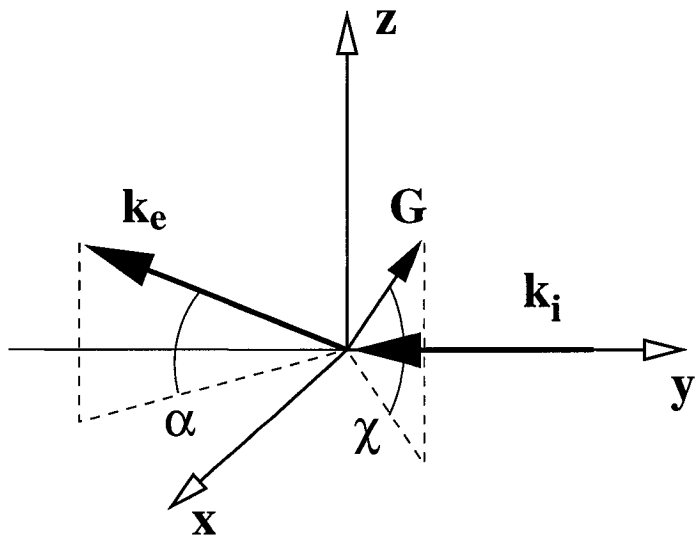

Figure B.1: Diffraction spot displacement when tilting the crystal.

The z component of this equation relates the two azimuth angles:

$$k \sin \alpha = G \sin \chi. \tag{B.4}$$

The rate of change of α with χ for small angles is therefore given by:

$$\frac{d\alpha}{d\chi} = \frac{\cos \chi}{\cos \alpha} \frac{\lambda}{d} \simeq 2 \sin \theta_B. \tag{B.5}$$

Because $k = \frac{2\pi}{\lambda}$ and $G = \frac{2\pi}{d}$, where λ is the wavelength and d is the spacing between the planes. We also assumed that α and χ are both small angles. If the detector is located at distance D from the origin, the displacement of the diffraction spot will simply equals to:

$$\Delta h = D\alpha = 2D \sin \theta_B \chi. \tag{B.6}$$

If Δh is known, from this equation we can calculate the tilt angle:

$$\chi = \frac{\Delta h}{2D \sin \theta_B}. \tag{B.7}$$

Moreover, the x component of eq. B.3 can be used to show that the diffraction angle doesn't change much when tilting the planes by a small angle:

$$k \cos \alpha \sin 2\theta_B = G \cos \chi \cos \theta_B. \tag{B.8}$$

If we take derivative with respect to χ we get:

$$-k \sin \alpha \sin 2\theta_B \frac{d\alpha}{d\chi} + k \cos \alpha \cos 2\theta_B \frac{d(2\theta_B)}{d\chi} = -G \sin \chi \cos \theta_B. \tag{B.9}$$

For small tilt angles, $\sin \alpha = \sin \chi \simeq 0$. Then we have:

$$\frac{d(2\theta_B)}{d\chi} \simeq 0. \tag{B.10}$$

Appendix C

Three dimensional deformations of a simple cantilever beam

We did not find a detailed calculation of the three dimensional deformations of a simple cantilever beam fixed at one end and subjected to a point force at its other end. So, in this appendix we derive a simplified case following the same method described by Ford [50] for the case of a uniform bending moment. Our solution doesn't satisfy all the boundary conditions at the fixed end of the cantilever, but these only affect the solutions within a size of the cantilever width and, therefore, the solutions derived here provide a good approximation for the points far enough from the fixed end of the cantilever.

Consider a simple homogeneous beam of length L, width b, and thickness t. The coordinate system axes are parallel to the beam edges and set so that the beam surfaces are at $x = -b/2, x = +b/2$, $y = 0, y = L$, and $z = -t/2, z = t/2$. The beam is fixed at $y = 0$ and a localized force F is applied to its free end at $y = L$ (Fig. C.1(a)). F is negative for a force downward. Our goal is to derive equations for the three dimensional deformations at each point of the beam. Equilibrium equations

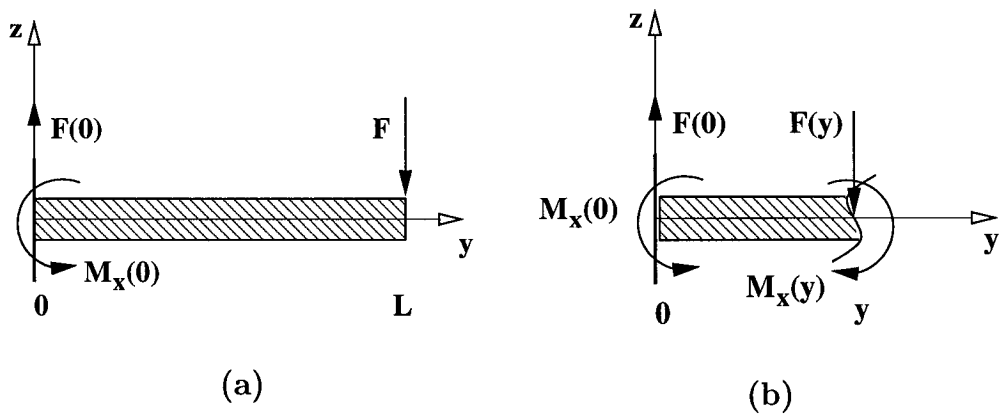

Figure C.1: Geometry of the model: the beam is fixed at one end and a localized force F is applied to its free end at $y = L$.

for the whole beam are:

$$F(0) + F = 0, \tag{C.1}$$

$$M_x(0) + LF = 0, \tag{C.2}$$

where $F(0)$ is the reaction force along z, and $M_x(0)$ is the bending moment about x axis at $y = 0$. At any point y along the beam (Fig. C.1(b)), the equilibrium equations are:

$$F(0) + F(y) = 0, \tag{C.3}$$

$$M_x(0) + yF(y) + M_x(y) = 0. \tag{C.4}$$

From eq. C.1, and eq. C.3 we get the force and bending moment at each point

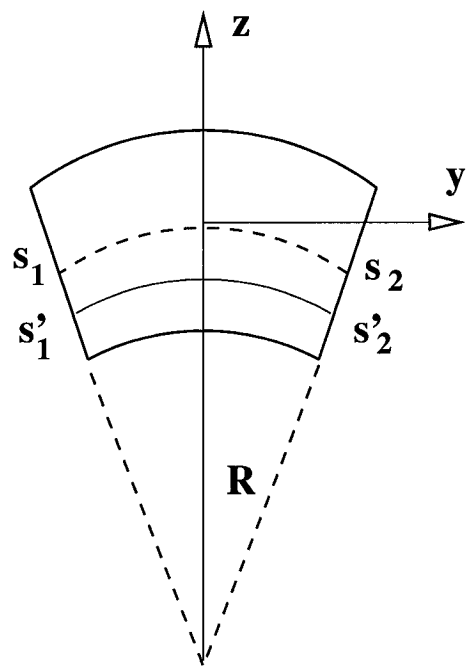

Figure C.2: Strain in a small segment of the bent beam: the top surface is under tension and the bottom surface is under compression. The dashed line shows the neutral axis of the beam. Note that in this figure R is negative.

along the beam:

$$F(y) = F, \tag{C.5}$$

$$M_x(y) = FL(1 - Y). \tag{C.6}$$

In this equation $Y \equiv y/L$ is the normalized (to length) coordinate along the cantilever. The beam gets deformed under these reactions. We use s as the coordinate along the cantilever length and consider a small segment of the bent beam between $s = s_1$ and $s = s_2$ (Fig. C.2(a)). The top surface of the beam is under compression and the bottom surface is under tension, therefore the strain must be zero somewhere in

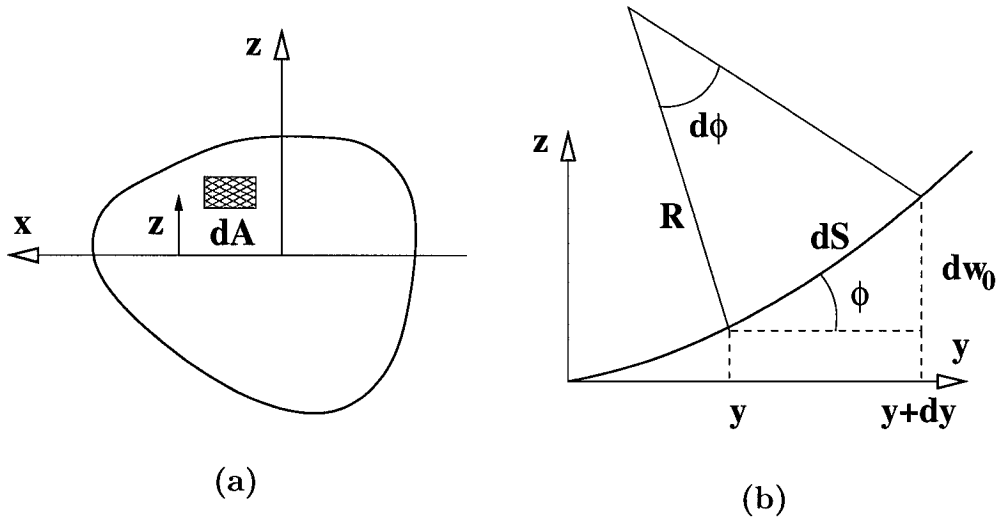

Figure C.3: (a) cross section of the beam. (b) bent beam curvature.

between. This is called the *neutral axis* of the beam. For a beam with a symmetric cross section, like what we have here, the neutral axis lies on the $z = 0$ plane. The y component of the strain at z is equal to:

$$\epsilon_{yy} = \frac{s_1' s_2' - s_1 s_2}{s_1 s_2} = \frac{(R - z)d\phi - Rd\phi}{Rd\phi} = -\frac{z}{R}. \tag{C.7}$$

If $R > 0$, ϵ_{yy} is compressive for $z > 0$ and tensile for $z < 0$. The bending moment $M_x(y)$ can be calculated from the stress component σ_{yy}. Suppose the beam has an arbitrary cross section profile shown in Fig. C.3(a). The bending moment can then be calculated from the sum of the torques at each small surface element:

$$\begin{aligned} M_x(y) &= -\int_A \sigma_{yy} z dA = -E \int_A \epsilon_{yy} z \, dA \\ &= \frac{E}{R} \int_A z^2 \, dA = \frac{EI}{R}, \end{aligned} \tag{C.8}$$

where E is the *module of elasticity*, and $I \equiv \int_A z^2 dA$ is the *area moment of inertia*

of the beam cross section with respect to the x axis. The curvature of the beam is by definition equal to: $\frac{1}{R} = -\frac{d\phi}{ds}$ (see Fig. C.3(b)). Let w_0 be the z displacement of the beam natural axis. For small deflections of the beam, $\phi \simeq \frac{dw_0}{dy}$ and $ds \simeq dy$. Therefore we get:

$$\frac{1}{R} \simeq \frac{d^2w_0}{dy^2}. \tag{C.9}$$

By combining eq. C.8 and eq. C.9, we obtain the following equation relating the curvature of the beam to the bending moment at each point:

$$\frac{d^2w_0}{dy^2} \simeq \frac{M_x(y)}{EI}. \tag{C.10}$$

Substituting eq. C.6 into the above equation, we obtain:

$$\frac{d^2w_0}{dy^2} \simeq \frac{FL}{EI}(1 - Y). \tag{C.11}$$

We can obtain the slope of the cantilever at each point by integrating this equation. Since the fixed end of the cantilever remains straight, the boundary condition will be: $\frac{dw_0}{dy}[y = 0] = 0$,

$$\phi = \frac{dw_0}{dy} = \phi_L(2Y - Y^2). \tag{C.12}$$

The end slope of the cantilever ϕ_L, is defined as:

$$\phi_L = \frac{FL^2}{2EI}. \tag{C.13}$$

We can find an equation for the displacement by integrating the slope once more with

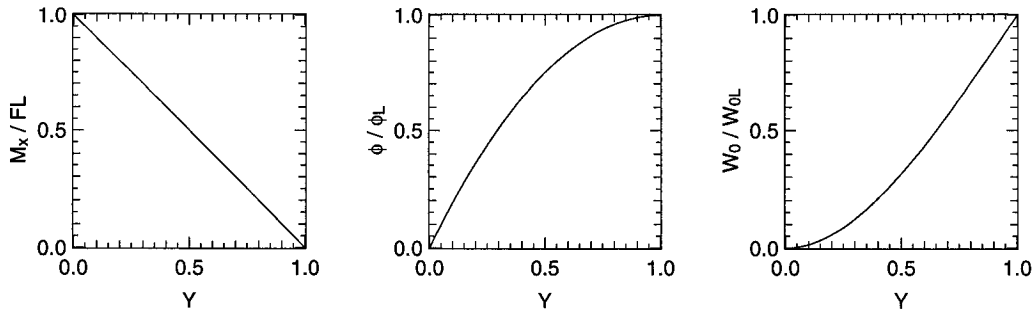

Figure C.4: Deformed cantilever beam: (a) Bending moment, (b) Slope, and (c) Deflection versus the dimensionless length Y.

the boundary condition that $w_0\,[y = 0] = 0$ (the fixed end of the beam doesn't move):

$$W_0 = \phi_L\,(Y^2 - \frac{1}{3}Y^3) \tag{C.14}$$

$$= W_{0L}\,(\frac{3}{2}Y^2 - \frac{1}{2}Y^3), \tag{C.15}$$

where $W_0 = w_0/L$ is the normalized (to length) displacement in z direction and $W_{0L} = \frac{2}{3}\phi_L$ is the maximum displacement at $y = L$. Equations C.6, C.12, and C.14 are plotted in Fig. C.4. Note that F, ϕ_L, and W_{0L} are negative for a force pointing down.

Now let $u(x, y, z)$, $v(x, y, z)$, and $w(x, y, z)$ be the deformations in x, y, and z directions at point (x, y, z). The y component of the strain is defined as $\epsilon_{yy} \equiv \frac{\partial v}{\partial y}$. From eqs. C.7, C.8, and C.6 we get:

$$\epsilon_{yy} = \frac{\partial v}{\partial y} = -\frac{FL^2}{EI}Z(1 - Y) = -2\phi_L Z(1 - Y), \tag{C.16}$$

where $Z = z/L$ is the third normalized coordinate. The other two diagonal components of the strain tensor, ϵ_{xx} and ϵ_{zz} are smaller by a factor called *Poisson ratio*

ν [50] and have the opposite sign (a rubber rob becomes thinner when gets stretched):

$$\epsilon_{xx} \equiv \frac{\partial u}{\partial x} = -\nu\epsilon_{yy} = 2\nu\phi_L Z(1-Y), \tag{C.17}$$

$$\epsilon_{zz} \equiv \frac{\partial w}{\partial z} = -\nu\epsilon_{yy} = 2\nu\phi_L Z(1-Y). \tag{C.18}$$

$$\tag{C.19}$$

The off-diagonal elements are all zero.

$$\epsilon_{xy} = \frac{\partial u}{\partial y} + \frac{\partial v}{\partial x} = 0, \tag{C.20}$$

$$\epsilon_{yz} = \frac{\partial v}{\partial z} + \frac{\partial w}{\partial y} = 0, \tag{C.21}$$

$$\epsilon_{xz} = \frac{\partial u}{\partial z} + \frac{\partial w}{\partial x} = 0. \tag{C.22}$$

It is more convenient to use the normalized displacements $U \equiv u/L$, $V \equiv v/L$, and $W \equiv w/L$. We can directly calculate V by integrating eq. C.16:

$$V = 0 - 2\phi_L Z \int_0^Y (1-Y')dY' = -2\phi_L Z(Y - \frac{Y^2}{2}) + f(X,Z). \tag{C.23}$$

f is an arbitrary function of only X and Z. This result can be substitute into eqs. C.21 and C.20:

$$\frac{\partial W}{\partial Y} = -\frac{\partial V}{\partial Z} = 2\phi_L(Y - \frac{Y^2}{2}) - \frac{\partial f}{\partial Z}, \tag{C.24}$$

$$\frac{\partial U}{\partial Y} = -\frac{\partial V}{\partial X} = -\frac{\partial f}{\partial X}. \tag{C.25}$$

Integrating with respect to Y, we get these solutions:

$$W = \phi_L(Y^2 - \frac{Y^3}{3}) - Y\frac{\partial f}{\partial Z} + g(X,Z) \tag{C.26}$$

$$U = -Y\frac{\partial f}{\partial X} + h(X,Z). \tag{C.27}$$

In these equations g and h are two other arbitrary functions of only X and Z. We can again substitute these solutions in eqs. C.18 and C.17. Therefore we get:

$$-Y[\frac{\partial^2 f}{\partial Z^2} - 2\nu\phi_L Z] + \frac{\partial g}{\partial Z} - 2\nu\phi_L Z = 0, \tag{C.28}$$

$$-Y[\frac{\partial^2 f}{\partial X^2} - 2\nu\phi_L Z] + \frac{\partial h}{\partial X} - 2\nu\phi_L Z = 0. \tag{C.29}$$

Since f is a function of only X and Z, and the above equations must be valid for any X, the [ ] terms must be equal to zero:

$$-\frac{\partial^2 f}{\partial Z^2} - 2\nu\phi_L Z = 0, \tag{C.30}$$

$$-\frac{\partial^2 f}{\partial X^2} - 2\nu\phi_L Z = 0. \tag{C.31}$$

Then we get one step closer to the solution of g and h functions in eqs. C.28 and C.31.

$$g = \nu\phi_L Z^2 + p(X), \tag{C.32}$$

$$h = 2\nu\phi_L XZ + q(z). \tag{C.33}$$

p is a function of only X and q a function of only Z. Now we can substitute these

solutions in eqs. C.26 and C.27 and then apply condition C.22 to obtain:

$$-2Y\frac{\partial^2 f}{\partial X\,\partial Z}+\frac{dp}{dX}+\frac{dq}{dZ}+2\nu\phi_L X=0. \tag{C.34}$$

Again For this equation to be valid for any value of y, it requires that:

$$\frac{\partial^2 f}{\partial X\,\partial Z}=0. \tag{C.35}$$

Separation of variables then requires that:

$$\frac{dp}{dX}+2\nu\phi_L X=-a, \tag{C.36}$$

$$\frac{dq}{dZ}=a. \tag{C.37}$$

In this equation a is a constant. The solution are simple:

$$p=-\nu\phi_L X^2-aX+p_0, \tag{C.38}$$

$$q=aZ+q_0. \tag{C.39}$$

p_0 and q_0 are constants. It can be seen that equation C.35 is consistent with eqs. C.30 and C.31 only for $\nu=0$. This is because the conditions in eq. C.20, C.21, and C.22 ignore coupling between the three axes. However, since ν for silicon (and in general) is only a few percent, we use the $\nu=0$ solutions as an approximation. In this case, we find:

$$f=AX+BZ+C. \tag{C.40}$$

A, B, and C are constants. Substituting our solutions in eqs C.27, C.23, and C.26,

we find the following solutions for the displacements:

$$U = -AY + 2\nu\phi_L XZ + aZ + q_0, \tag{C.41}$$

$$V = -2\phi_L Z(Y - \frac{Y^2}{2}) + AX + BZ + C, \tag{C.42}$$

$$W = \phi_L(Y^2 - \frac{Y^3}{3}) - BY + \nu\phi_L(Z^2 - X^2) - aX + p_0. \tag{C.43}$$

The boundary conditions at $y = 0$ are the followings:

$$\begin{aligned} U = V = W = 0 \quad & \text{no displacement,} \\ \frac{\partial W}{\partial Y} = 0 \quad & \text{zero slope,} \\ \frac{\partial W}{\partial X} = 0 \quad & \text{zero anticlastic curvature,} \\ \frac{\partial U}{\partial Y} = 0 \quad & \text{zero lateral slope.} \end{aligned} \tag{C.44}$$

Our solutions don't satisfy all these boundary conditions (see Fig. C.5), because, our initial assumptions that $\epsilon_{xy} = \epsilon_{yz} = \epsilon_{xz} = 0$ are not valid near the fixed end of the cantilever. The exact analytical solutions for deformations with these boundary conditions are too complicated. For example, Sader [114] derived the solutions for a cantilever with constant bending moment. However, our simple model can provide the approximate answer for points far enough (about the width of the cantilever) from the fixed end. Only near the fixed end of the cantilever the exact solution differs from the simple treatment given here. If we apply the boundary conditions at the origin

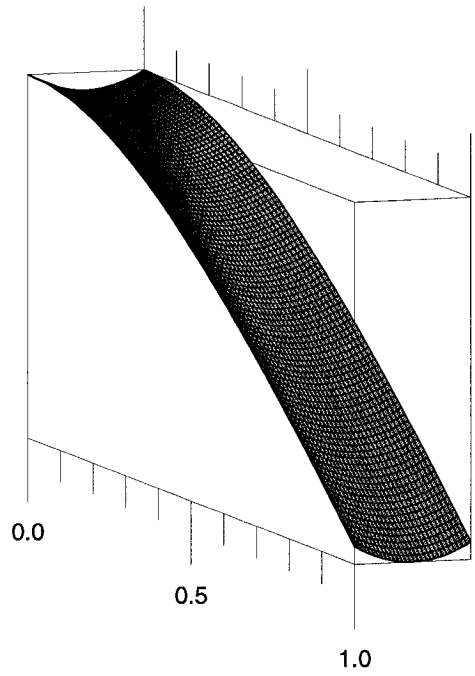

Figure C.5: Three dimensional deflection of the natural plane of a simple beam.

$X = Y = Z = 0$, we find that all the constants will be zero and the final solutions for the cantilever displacements will be given by:

$$U = 2\nu\phi_L XZ, \tag{C.45}$$

$$V = -2\phi_L Z(Y - \frac{Y^2}{2}), \tag{C.46}$$

$$W = \phi_L(Y^2 - \frac{Y^3}{3}) + \nu\phi_L(Z^2 - X^2). \tag{C.47}$$

The $-\nu\phi_L X^2$ term in eq C.47 shows the parabolic anticlastic curvature across the cantilever width. A three dimensional plot of W for the natural axis is plotted in Fig. C.5.

The strains are given by the derivatives:

$$\epsilon_{xx} = \frac{\partial U}{\partial X} = 2\nu\phi_L Z, \tag{C.48}$$

$$\epsilon_{yy} = \frac{\partial V}{\partial Y} = -2\phi_L Z(1-Y), \tag{C.49}$$

$$\epsilon_{zz} = \frac{\partial W}{\partial Z} = 2\nu\phi_L Z. \tag{C.50}$$

Bibliography

[1] J. Als-Nielsen and D. McMorrow. *Elements of Modern X-ray Physics.* Wiley, 2001.

[2] G. Arlt, D. Hennings, and G. de With. Dielectric properties of fine-grained barium titanate ceramics. *J. Appl. Phys.*, 58(4):1619–1625, 1985.

[3] G. Arlt and N. A. Pertsev. Force constant and effective mass of 90° domain walls in ferroelectric ceramics. *J. Appl. Phys.*, 70(4):2283–2289, 1991.

[4] G. Arlt and P. Sasko. Domain configuration and equilibrium size of domains in $BaTiO_3$. *J. Appl. Phys.*, 51(9):4956–4960, 1980.

[5] O. Auciello, J. F. Scott, and R. Ramesh. The physics of ferroelectric memories. *Physics Today*, 51(7):22–27, 1998.

[6] Authier. *Dynamical theory of x-ray diffraction.* Oxford University Press, 2001.

[7] A. Authier. Study of the anomalous transmission of x-rays in crystals of silicon. *Bulletin de la Societe Francaise de Mineralogie et de Cristallographie*, 84(1):51–89, 1961. in French.

[8] B. W. Batterman. Dynamical diffraction of x rays by perfect crystals. *Rev. Mod. Phys.*, 36(3):681–717, 1964.

[9] J. F. Bell. Large deflection, rotation, and plastic strain in cantilever beams. *Int. J. Engng Sci*, 28(3):231–239, 1990.

[10] W. F. Berg. *Naturwissenshaften*, 19:391–396, 1931. in German.

[11] U. Bonse. Zur röntgenographischen bestimmung des typs einzelner versetzungen in einkristallen. *Zeitschrift für Physik*, 153:278–296, 1958. in German.

[12] M. Born and E. Wolf. *Principles of Optics.* Cambridge University Press, 7 edition, 1999.

[13] Bowen and Tanner. *High resolution X-ray Diffractometery and Topography.* Taylor and Francis, 1998.

[14] W. A. Brantley. Calculated elastic constants for stress problems associated with semiconductor devices. *J. Appl. Phys.*, 44(1):534–535, 1973.

[15] S. Brauer, G. B. Stephenson, and M. Sutton. Perfect crystals in the asymmetric bragg geometry as optical elements for coherent x-ray beams. *J. Synchrotron Rad.*, 2:163–173, 1995.

[16] J. D. Budai et al. X-ray microdiffraction study of growth modes and crystallographic tilts in oxide films on metal substrates. *Nature materials*, 2:487–492, 2003.

[17] W. Cao and L. E. Cross. Theory of tetragonal twin structures in ferroelectric pervoskite with a first-order phase transition. *Phys. Rev. B*, 44(1):5–12, 1991.

[18] G. S. Cargill, J. Angilello, and K. L. Kavanagh. Lattice compression from conduction electrons in heavily doped Si:As. *Phys. Rev. Lett.*, 61(15):1748–1751, 1988.

[19] M. E. Caspari and W. J. Merz. The electromechanical behavior of $BaTiO_3$ single-domain crystals. *Phys. Rev.*, 80(6):1082–1089, 1950.

[20] P. M. Chaikin and T. C. Lubensky. *Principles of condensed matter physics.* Cambridge University Press, 1995.

[21] K. S. Chandrasekaran, S. K. Mohanlal, and S. Israel. X-ray structure of barium titanate: missed opportunities. *Acta Crystallogr. Sect. B*, 56:918–919, 2000.

[22] C. J. Chen. *Introduction to scanning tunneling microscopy.* Oxford University Press, 1993.

[23] G. Y. Chen, T. Thundat, E. A. Wachter, and R. J. Warmack. Adsorption-induced surface stress and its effects on resonance frequency of microcantilevers. *J. Appl. Phys.*, 77:3618–3622, 1995.

[24] Y. Chikaura, M. Imai, and T. Ishikawa. Observation of microdefects in thin silicon crystals by means of plane-wave topography using synchrotron x-radiation. *Jap. J. Appl. Phys.*, 26(6):L889–92, 1987.

[25] Y. Chikaura, M. Imai, Y. Suzuki, and Y. Yatsurugi. Synchrotron x-radiation plane-wave topography for imaging microdefects in thinned silicon crystals. *J. Cryst. Growth.*, 103(1-4):141–9, 1990.

[26] W. Cochran. Crystal stability and the theory of ferroelectricity. *Phys. Rev. Lett.*, 3(9):412–414, 1959.

[27] W. Cochran. Crystal stability and the theory of ferro-electricity. *Advances in Physics*, 9:387–423, 1960.

[28] R. E. Cohen. Theory of ferroelectrics: A vision for the next decade and beyond. *J. Phys. Chem. Solids*, 61:139–146, 2000.

[29] D. Courjon. *Near-field microscopy and near-field optics.* Imperial College Press, 2003.

[30] D. Damjanovic. Ferroelectrics, dielectric and piezoelectric properties of ferroelectric thin films and ceramics. *Rep. Prog. Phys.*, 61:1267–1324, 1998.

[31] M. Dawber, K. M. Rabe, and J. F. Scott. Physics of thin-film ferroelectric oxides. *Rev. Mod. Phys.*, 77:1083–1130, 2005.

[32] Carlos Paz de Araujo, Orlando Auciello, Ramamoorthy Ramesh, and George W. Taylor, editors. *Science and Technology of Integrated Ferroelectrics (Ferroelectricity and Related Phenomena).* Gordon and Breach Science Publishers, 2000.

[33] I. de Wolf et al. Techniques for mechanical strain analysis in sub-micrometer structures: TEM/CBED, micro-raman spectroscopy, x-ray micro-diffraction and modeling. *Microelectronic Engineering*, 75:425–435, 2003.

[34] A. F. Devonshire. Theory of barium titanate. i. *Philos. Mag.*, 40:1040–1063, 1949.

[35] A. F. Devonshire. Theory of barium titanate. ii. *Philos. Mag.*, 42:1065–1079, 1951.

[36] A. F. Devonshire. Theory of ferroelectrics. *Advances in Physics*, 3:85–130, 1954.

[37] A. F. Devonshire. Some recent work on ferroelectrics. *Rep. Prog. Phys.*, 27:1–22, 1964.

[38] M. Drakopoulos, Z. W. Hu, S. Kuznetsov, A. Snigirev, I. Snigireva, and P. A. Thomas. Quantitative x-ray bragg diffraction topography of periodically domain-inverted $LiNbO_3$. *J. Phys. D*, 32:A160–A165, 1999.

[39] M. Dudley, X. Huang, and W. M. Vetter. Contribution of x-ray topography and high-resolution diffraction to the study of defects in SiC. *J. Phys. D*, 36:A30–A36, 2003.

[40] H. M. Duiker et al. Fatigue and switching in ferroelectric memories: Theory and experiment. *J. Appl. Phys.*, 68(11):5783–5791, 1990.

[41] A. Y. Emelyanov and N. A. Pertsev. Effect of finite domain-wall width on the domain structures of epitaxial ferroelectric and ferroelastic thin films. *J. Appl. Phys.*, 89(2):1355–1366, 2001.

[42] A. Enzler, N. Herres, and A. Dommann. Analysis of etched cantilevers. *Microelectronics Reliability*, 42:1807–1809, 2002.

[43] H. T. Evans. Note on anomalous dispersion and evans's x-ray study of tetragonal barium titanate. *Acta Cryst.*, 21:182, 1966.

[44] H.T. Evans. An x-ray diffraction study of tetragonal barium titanate. *Acta Cryst.*, 14:1019–1024, 1961.

[45] P. F. Fewster. Combining high-resolution x-ray diffraction and topography. *J. Appl. Crystallogr.*, 24:178–183, 2003.

[46] N. Floquet, J. Hector, and Gaucher P. Correlation between structure, microstructure, and ferroelectric properties of $PbZr_{0.2}Ti_{0.8}O_3$ integrated film: Influence of the sol-gel process and the substrate. *J. Appl. Phys.*, 84(7):3815–3826, 1998.

[47] N. Floquet and C. M. Valot. Ferroelectric domain walls in $BaTiO_3$: Structural wall model interpreting fingerprints in XRPD diagrams. *Ferroelectrics*, 234(1-4):107–122, 1999.

[48] N. Floquet, C. M. Valot, M. T. Mesnier, J. C. Niepce, L. Normand, A. Thorel, and R. Kilaas. Ferroelectric domain walls in $BaTiO_3$: Fingerprints in xrpd diagrams and quantitative hrtem image analysis. *J. Phys. III*, 7:1105–1128, 1997.

[49] G. Fogarty, B. Steiner, M. Cronin-Golomb, U. Laor, M. H. Garrett, J. Martin, and R. Uhrin. Antiparallel ferroelectric domains in photorefractive barium titanate and strontium barium niobate observed by high-resolution x-ray diffraction imaging. *J. Opt. Soc. Am. B*, 13(11):2636–2643, 1996.

[50] Ford. *Advanced Mechanics of Materials.* Ellis Horwood, 2 edition, 1977.

[51] M. H. Garrett, J. Y. Chang, H. P. Jenssen, and C. Warde. A method for poling barium titanate batio$_3$. *Ferroelectrics*, 120:167–173, 1991.

[52] Julio A. Gonzalo and Basilio Jiménez, editors. *Ferroelectricity, The Fundamentals Collection.* Wiley-VCH, 2005.

[53] A. Gruverman, O. Auciello, and H. Tokumoto. Imaging and control of domain structures in ferroelectric thin films via scanning force microscopy. *Annu. Rev. Mater. Sci.*, 28:101–123, 1998.

[54] P. J. Halfpenny and J. N. Sherwood. Synchrotron-radiation section topography of large uncut crystals of organic nonlinear optical materials. *Philos. Mag. Lett.*, 62(1):1–7, 1990.

[55] J. Harada, T. Pedersen, and Z. Barnea. X-ray and neutron diffraction study of tetragonal barium titanate. *Acta Crystallogr. Sect. A*, 26:336–344, 1970.

[56] M. Hart. Bragg angle measurement and mapping. *J. Cryst. Growth.*, 55(2):409–27, 1981.

[57] Kh. Hassani, M. Sutton, Tkachuk A., and M. Holt. X-ray microdiffraction imaging of a micron-size silicon cantilever. To be submitted soon, 2006.

[58] A. R. Hibbs. *Confocal microscopy for biologists.* Kluwer Academic / Plenum Publisher, 2004.

[59] M. Holt, Kh. Hassani, and M. Sutton. Microstructure of ferroelectric domains in batio3 observed via x-ray microdiffraction. *Phys. Rev. Lett.*, 95:085504, 2005.

[60] S. M. Hu. Stress-related problems in silicon technology. *J. Appl. Phys.*, 70(6):R53–R80, 1991.

[61] Z. W. Hu, P. A. Thomas, and W. P. Risk. Periodically poled Cs-exchanged $RbTiOAsO_4$ optical waveguides: High-resolution x-ray diffraction, scattering, and topography study. *Phys. Rev. B*, 58(10):6074–80, 1998.

[62] Y. Ishibashi. On polarization reversal in ferroelectrics. *Integrated Ferroelectrics*, 2:41–49, 1992.

[63] T. Ishikawa, T. Kitano, and J. Matsui. Equi-lattice-spacing mapping x-ray topography. *J. Appl. Crystallogr.*, 20:344–348, 1987.

[64] Hiroshi Ishiwara, Masanori Okuyama, and Yoshihiro Arimoto, editors. *Ferroelectric random access memories : fundamentals and applications.* Springer, 2004.

[65] A. A. Istratov and E. R. Weber. Structural, elemental, and chemical complex defects in silicon and their impact on silicon devices. *Electrochemical Society Interface*, 14(1):34–36, 2005.

[66] T. Jach, S. Kim, V. Gopalan, S. Durbin, and D. Bright. Long-range strains and the effects of applied field at 180° ferroelectric domain walls in lithium niobate. *Phys. Rev. B*, 69(6):64113, 2004.

[67] J. D. Jackson. *Cassical Electrodynamics.* Wiley, 3 edition, 1998.

[68] C. Jacobsen et al. Diffraction-limited imaging in a scanning transmission x-ray microscope. *Optics Communications*, 86:351–364, 1991.

[69] S. Jeon, Y. Braiman, and T. Thundat. Cross talk between bending, twisting, and buckling modes of three types of microcantilever sensors. *Rev. Sci. Instrum.*, 75(11):4841–4844, 2004.

[70] H. Kahn, C. Deeb, I. Chasiotis, and Heuer A. H. Anodic oxidation during mems processing of silicon and polysilicon: Native oxides can be thicker than you think. *J. Microlelectromechanical Systems*, 14(5):914–923, 2005.

[71] S. K. Kaldor and C. Noyan. Differentiating between elastically bent rectangular beams and plates. *Apl. Phys. Lett.*, 80(13):2284–2286, 2002.

[72] F. Kao and P. Török, editors. *Optical imaging and microscopy : techniques and advanced systems.* Springer-Verlag, 2003.

[73] S. Kawado et al. Synchrotron-radiation x-ray topography of surface strain in large-diameter silicon wafers. *J. Synchrotron Rad.*, 9(3):166–8, 2002.

[74] S. Kawado et al. Three-dimensional structure of dislocations in silicon determined by synchrotron white x-ray topography combined with a topo-tomographic technique. *J. Phys. D*, 38(10A):A17–22, 2005.

[75] R. Khachatryan, A. Tkachuk, Chu Y. S., Qian J., and Macrander A. Open-faced z-shaped channel-cut x-ray monochromator. In *Proc. SPIE*, volume 5537, pages 171–176, 2004.

[76] S. Kim, V. Gopalan, and B. Steiner. Direct x-ray synchrotron imaging of strains at 180 domain walls in congruent $LiNbO_3$ and $LiTaO_3$ crystals. *Apl. Phys. Lett.*, 77(13):2051–2053, 2000.

[77] S. Kimura et al. High-resolution x-ray topographic images of dislocations in a silicon crystal recorded using an x-ray zooming tube. *J. Synchrotron Rad.*, 5(3):1079–81, 1998.

[78] S. Kimura, T. Ishikawa, and J. Matsui. Observation of minute strain fields in a floating-zone-grown silicon crystal containing d defects by means of plane-wave x-ray topography. *Philos. Mag. A*, 69(6):1179–87, 1994.

[79] S. Kimura, T. Ishikawa, J. Mizuki, and J. Matsui. Analysis of minute strain field around a-swirl defects in a float zone silicon crystal by means of plane wave x-ray topography using extremely collimated x-rays. *J. Cryst. Growth.*, 116(1-2):22–26, 1992.

[80] P. Kirkpatrick and A. V. Baez. Formation of optical images by x-rays. *J. Opt. Soc. Am.*, 38:766–774, 1948.

[81] T. Kitano et al. Synchrotron plane wave x-ray topography of 6 inch diameter si crystal. *Jap. J. Appl. Phys.*, 26(2):L108–10, 1987.

[82] Landau and Lifshits. *Statistical physics, part 1.* Butterworth-Heinemann, 3 edition, 1999.

[83] Landau and Lifshits. *Theory of Elasticity.* Butterworth-Heinemann, 3 edition, 2002.

[84] A. R. Lang. Direct observation of individual dislocations by x-ray diffraction. *J. Appl. Phys.*, 29:597–598, 1958.

[85] S. Lida et al. Plane-wave synchrotron x-ray topography observation of grown-in microdefects in a slowly pulled CZ-silicon crystal. *J. Phys. D*, 38:A23–A27, 2005.

[86] M. E. Lines. *Principles and Applications of Ferroelectrics and Related Materials.* Oxford University Press, 2001.

[87] E. A. Little. Dynamic behavior of domain walls in barium titanate. *Phys. Rev.*, 98(4):978–984, 1955.

[88] P. Lu, H. P. Lee, H. Lu, and S. J. O'Shea. Surface stress effects on the resonance properties of cantilever sensors. *Phys. Rev. B*, 72:085405, 2005.

[89] W. Ludwig et al. Three-dimensional imaging of crystal defects by 'topo-tomography'. *J. Appl. Crystallogr.*, 34(5):602–607, 2001.

[90] W. P. Mason and B. T. Matthias. Theoretical model for explaining the ferro-electric effect in barium titanate. *Phys. Rev.*, 74:1622–1636, 1948.

[91] W. J. Merz. The electric and optical behavior of $BaTiO_3$ single-domain crystals. *Phys. Rev.*, 76(8):1221–1225, 1949.

[92] W. J. Merz. Domain properties in $BaTiO_3$. *Phys. Rev.*, 88:421–422, 1952.

[93] W. J. Merz. Domain formation and domain wall motions in ferroelectric $BaTiO_3$ single crystals. *Phys. Rev.*, 95(3):690–698, 1954.

[94] A. Michette and S. Pfauntsch. *X-rays : the first hundred years.* John Wiley & Sons, 1996.

[95] R. C. Miller. Some experiments on the motion of 180° domain walls in $BaTiO_3$. *Phys. Rev.*, 111(3):736–739, 1958.

[96] R. C. Miller and A. Savage. Further experiments on the sidewise motion of 180 ° domain walls $BaTiO_3$. *Phys. Rev.*, 115(5):1176–1180, 1959.

[97] R. C. Miller and G. Weinreich. Mechanism for the sidewise motion of 180 ° domain walls in barium titanate. *Phys. Rev.*, 117(6):1460–1466, 1960.

[98] D. M. Mills, editor. *Third-generation hard x-ray synchrotron radiation sources : source properties, optics, and experimental techniques.* Wiley, 2002.

[99] P. Muralt. Ferroelectric thin films for micro-sensors and actuators: a review. *J. Micromech. Microeng.*, 10:136–146, 2000.

[100] C. E. Murray, C. C. Goldsmith, and I. C. Noyan. Spatially transient stress effects in thin films by x-ray diffraction. *Powder Diffraction*, 20(2):112–116, 2005.

[101] C.E. Murray, I.C. Noyan, P.M. Mooney, B. Lai, and Z. Cai. Mapping of strain fields about thin film structures using x-ray microdiffraction. *Apl. Phys. Lett.*, 83(20):4163–5, 2003.

[102] S. Nambu, , and D. A. Sagala. Domain formation and elastic long-range interaction in ferroelectric pervoskite. *Phys. Rev. B*, 50(9):5838–5847, 1994.

[103] Newkirk. *Direct observation of imperfections in crystals.* New York Interscience Publishers, 1962.

[104] X. J. Ning. Distribution of residual stresses in boron doped p^+ silicon. *J. Electrochemical Society*, 143:3389–3393, 1996.

[105] I. C. Noyan, T. C. Huang, and B. R. York. Residual stress/strain analysis in thin films by x-ray diffraction. *Crit. Rev. Solid State Mater. Sci. (USA)*, 20(2):125–177, 1995.

[106] Characterization of substrate/thin-film interfaces with x-ray microdiffraction. Noyan, i.c. and jordan-sweet, j. and liniger, e.g. and kaldor, s.k. *Apl. Phys. Lett.*, 72(25):3338–40, 1998.

[107] J. Padilla, W. Zhong, and D. Vanderbilt. First-principles investigation of 180 domain walls in $BaTiO_3$. *Phys. Rev. B*, 53(10):R5969–R5972, 1996.

[108] Phillips. *Crystals, defects and microstructures : modeling across scales.* Cambridge University Press, 2001.

[109] H. Rarback et al. Scanning x-ray microscope with 75-nm resolution. *Rev. Sci. Instrum.*, 59:52–59, 1988.

[110] L. Reimer. *Transmission electron microscopy : physics of image formation and microanalysis.* Springer, 1997.

[111] L. Reimer. *Scanning electron microscopy : physics of image formation and microanalysis.* Springer, 1998.

[112] R. C. Rogan, N. Tamura, G. A. Swift, and E. Üstündag. Direct measurement of triaxial strain fields around ferroelectric domains using x-ray microdiffraction. *nature materials*, 2:379–381, 2003.

[113] J. E. Sader. Surface stress induced deflections of cantilever plates with applications to the force microscope: Rectangular plates. *J. Appl. Phys.*, 89(5):2911–2921, 2001.

[114] J. E. Sader. Surface stress induced deflections of cantilever plates with applications to the force microscope: V-shape plates. *J. Appl. Phys.*, 91(11):9354–61, 2002.

[115] J. E. Sader and R. C. Sader. Susceptibility of atomic force microscope cantilevers to lateral forces: Experimental verification. *Apl. Phys. Lett.*, 83(15):3195–3197, 2003.

[116] T. Saka, T. Katagawa, and N. Kato. The theory of x-ray crystal diffraction for finite polyhedral crystals. I. the Laue-Bragg cases. *Acta Crystallogr. Sect. A*, 28:102–113, 1972.

[117] T. Saka, T. Katagawa, and N. Kato. The theory of x-ray crystal diffraction for finite polyhedral crystals. II. the Laue-$(\text{Bragg})^m$ cases. *Acta Crystallogr. Sect. A*, 28:113–120, 1972.

[118] T. Saka, T. Katagawa, and N. Kato. The theory of x-ray crystal diffraction for finite polyhedral crystals. III. the Bragg-$(\text{Bragg})^m$ cases. *Acta Crystallogr. Sect. A*, 29:192–200, 1973.

[119] D. Sarid. *Scanning force microscopy : with applications to electric, magnetic, and atomic forces.* Oxford University Press, 1994.

[120] F. Saurenbach and B. D. Terris. Imaging of ferroelectric domain walls by force microscopy. *Apl. Phys. Lett.*, 56(17):1703–1705, 1990.

[121] C. B. Sawyer and C. H. Tower. Piezoelectric activity of rochelle salt under various conditions. *Phys. Rev.*, 19:478–491, 1922.

[122] C. B. Sawyer and C. H. Tower. Rochelle salt as a dielectric. *Phys. Rev.*, 35:269–273, 1930.

[123] J. F. Scott. Limitations on ulsi-ferams. *IEICE TRANS. ELECTRON.*, E81-C(4):477–487, 1998.

[124] J. F. Scott. *Ferroelectric memories.* Springer, 2000.

[125] E. Snoeck, L. Normand, A. Thorel, and C. Roucau. Electron microscopy study of ferroelastic and ferroelectric domain wall motions induced by the in situ application of an electric field in $BaTiO_3$. *Phase Transitions*, 46:77, 1994.

[126] V. T. Srikar, A. K. Swan, and M. S. Unlu. Micro-ramman measurement of bending stresses in micromachined silicon flexures. *J. Microlelectromechanical Systems*, 12(6):779–787, 2003.

[127] H. L. Stadler and P. J. Zachmanidis. Nucleation and growth of ferroelectric domains in $BaTiO_3$ at fields from 2 to 450 kv/cm. *J. Appl. Phys.*, 34(11):3255–3260, 1963.

[128] S. Stemmer, S. K. Streiffer, F. Ernst, and Rühle M. Atomistic structure of 90° domain walls in ferroelectric $PbTiO_3$ thin films. *Philos. Mag. A*, 71(3):713–724, 1995.

[129] N. Tamura et al. Submicron x-ray diffraction and its applications to problems in materials and environmental science. *J. Synchrotron Rad.*, 73:1369–1372, 2001.

[130] G. Tarrach, P. Lagos, and R. Hermans. Nanometer spot allocation for raman spectroscopy on ferroelectrics by polarization and piezoresponse force microscopy. *Apl. Phys. Lett.*, 79(19):3152–3154, 2001.

[131] M. Tatsuya and F. Masamichi. Calibration of surface stress measurements with atomic force microscopy. *J. Appl. Phys.*, 81(11):7099–7101, 1997.

[132] J. C. Toledano and P. Toledano. *Landau theory of phase transitions: applications to structural, incommensurate, magnetic, and liquid crystal systems.* World Scientific, 1987.

[133] C. M. Valot, N. Floquet, M. Perriat, M. Mesnier, and J. C. Niepce. Ferroelectric domains in $BaTiO_3$ powder and ceramics evidenced by x-ray diffraction. *Ferroelectrics*, 172:235–241, 1995.

[134] B. E. Warren. *X-ray Diffraction.* Dover, 1990.

[135] O. Wolter, Th. Bayer, and J. Greshner. Micromachined silicon sensors for scanning force microscopy. *J. Vac. Sci. Technol. B*, 9(2):1353–1357, 1991.

[136] B. Wul. Barium titante: a new ferro-electric. *Nature*, 157:808, 1946.

[137] Y. Xu. *Ferroelectric materials and their applications.* Elsevier Science Pub. Co., 1991.

[138] S. I. Yakunin, V. V. Shakamanov, G. V. Spivak, and N. V. Vasil'eva. Microstructure of domains and domain walls in single-crystal films of barium titanate. *Nature*, 14(2):310–313, 1972.

[139] T. J. Yang, V. Gopalan, P. Swart, and U. Mohideen. Experimental study of internal fields and movement of single ferroelectric domain walls. *J. Phys. Chem. Solids*, 61:275–282, 2000.

[140] W. Yang et al. Spatially resolved poisson strain and anticlastic curvature measurements in si under large deflection bending. *Apl. Phys. Lett.*, 82(22):3856–3858, 2003.

[141] V. A. Zirov. A contribution to the theory of domain walls in ferroelectrics. *Soviet Physics JETP*, 35(5):822–825, 1959.

[142] E. Zolotoyabkoa, J. P. Quintana, B. H. Hoerman, and B. W. Wessels. Fast time-resolved x-ray diffraction in $BaTiO_3$ films subjected to a strong high-frequency electric field. *Apl. Phys. Lett.*, 80(17):3159–3161, 2002.

[143] www.mticrystals.com.

[144] www.newfocus.com.

[145] www.microesys.com.

[146] www.certif.com.

[147] www.nanosensors.com.

Index